J. Fluid Mech. (1988), *vol.* 192, *pp.* 115–173
Printed in Great Britain

The dynamics of coherent structures in the wall region of a turbulent boundary layer

By NADINE AUBRY,† PHILIP HOLMES,‡‖
JOHN L. LUMLEY† AND EMILY STONE‡

† Sibley School of Mechanical and Aerospace Engineering, Cornell University, Ithaca, NY 14853, USA

‡ Department of Theoretical and Applied Mechanics, Cornell University, Ithaca, NY 14853, USA

‖ Department of Mathematics and Center for Applied Mathematics, Cornell University, Ithaca, NY 14853, USA

Corrigendum 324 pp 407-408

(Received 31 October 1986 and in revised form 17 November 1987)

We have modelled the wall region of a turbulent boundary layer by expanding the instantaneous field in so-called empirical eigenfunctions, as permitted by the proper orthogonal decomposition theorem (Lumley 1967, 1981). We truncate the representation to obtain low-dimensional sets of ordinary differential equations, from the Navier–Stokes equations, via Galerkin projection. The experimentally determined eigenfunctions of Herzog (1986) are used; these are in the form of streamwise rolls. Our model equations represent the dynamical behaviour of these rolls. We show that these equations exhibit intermittency, which we analyse using the methods of dynamical systems theory, as well as a chaotic regime. We argue that this behaviour captures major aspects of the ejection and bursting events associated with streamwise vortex pairs which have been observed in experimental work (Kline *et al.* 1967). We show that although this bursting behaviour is produced autonomously in the wall region, and the structure and duration of the bursts is determined there, the pressure signal from the outer part of the boundary layer triggers the bursts, and determines their average frequency. The analysis and conclusions drawn in this paper appear to be among the first to provide a reasonably coherent link between low-dimensional chaotic dynamics and a realistic turbulent open flow system.

1. Introduction

There has been much interest in recent years regarding the application of methods, ideas and models from dynamical systems and bifurcation theory to the study of turbulent fluid flow. The first paper in which an explicit link was made between strange attractors and turbulence is that of Ruelle & Takens (1971), although, unknown to those authors, Lorenz (1963) had proposed a three-dimensional set of ordinary differential equations (ODEs) as a minimal model for two-dimensional Bénard convection considerably earlier.

Recent work in this area, accounts of which can be found in collections such as Rand & Young (1981), Swinney & Gollub (1981) and Campbell & Rose (1983), has concentrated on 'closed' flow systems such as the Rayleigh–Bénard or Taylor–Couette problems. In such problems, simultaneous variation of two or more parameters (Reynolds or Rayleigh numbers, Prandtl number, aspect ratios, etc.) gives rise to multiple bifurcations in which two or more modes become simultaneously

unstable. Centre manifold and normal form methods then permit the analysis of such modal interactions in terms of low-dimensional dynamical systems: relatively small sets of ODEs. For background see Guckenheimer & Holmes (1983) or Golubitsky & Guckenheimer (1986). These methods are closely related to the classical amplitude expansions of weakly nonlinear hydrodynamic stability theory (Drazin & Reid 1981). (In fact, Galerkin and other discretization techniques are not always easy to apply to such problems, since, even if the steady (bifurcating) solution is known analytically, the normal modes are not usually elementary functions and linear stability analyses are not straightforward.) Even in this situation, however, rigorous results have not gone beyond the first preturbulent bifurcations from steady, laminar flows. There is nothing close to a proof of Ruelle & Takens' conjecture that the Navier–Stokes equation has a strange attractor for a realistic flow geometry. On the other hand, sophisticated analyses of experimental data have lent much support to the thesis that low-dimensional dynamics do control certain aspects of preturbulent flow in closed fluid systems (see Swinney 1983 and references therein).

In view of this, the present study of an open flow – the fully developed boundary layer on a flat plate – might seem hopeless. As Monin (1978) has pointed out, low-dimensional models cannot hope to account for the detailed, high wavenumber, spatially chaotic aspects of fully developed turbulence. Moreover, in open flow systems natural modal decompositions such as the Fourier modes of linear theory are lacking or of limited use in the inhomogeneous directions. Thus another expansion is necessary and a coherent structure approach seems to be worth investigating for a judicious determination of relevant modes when large eddies are experimentally seen to play an important role. Since the early work of Theodorsen (1952), which suggested the importance of large-scale horseshoe-shaped vortices in turbulent transport in a turbulent boundary layer, flow visualization and conditional sampling techniques have revealed the existence of organized structures in many shear flows.

Nevertheless the extraction of deterministic features from a random, fine-grained turbulent flow has been a challenging problem. Zilberman, Wygnanski & Kaplan (1977) write: 'there are no consistent methods for identification which are independent of the techniques and the observer' and 'we cannot unambiguously define the signature of an eddy without *a priori* knowledge of its shape and its location relative to the observation station and cannot map such an eddy because we do not have a proper criterion for pattern recognition'. More recently, Kim (1983) has used a conditional sampling technique based on numerical data but he also admits the subjectivity of the method due to the arbitrary choice of detection functions and threshold values.

In contrast, Lumley (1967) proposed an unbiased technique for identifying such structures. The method consists of extracting the candidate that is the best correlated, in a statistical sense, with the background velocity field. Such a quantity is called, by definition, *a structure*. The different structures are identified with the orthogonal eigenfunctions of the proper orthogonal or Karhunen–Loève decomposition theorem of probability theory (Loève 1955). This is thus a systematic way to find organized motions in a given set of realizations of a random field. The question remains of how energetic and characteristic of the full turbulence of the flow such structures are. The method applied here is optimal in the sense that the series of eigenmodes converges more rapidly (in quadratic mean) than any other representation. Nevertheless the use of these modes for a low-dimension dynamical system study requires a very fast convergence of the series. The method we propose

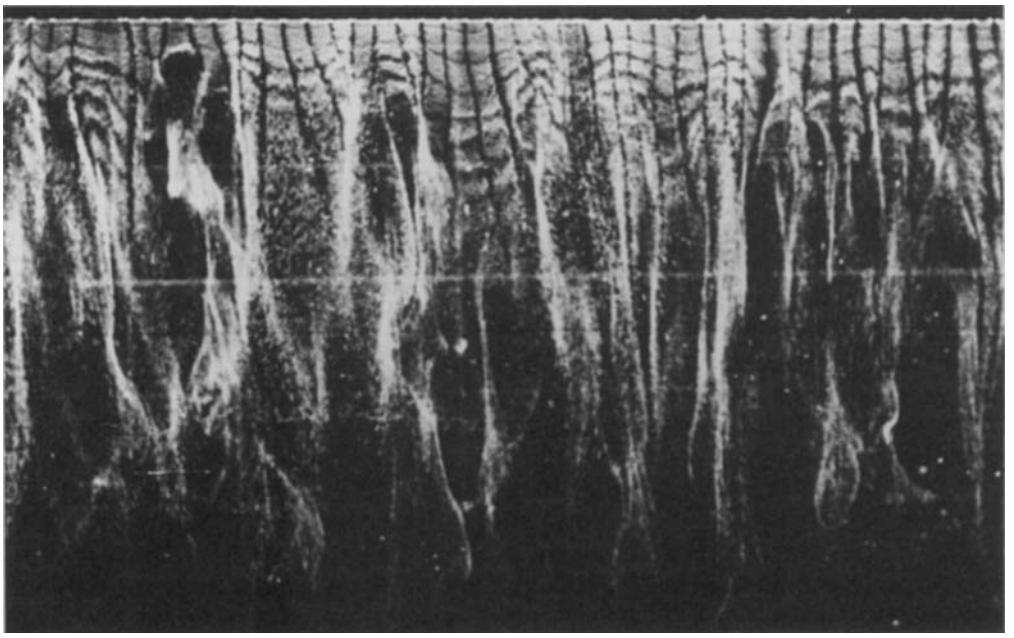

FIGURE 1. Bubble-wire visualization of the turbulent boundary layer at $x_2^+ = 6.6$. A single frame from the movie taken by S. Kline at Stanford University (see Kline *et al.* 1967) and kindly provided by S. Kline.

here is therefore limited in application to certain types of flows in which large coherent structures contain a major fraction of the energy. It has been demonstrated that axisymmetric turbulent jet mixing layers (Glauser, Leib & George 1985*a*) and wall regions of turbulent boundary layers (Moin 1984; Herzog 1986) belong to this group. In the wall region of a turbulent boundary layer, large eddies, which manifest themselves as streamwise streaks in visualizations, and are thought to be characteristic organized structures, are experimentally observed to be intermittent in time and space (in the streamwise direction). They are associated with a succession of events in which their sudden breakup corresponds to peaks in the turbulent energy production. These violent motions of the streaks, called *bursting events*, are also thought to be the basic phenomenon for turbulent energy transfer between the inner and outer regions of the layer, and hence they contribute significantly to the entire turbulence process.

Despite the contribution of many researchers, the description of these eddies is still vague. Theodorsen (1952) was probably the first to suggest the formation of these vortices inclined at an angle of 45° to the wall. Head & Bandyopadhyay's (1981) experiments convincingly established the existence of horseshoe or hairpin vortices – depending on the value of Reynolds number – in the wall region of a boundary layer (cf. Willmarth & Tu 1967). More recently, from a large-eddy simulation, Kim & Moin (1986) have used conditional sampling criteria to produce spatial structures and detect the presence of three-dimensional hairpin vortical structures inclined at 45° to the wall. A second group argues for the existence of streamwise elongated patterns, streaks and vortices. The experiment of Hama (Corrsin 1957) first revealed streamwise streaks which were also observed by Kline *et al.* (1967), figure 1, who were able to determine the average streak spacing. Bakewell & Lumley (1967) find

streamwise counter-rotating eddy pairs as the main structure of the wall region (see also Herzog 1986). Willmarth (1975, 1978) and Blackwelder & Eckelmann (1979) give a similar picture of the wall region. Hogenes & Hanratty (1982) find essentially the bottom halves of streamwise counter-rotating eddy pairs. It is not rare to find people belonging to both schools. For example, Head & Bandyopadhyay's investigations extending to the immediate vicinity of the wall provided visual evidence of streamwise filaments. They conclude that 'the hairpins have their origin in longitudinal vortex motions very close to the wall'. Nevertheless they do not feel able to provide 'firmly established connection(s)'. Kim's (1983, 1985) results, obtained from a sampling technique (producing a time structure applied to numerical data), indicate that the bursting event is associated with a pair of counter-rotating streamwise vortices, since they survive in an ensemble-averaging technique. Whether or not these streamwise vortices are related to hairpins is unclear and although many connections have been proposed, nothing has been proved yet. For example, Smith (1984) states that these streamwise vortices are the legs of a horseshoe vortex structure.

The time-dependent behaviour of these structures has also remained unclear. Experimental results obtained from flow visualization provide a qualitative description in terms of a quasi-cyclic succession of events which consists of a gradual lift-up of the longitudinal, streamwise streaks, a sudden oscillation, a breakup or *bursting event*, a downward motion of high-speed fluid towards the wall, called a *sweep event*, and a violent upward motion of low-velocity fluid called an *ejection event*. This intense updraught is postulated to be closely related to the high local production of turbulent energy associated with the breakup of the streaks. For more details see Kline *et al.* (1967). Quantitative estimates have been given for the bursting period, i.e. the average time between two consecutive bursting events at a given spatial location (Kline *et al.* 1967; Rao *et al.* 1971). Many assumptions have been made to explain the bursting phenomenon. The most common is a secondary instability of an inflexional velocity profile in the updraught between the counter-rotating eddies, but nothing has really been proved.

A major purpose of this study is to understand better the patterns of the wall-region structures, their dynamics, the role they play in the bursting phenomenon and their importance in the turbulent production mechanism. Specifically, we shall develop a model for the wall region of the boundary layer (from $x_2^+ = 0$ to $x_2^+ = 40$ in wall units (Tennekes & Lumley 1972)), using the proper orthogonal decomposition of Lumley (1967, 1970, 1981) in the direction normal to the wall, in which the flow is strongly non-homogeneous. In the streamwise and spanwise directions the flow is essentially homogeneous, and Fourier modes will suffice. Used in conjunction with Galerkin projection, the proper orthogonal decomposition yields an optimal set of basis functions in the sense that the resulting truncated system of ODEs captures the maximum amount of kinetic energy among all possible truncations of the same order. The method has obvious advantages over *a priori* decompositions, based on linear normal modes, but it does not appear to have been used before owing to the difficulty of computing the proper orthogonal modes. For this one requires three-dimensional autocorrelation tensors averaged over many realizations of the flow in question, data only obtainable from lengthy experiments and analyses or from detailed numerical simulations. In our case complete data are only available from experimental work in a glycerine tunnel (Herzog 1986), although Moin (1984), has derived two-dimensional orthogonal modes from large-eddy simulations. However, as we shall see, knowledge of the autocorrelation tensor, and use of the Navier–Stokes

equations, does allow one to uniquely determine the unsteady flow, in contrast to Cantwell's (1981) expectation.

Using this modal decomposition, we derive and study minimal truncations of various orders of the Navier–Stokes equations in the wall layer. The modes neglected in the truncation are accounted for by a Heisenberg model and we include a feedback effect to account for the stabilizing role of the interaction between the mean (driving) velocity profile and the fluctuating velocity field in the wall region as disturbances grow. The final models are sets of 3–6 ODEs for the complex modal amplitudes. We study these equations analytically and numerically, and interpret their behaviour in the light of dynamical systems theory. This study should be seen as preliminary, and substantial modelling and mathematical issues remain to be resolved, but the initial indications are very encouraging.

We should make clear here that there are two generic questions that can be asked regarding the wall layer: (1) Where do the coherent structures in the wall region come from, i.e. what dynamical mechanism is responsible for their life cycle? (2) Supposing that there are streamwise rolls in the wall region, what is their dynamical behaviour? We concern ourselves here only with the second question.

For high values of the Heisenberg parameter (representing large losses to the unresolved modes) our model displays a unique, globally attracting fixed point which corresponds to (steady) streamwise vortices or rolls similar to those that have been observed in many experiments (e.g. Kline *et al.* 1967; Head & Bandopadhyay 1981). This is not entirely surprising, since the orthogonal and Fourier modes used in the Galerkin projection encode this velocity field structure, although the lateral dimension is autonomously selected by the system of equations. Even this is to a certain extent pre-ordained, since the vertical dimension is fixed by the choice of eigenfunctions; the system will of course choose roughly circular rolls, corresponding to minimum dissipation. However, as the Heisenberg parameter is reduced to about 1.6, the fixed point destabilizes and intermittent bursting behaviour occurs in which the modal content, amplitudes and geometry of the rolls, change quasi-periodically. Starting with almost steady rolls, a period of slow oscillatory growth occurs, culminating in a 'burst' after which the velocity field relaxes quickly to the steady state. This is strongly reminiscent of the bursts observed in experiments (Kline *et al.* 1967) and it is even possible to match typical burst periods by judicious choice of the Heisenberg parameter. Thus our model appears to capture not only the static behaviour of the coherent structures in the wall layer, but also major features of their dynamics. Moreover, it suggests that the bursts originate very close to the wall, as suggested by Kline *et al.* (1967). We also show that, while the character of the bursts is determined entirely by the wall layer, the pressure perturbation from the outer part of the boundary layer can trigger the occurrence of a burst; bursting frequency is thus determined by the pressure signal.

We must mention several other authors who have considered the dynamics of the wall region; in particular Chapman & Kuhn (1986), Hatziavramidis & Hanratty (1979), Ersoy & Walker (1985) and Nikolaides (1984). These authors have all carried out computations of solutions of the Navier–Stokes equations in the wall region with various truncations, and various boundary conditions. Chapman & Kuhn (1986) were interested primarily in the asymptotic behaviour of the various velocity components and Reynolds stress in the immediate vicinity of the wall. Ersoy & Walker (1985) examined the behaviour of streamwise counter-rotating eddy pairs in the vicinity of the wall. They found a zone of separation on the wall, and strong eruptions. (We may note here that we certainly do not claim to have discovered

eruptions – we are trying to *explain* them.) Hatziavramidis & Hanratty (1979) neglect streamwise variation of the field (as we do in this initial study), and assume that the cross-stream fluctuation of the velocity field at the top boundary contains one spatial (spanwise) wavenumber (that of the experimentally observed streak spacing) and one temporal frequency (that of the bursting period). They find streamwise counter-rotating eddies and separation bubbles on the wall. Nikolaides (1984) calculated with more realistic conditions on the outer boundary and obtained solutions in many respects similar to ours.

We feel that all these investigations have substantially different goals and results from ours. To begin with, since the Navier–Stokes equations describe the flow, correct solution of these equations in a domain with the proper boundary conditions should reproduce experimental findings. This is not to denigrate the difficulty of carrying out such a solution; however, nothing will have been learned about causality, mechanisms, etiology and so forth. Information of this sort can only come from hypotheses that reduce the system solved to something considerably less than the Navier–Stokes equations, and from detailed examination of the structure of the equations solved, and of the character of the solution trajectories in phase space. It is as though these authors said, 'Look! We can make a simple system that behaves like reality'. We are saying, 'We can dismantle the system and show you how it works'. We feel that these other investigations have shed no light on questions such as: what part of the dynamical behaviour of the wall region is autonomous, and what part is directly attributable to the influence of the outer region? What is the minimum complexity capable of reproducing this dynamical behaviour (i.e. what are the indispensable characteristics of a model)? How does the dynamical mechanism work, in detail? These and similar issues will be explored in the body of this paper. It is to answer such questions that we have embarked on this investigation.

The paper is organized as follows. In §§2–4 we outline the proper orthogonal decomposition, its application to the boundary-layer problem and the experimental work that provides our orthogonal modes. In §§5–6 we discuss the (Navier–Stokes) equations of motion and the Heisenberg parameter and mean profile feedback models. In §§7–8 we address the question of truncations and the derivation, via Galerkin projection of the ODEs. Section 9 contains mathematical analyses of these model equations, including a discussion of various invariant subspaces and their physical interpretation in terms of symmetries of the flow. Thus prepared, in §10 we embark on the stormy waters of numerical simulation, concentrating on a model involving a single orthogonal mode normal to the wall, a single ($k = 0$) streamwise Fourier mode and six spanwise Fourier modes. In §11 we discuss the important influence of the pressure term, neglected up to this point. Finally, in §§12–13 we illustrate and discuss the physical implications of the behaviour of our model equations.

The use of the proper orthogonal decomposition in turbulence analysis has been discussed in general in three recent papers of Sirovich (1987*a*, *b*, *c*) who has applied the method in studies of the Ginzburg–Landau equation (Sirovich & Rodriguez 1987) and Rayleigh–Bénard convection (Sirovich, Maxey & Tarman 1987).

Technical details, tables of coefficients, etc. are relegated to the Appendices and we attempt to keep our use of dynamical-systems jargon to a minimum. However, some technicalities are unavoidable, and the reader unfamiliar with the field is referred to Guckenheimer & Holmes (1983), Devaney (1985) or Guckenheimer (1986) for background. We hope that we have included enough information for such references to be unnecessary; our attempt to do so accounts for the length of this paper.

2. The proper orthogonal decomposition

Lumley (1967) proposed a method of identification of coherent structures in a random turbulent flow, which we now outline. An advantage of the method is its objectivity and lack of bias. Given a realization of an inhomogeneous, energy-integrable velocity field $x \in E$, it consists of projecting the random field $\boldsymbol{u}(x)$, on a candidate structure $\boldsymbol{\phi}(x)$, and selecting the structure that maximizes the projection

$$\gamma = (\boldsymbol{\phi}, \boldsymbol{u})/(\boldsymbol{\phi}, \boldsymbol{\phi})^{\frac{1}{2}} \tag{1}$$

in quadratic mean, where the inner product in the Hilbert space of L_2 (all measurable vectorial functions on the set E such that $\int_E |\boldsymbol{f}| < \infty$) is defined by $(\boldsymbol{f}, \boldsymbol{g}) = \int f_i^*(x)\, g_i(x)\, \mathrm{d}x$ and the norm by $(\boldsymbol{f}, \boldsymbol{f}) = |\boldsymbol{f}|^2$ (*indicates the complex conjugate).

In other words, we are interested in the structure that is the best correlated to the random, energy-integrable field. More precisely, given an ensemble of realizations of the field, the purpose is to find the structure that is the best correlated with all the elements of the ensemble. Thus we want to maximize a statistical measure of the magnitude of γ which can be given by the mean square of its absolute value $\langle |\gamma|^2 \rangle$. Here $\langle\ \rangle$ indicates the ensemble average. The calculus of variations reduces this problem of maximization to a Fredholm integral equation of the first kind:

$$\int R_{ij}(x, x')\, \phi_j(x')\, \mathrm{d}x' = \lambda \phi_i(x), \tag{2}$$

whose symmetric kernel, R_{ij} is the autocorrelation matrix. The properties of this integral equation are given by Hilbert–Schmidt theory. There is a denumerable set of eigenfunctions $\phi_i^{(n)}$ (structures). The eigenfunctions form a complete orthogonal set, which means that the random field can be reconstructed in the following way:

$$u_i(x) = \sum_{n=1}^{\infty} a^{(n)} \phi_i^{(n)}(x), \tag{3}$$

with $(\boldsymbol{\phi}^{(n)}, \boldsymbol{\phi}^{(m)}) = \delta_{nm}$ if the eigenfunctions are normalized. Here δ_{nm} is the Kronecker delta symbol. The coefficients are uncorrelated and their mean square values are the eigenvalues themselves.

$$\langle a^{(n)} a^{(m)} \rangle = \delta_{nm} \lambda^{(n)}. \tag{4}$$

The kernel can be expanded in a uniformly and absolutely convergent series

$$R_{ij}(x, x') = \sum_{n=1}^{\infty} \lambda^{(n)} \phi_i^{(n)}(x)\, \phi_j^{(n)*}(x'), \tag{5a}$$

and the turbulent kinetic energy is the sum (over n) of the eigenvalues:

$$E = \int \langle u_i u_i \rangle \, \mathrm{d}x = \sum_{n=1}^{\infty} \lambda^{(n)}. \tag{5b}$$

Thus every structure makes an independent contribution to the kinetic energy and Reynolds stress.

The most significant point of the decomposition is perhaps the fact that the convergence of the representation is optimally fast since the coefficients $a^{(n)} = (\boldsymbol{\phi}^{(n)}, \boldsymbol{u})$ of the expansion have been maximized in a mean-square sense. The mean square of the first coefficient is as large as possible, the second is the largest in the remainder of the series once the first term has been subtracted, etc.

We have presented this theorem for the simplest case, that of a completely

inhomogeneous, square integrable, field. If the random field is homogeneous in one or more directions, the spectrum of the eigenvalues becomes continuous, and the eigenfunctions become Fourier modes, so that the proper orthogonal decomposition reduces to the harmonic orthogonal decomposition in those directions. See Lumley (1967, 1970, 1981) for more details.

We shall apply this decomposition theorem to the fluctuating velocity field, after subtraction of the mean. Another possibility would be to look for eigenfunctions of the entire instantaneous field, mean plus fluctuating part. The question is, to what extent would these differ from the eigenfunctions for the fluctuating field? It is clear in general that the first eigenfunction for the instantaneous field will be the mean velocity. The next eigenfunction for the instantaneous field can be constructed from the first eigenfunction for the fluctuating field; if this is not orthogonal to the mean velocity, a small component proportional to the mean velocity must be subtracted. We may continue in this way, so that each eigenfunction for the instantaneous field will be a linear combination of the mean velocity and all eigenfunctions of the fluctuating field of that order and lower. In fact, for the one-dimensional case in the wall region of a turbulent boundary layer (see Bakewell & Lumley 1967), the first eigenfunction is proportional to the mean velocity profile, so that only the value of the first eigenvalue is changed, by the addition of an integral of the square of the mean velocity. In the general case, the representation of the instantaneous velocity field by the first few eigenfunctions is unchanged, since the series of eigenfunctions can be recombined to give the mean profile plus the series of eigenfunctions for the fluctuation. This approach would thus make no difference to our results. From now on, we shall discard this possibility, and adhere strictly to the decomposition of the fluctuating field.

3. Application of the proper orthogonal decomposition to the shear flow of the wall region

The flow of interest here is three-dimensional, approximately homogeneous in the streamwise direction (x_1) and spanwise direction (x_3), approximately stationary in time (t), inhomogeneous and of integrable energy in the normal direction (x_2).

Lumley's first proposition (1967, 1981) consisted of a four-dimensional decomposition; a proper orthogonal decomposition in the x_2-direction and a harmonic orthogonal decomposition in the three other directions:

$$u_i(x_1, x_2, x_3, t) = \sum_n \int a^{(n)}_{k_1 k_3 \omega} \, \mathrm{e}^{2\pi \mathrm{i}(k_1 x_1 + k_3 x_3 + \omega t)} \, \phi^{(n)}_{i\, k_1 k_3 \omega}(x_2) \, \mathrm{d}k_1 \, \mathrm{d}k_3 \, \mathrm{d}\omega, \tag{6}$$

where the $a^{(n)}$ are random coefficients and, the $\phi^{(n)}$ deterministic. The solution of the equation:

$$\int \Phi_{ij}(x_2, x_2') \, \phi^{(n)}_j(x_2') \, \mathrm{d}x_2' = \lambda^{(n)} \phi^{(n)}_i(x_2) \tag{7}$$

(Φ_{ij} denotes the Fourier transform of the autocorrelation tensor in the x_1, x_3, τ-directions; in effect, the kernel in (2) becomes a function of the difference of primed and unprimed arguments in each homogeneous direction, and one simply takes the Fourier transform in each of these directions to obtain (7). The values k_1, k_3 and ω are parameters on which all terms in equation (7) depend) for each triplet (k_1, k_3, ω), leads to the determination of the eigenfunctions

$$\phi^{(n)}_{i\, k_1 k_3 \omega}(x_2).$$

Nevertheless the $a^{(n)}$ are known only in their mean-square absolute value and the eigenfunctions can be multiplied by any arbitrary phase factor $e^{i\sigma(k)}$ depending on the wavenumbers, since (7) is homogeneous. Thus, the eigenvalue problem alone does not allow the reconstruction of the velocity field in physical space, although Lumley (1981) gives a method to recover this phase information from third-order statistics.

An alternative to the decomposition (6) is a three-dimensional decomposition which can be substituted in the Navier–Stokes equations in order to recover the phase information carried by the coefficients. We have to decide which variable we want to keep. Time is a good candidate since we are particularly interested in the temporal dynamics of the structures. Such a decomposition is possible, and we do not need a separation of variables in the eigenfunctions of the type $\boldsymbol{\phi}(\boldsymbol{x}, \omega) = A(\omega)\,\boldsymbol{\psi}(\boldsymbol{x})$ in (6) (as suggested by Glauser, George & Taulbee 1985*b*) if we do not use any decomposition in time and choose the appropriate autocorrelation tensor. The idea is to measure the two velocities at the same time and determine $\langle u_i(x_1, x_2, x_3, t)\, u_j(x_1', x_2', x_3', t)\rangle$. Since the flow is quasi-stationary, R_{ij} does not depend on time and nor do the eigenvalues and eigenfunctions. The information in time is carried by the coefficients $a^{(n)}$ which are still 'stochastic', but now evolve under the constraint of the equations of motion. Thus the decomposition becomes

$$u_i(x_1, x_2, x_3, t) = \sum_n \int a^{(n)}_{k_1 k_3}(t)\, e^{2\pi i(k_1 x_1 + k_3 x_3)}\, \phi^{(n)}_{i\,k_1 k_3}(x_2)\, \mathrm{d}k_1\, \mathrm{d}k_3 \tag{8}$$

and we have to solve (7) for each pair of wavenumbers (k_1, k_3). $\boldsymbol{\Phi}_{ij}$ now denotes the Fourier transform of the autocorrelation tensor in the x_1-, x_3-directions.

Our second change to the decomposition is a transformation of the Fourier integral into a Fourier series, assuming that the flow is periodic in the x_1- and x_3-directions. The periods L_1, L_3 are determined by the first non-zero wavenumbers chosen. Finally, each component of the velocity field can be expanded as the triple sum

$$u_i(x_1, x_2, x_3, t) = \frac{1}{(L_1 L_3)^{\frac{1}{2}}} \sum_{k_1 k_3 n} e^{2\pi i(k_1 x_1 + k_3 x_3)}\, a^{(n)}_{k_1 k_3}(t)\, \phi^{(n)}_{i\,k_1 k_3}(x_2), \tag{9}$$

In this case, a 'structure' is defined by

$$\frac{1}{(L_1 L_3)^{\frac{1}{2}}} \sum_{k_1 k_3} e^{2\pi i(k_1 x_1 + k_3 x_3)}\, a^{(n)}_{k_1 k_3}\, \phi^{(n)}_{i\,k_1 k_3}(x_2)$$

and the entire velocity field is recovered by the sum of all the structures (over n).

4. Experimental results

The candidate flow that we are investigating is the wall region (which reaches $x_2^+ = 40$) of a pipe flow with almost pure glycerine (98 %) as the working fluid (Herzog 1986). The Reynolds number based on the centreline mean velocity and the diameter of the pipe is 8750. The corresponding Reynolds number based on the shear velocity u_τ is 531. The measurements obtained from hot-film anemometry were taken at 882 point pairs, 7 points in the streamwise direction up to $x_1^+ = 40$, 6 points in the normal direction up to $x_2^+ = 40$ and 6 points in the spanwise direction up to $x_3^+ = 136$. Two components of velocity, u_1 and u_3, were measured for each pair for three minutes. The other velocity component, u_2, was deduced by integration of the continuity equation. From this data the autocorrelation tensor at zero time lag ($t - t' = 0$ between the two velocities), $R_{ij}(x_1 - x_1', x_2, x_2', x_3 - x_3')_{t-t'=0}$, was obtained and the spatial eigen-

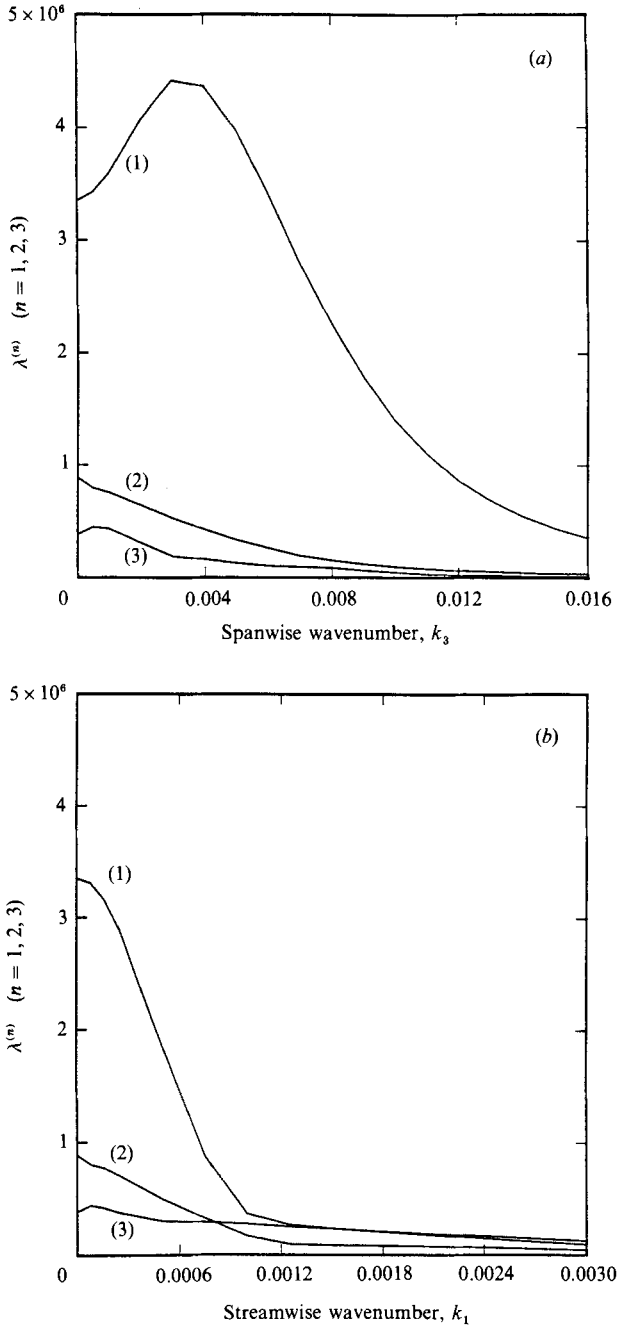

FIGURE 2. Convergence of the proper orthogonal decomposition in the near-wall region ($x_2^+ = 40$) of a pipe flow according to experimental data. Turbulent kinetic energy in the first three eigenmodes. $\lambda^{(n)}$ $(n = 1, 2, 3)$ as a function of (*a*) the spanwise wavenumber, (*b*) the streamwise wavenumber (from Herzog 1986).

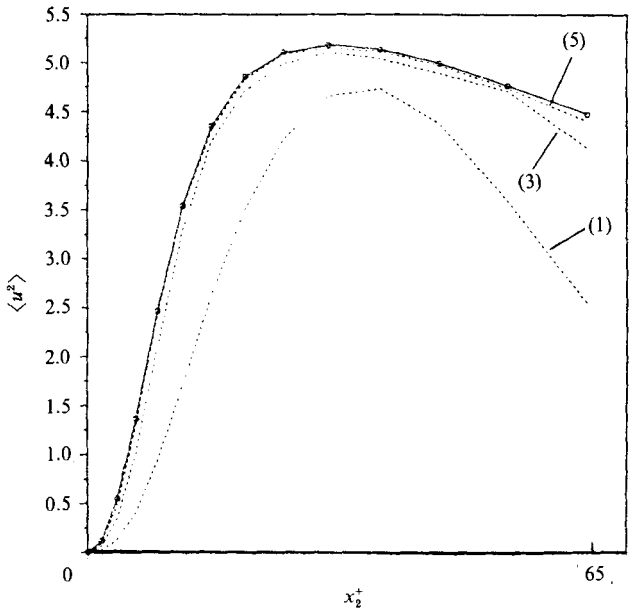

FIGURE 3. Convergence of the proper orthogonal decomposition in the near-wall region ($x_2^+ = 65$) of a channel flow according to numerical data. Contribution to the turbulent kinetic energy of one, three, five eigenmodes (from Moin 1984).

functions were extracted by numerical solution of the eigenvalue problem. Figure 2 illustrates the convergence of the resulting eigenfunction expansion in the wall region; for comparison similar data derived from numerical simulations of Moin (1984) are shown in figure 3. The three components of the first empirical eigenfunction for different spanwise wavenumbers and zero streamwise wavenumber are shown in figure 4 as functions of x_2. In the present study, only the two components of the eigenfunctions that are directly obtained from the experimental data are used; they are curve fitted (since the first and second derivatives are needed) and the third component is derived analytically from the continuity equation which is thus exactly satisfied. This equation can be written in terms of the eigenfunctions

$$2\pi(\mathrm{i}k_1 \phi_{1_k}^{(n)}(x_2) + \mathrm{i}k_3 \phi_{3_k}^{(n)}(x_2)) + \frac{\mathrm{d}\phi_{2_k}^{(n)}(x_2)}{\mathrm{d}x_2} = 0. \tag{10}$$

The results show that approximately 60% of the total kinetic energy and Reynolds stress is contained in the first eigenmode and that the first three eigenmodes capture essentially the entire flow field as far as these statistics are concerned. This very fast convergence of the decomposition in the near-wall region is in good agreement with Moin's (1984) results. From a large-eddy-simulation data base, Moin uses the proper orthogonal decomposition successively in one and two dimensions in the wall region (up to $x_2^+ = 65$). His first structure contains 60% of the total kinetic energy and 120% of the Reynolds stress (this apparent paradox occurs because the contribution of higher-order structures to the Reynolds stress is negative). 90% of the kinetic energy is captured by the first three terms. Nevertheless in a much larger integration domain, which extends to the centreline of the channel,

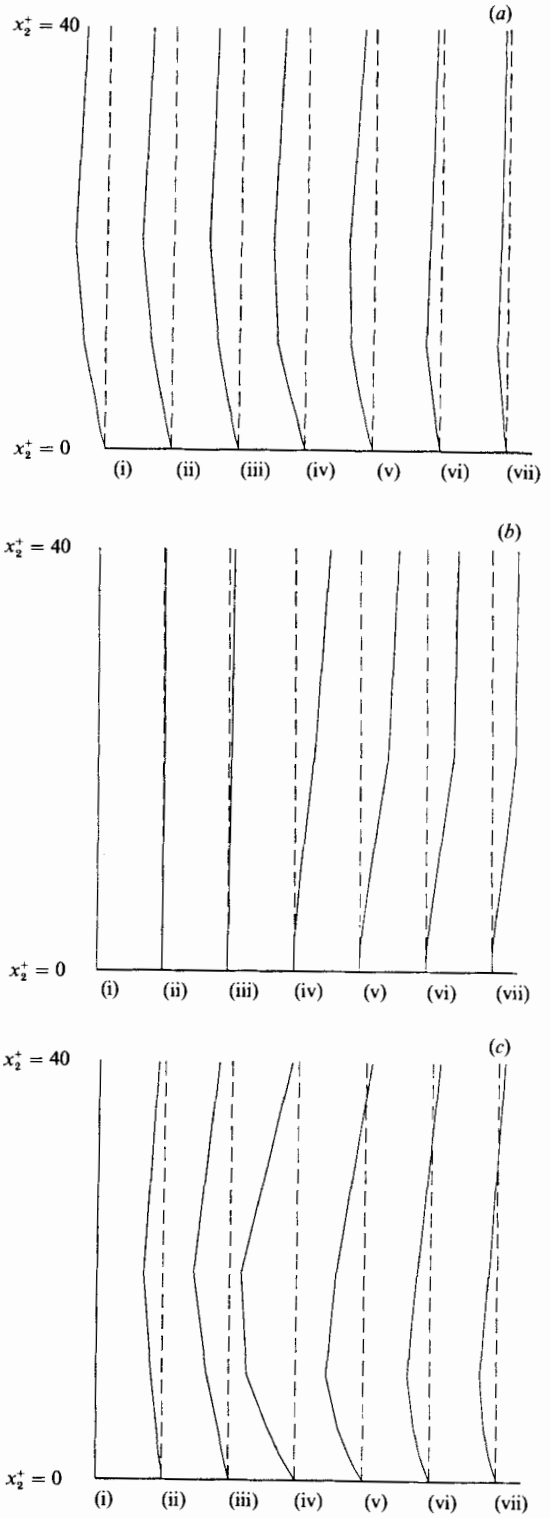

FIGURE 4. Empirical components $[(a, b, c)$ respectively $(x_1, x_2, x_3)]$ of the first eigenfunction as functions of x_2^+, weighted by the square root of the corresponding eigenvalues, for different spanwise wavenumbers and zero streamwise wavenumber, from experimental data (from Herzog 1986); wavenumbers k_3: (i) 0; (ii) 5×10^{-4}; (iii) 10^{-3}; (iv) 4×10^{-3}; (v) 8×10^{-3}; (vi) 1.3×10^{-2}; (vii) 1.6×10^{-2}.

the convergence is much slower ($\sim$ 20 terms are needed). Both studies show that each term in the decomposition corresponding to the first eigenmode

$$a^{(1)}_{k_1 k_3} \phi^{(1)}_{i\,k_1 k_3}(x_2)\, \mathrm{e}^{2\pi \mathrm{i}(k_1 x_1 + k_3 x_3)}$$

represents streamwise rolls. In order to reconstruct the entire velocity field, these authors made assumptions concerning the phases between the different wavenumbers, namely the phase angles were set to zero. Under such considerations the first coherent structure reveals the pattern of a pair of counter-rotating and symmetric rolls similar to the ones experimentally observed (Blackwelder & Kaplan 1976).

There is an apparent contradiction between the numbers of eigenfunctions we need for a more-or-less complete description of this flow field, and recent estimates of the Lyapunov dimension of the attractor corresponding to channel flow (Keefe *et al.* 1987). The latter, estimated in a very low-Reynolds-number flow, was in the range 360–400, and because of the relatively poor spatial resolution of the calculation, this was felt to be a lower bound. However, we should bear in mind (L. Sirovich, private communication) that when we say 20 eigenfunctions, we mean 20 eigenfunctions at each of, say, six cross-stream and, say, three streamwise wavenumbers, and of two components each (continuity makes the third redundant). Taking account of the various symmetries, this gives us a dimension of 1080 (see Aubry 1987), which is the right order of magnitude. In the wall region, carrying three eigenfunctions on the same wavenumber grid gives a dimension of 162. The case we are considering, with one eigenfunction and five active cross-stream wavenumbers, and only one in the streamwise direction, has a dimension of ten.

5. The dynamical equations

We decompose the velocity v – or the pressure π – into the mean (defined using a spatial average $1/L_1 L_3 \int (\,)\,\mathrm{d}x_1\,\mathrm{d}x_3$) flow $\boldsymbol{U}$ – or the corresponding mean pressure P – and the fluctuation $\boldsymbol{u}$ – or p:

$$\begin{aligned} \boldsymbol{v} &= \boldsymbol{u} + \boldsymbol{U} \quad \text{with } \boldsymbol{U} = U(x_2)\,\boldsymbol{e}_1, \\ \pi &= p + P. \end{aligned} \tag{11}$$

We substitute this decomposition into the Navier–Stokes equations:

$$\frac{\mathrm{d}u_i}{\mathrm{d}t} + u_{i,1} U + U_{,2}\, u_2\, \delta_{i1} + u_{i,j} u_j = -\frac{1}{\rho}(p_{,i} + P_{,i}) + \nu(u_{i,jj} + U_{,jj}\,\delta_{i1}). \tag{12}$$

Taking the spatial average ($\langle\ \rangle = 1/L_1 L_3 \int (\,)\,\mathrm{d}x_1\,\mathrm{d}x_3$) of these equations we obtain a relation between the divergence of the Reynolds stress and the mean pressure and velocity:

$$\langle u_{i,j} u_j \rangle = -\frac{1}{\rho} P_{,i} + \nu U_{,jj}\,\delta_{i1} \tag{13}$$

Equation (12) becomes, upon substitution of (13),

$$\frac{\mathrm{d}u_i}{\mathrm{d}t} + u_{i,1} U + U_{,2}\, u_2\, \delta_{i1} + u_{i,j} u_j - \langle u_{i,j} u_j \rangle = -\frac{1}{\rho} p_{,i} + \nu u_{i,jj}. \tag{14}$$

The mean velocity U can be expressed in terms of the Reynolds stress $\langle u_1 u_2 \rangle$ in a channel flow in a manner that gives some feedback to the system of equations as

the fluctuation varies. We shall see that this feedback is necessarily stabilizing for the first structure (according to the experimental results) and increases as the Reynolds stress gets stronger. In other words, this term controls the intensity of the rolls, by reducing the mean velocity gradient as the rolls intensify, thus weakening the source of energy. The expression for the mean velocity profile is the following:

$$U = \frac{1}{\nu}\int_0^{X_2} \langle u_1 u_2 \rangle \, \mathrm{d}x_2 + \frac{u_\tau^2}{\nu}\left(x_2 - \frac{x_2^2}{H}\right), \tag{15}$$

where X_2 is the upper edge of the integration domain and H the half-height of the channel. It contains two parts: one from the Reynolds stress, the other one from the mean pressure gradient. We can get a good idea of the mean velocity profile we are using by taking the time average of (15).

The expansion of the Fourier transform $\hat{u}_i$ of the fluctuating velocity u_i, defined by

$$u_i(x_1, x_2, x_3, t) = \frac{1}{L_1 L_3} \sum_{k_1 k_3} \mathrm{e}^{2\pi \mathrm{i}(k_1 x_3 + k_3 x_3)} \, \hat{u}_i(k_1, k_3, x_2, t), \tag{16}$$

is achieved by use of the complete set of eigenfunctions $\boldsymbol{\phi}^{(n)}$ in an infinite sum:

$$\hat{u}_i(k_1, k_3, x_2, t) = (L_1 L_3)^{\frac{1}{2}} \sum_{m=1}^{\infty} a^{(m)}_{k_1 k_3}(t) \, \phi^{(m)}_{i_{k_i k_3}}(x_2). \tag{17}$$

Since we want to truncate this sum, we use a Galerkin projection which minimizes the error due to the truncation and yields a set of ordinary differential equations for the coefficients. The idea is to make the residual

$$R_i = (L_1 L_3)^{\frac{1}{2}} \sum_{m=1}^{N} a^{(m)}(t) \, \phi_i^{(m)}(x_2) \tag{18}$$

orthogonal to each eigenfunction in the Hilbert space. After taking the Fourier transform of the Navier–Stokes equations $N_i = 0$ and introducing the truncated expansion, we apply Galerkin projection by taking the inner product

$$(\boldsymbol{\phi}^{(n)}, \boldsymbol{N}) = \int_0^{X_2} N_i(x_2) \, \phi_i^{(n)*}(x_2) \, \mathrm{d}x_2 = 0. \tag{19}$$

Finally we obtain a set of ordinary differential equations of the form:

$$\boldsymbol{A} \frac{\mathrm{d}a_k^{(n)}}{\mathrm{d}t} = \boldsymbol{B} a_k^{(n)} + \mathrm{NL}, \tag{20}$$

where $\boldsymbol{A}$ and $\boldsymbol{B}$ are matrices. Here $\boldsymbol{A}$ is the identity matrix (since the complete set of eigenfunctions is orthogonal) and NL are nonlinear terms. The nonlinear terms are of two sorts: quadratic and cubic. The quadratic terms come from the nonlinear fluctuation–fluctuation interactions and represent energy transfer between the different eigenmodes and Fourier modes. Their signs vary. The role of the Reynolds stresses $\langle u_i u_j \rangle$ in these terms should be mentioned. They vanish for all wavenumber pairs except for $(k_1, k_3) = (0, 0)$ for which they exactly cancel the quadratic term. Therefore they prevent this mode from having any kind of quadratic interactions with other Fourier modes. Since the cubic terms are zero too, the $(0, 0)$ mode just decays by action of viscosity and does not participate in the dynamics of the system.

The cubic terms come from the mean velocity–fluctuation interaction corresponding to the Reynolds stress $\langle u_1 u_2 \rangle$ in (15) (the other part of (15) leads to a linear term). Sine the streamwise and normal components of the first eigenfunction have opposite signs, they make a positive contribution to the turbulence production and hence provide negative cubic terms which are thus stabilizing. We remark that this is not necessarily the case for higher-order eigenfunctions.

By use of the continuity equation (10) and the boundary conditions

$$\phi_{2_k}^{(n)} = 0 \quad \text{at } x_2 = 0 \quad \text{(at the wall)},$$

and

$$x_2 \to \infty, \quad \phi_{2_k}^{(n)} \quad \text{(decay at infinity)},$$

it can be seen by integration by parts that the pressure term would disappear if the domain of integration covered the entire flow volume. Since this is not the case (rather the domain is limited to $X_2^+ = 40$), there remains the value of the pressure term at the upper edge X_2 of the integration domain which represents an external perturbation coming from the outer flow. The exact form of the general equations is given in Appendix A.

6. Energy transfer model

The exact form of the equations obtained from the decomposition, truncated at some cutoff point (k_{1c}, k_{3c}, n_c), does not account for the energy transfer between the resolved (included) modes and the unresolved smaller scales. The influence of the missing scales will be parameterized by a simple generalization of the Heisenberg spectral model in homogeneous turbulence. Such a model is fairly crude, but we feel that its details will have little influence on the behaviour of the energy-containing scales, just as the details of a subgrid-scale model have relatively little influence on the behaviour of the resolved scales in a large-eddy simulation. This is a sort of St. Venant's principle, admittedly unproved here, but amply demonstrated experimentally by the universal nature of the energy-containing scales in turbulence in diverse media having different fine structures and dissipation mechanisms (see Tennekes & Lumley 1972 for a fuller discussion). The only important parameter is the amount of energy absorbed.

We begin by defining a moving spatial filter which removes from the total field the unresolved modes. The details of the definition are not important – it is sufficient to conceive of the possibility of such a filter. This filter is also an averaging operator. The velocity field may now be divided into the resolved and unresolved field by using this filter. The Reynolds stress of the unresolved field may now be defined as the average using our filter operator, of the product of the unresolved velocities; this acts on the resolved field. We suppose that the deviator of this Reynolds stress is proportional to the strain rate of the resolved field. We neglect the Leonard stresses, which essentially supposes that there is more of a spectral gap than really exists. This is what is done in the Heisenberg model, without ill effect. The way in which we are treating the effect of the unresolved modes on the resolved ones is very much like what is done in large-eddy simulation, and is called subgrid-scale modelling; our model would probably be called a Smagorinsky model (there are minor differences in the definition of the equivalent transport coefficient). Let us agree to designate the resolved field as $u_{i<}$ and the unresolved field as $u_{i>}$, while an average of ϕ, say, over the unresolved modes (the filtering process) can be designated as $\langle \phi \rangle_>$. Thus:

$$\tau_{ij>} = -2\alpha_1 \nu_T S_{ij<} \tag{21}$$

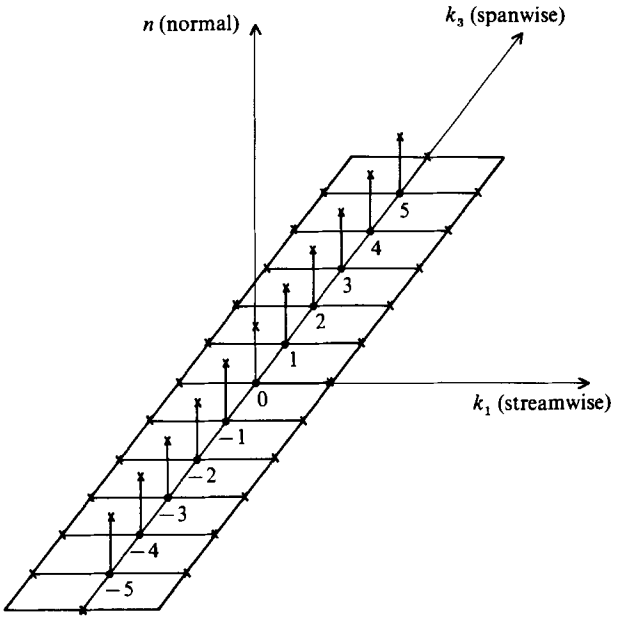

FIGURE 5. Inhomogeneous Heisenberg model applied to the specific truncation of §7: ●, resolved modes; ×, first neglected modes which are considered for the computation of the characteristic scales of the Heisenberg model.

with $$\tau_{ij>} = \langle u_{i>}\, u_{j>}\rangle_{>} - \langle\langle u_{i>}\, u_{j>}\rangle_{>}\rangle - \tfrac{1}{3}\delta_{ij}(\langle u_{k>}\, u_{k>}\rangle_{>} - \langle\langle u_{k>}\, u_{k>}\rangle_{>}\rangle)$$

and $$S_{ij<} = \tfrac{1}{2}(u_{i<,j} + u_{j<,i}).$$

Here $<$ denotes the sum over all the modes (k_1, k_3, n) such that $k_1 \leqslant k_{1c}$, $k_3 \leqslant k_{3c}$, $n \leqslant n_c$ and $>$ denotes the sum over all the modes (k_1, k_3, n) such that $k_1 > k_{1c}$ or $k_3 > k_{3c}$ or $n > n_c$, where (k_{1c}, k_{3c}, n_c) is the cutoff mode. The characteristic scales of the parameter ν_T are those of the higher modes. We have introduced an explicit dimensionless parameter α_1, and will exclude adjustable constants from ν_T. By observation that the energy decreases rapidly with increasing n and $\boldsymbol{k}$ (figure 2), we assume that these relevant scales are given by characteristic scales of the *first* neglected modes. This is probably a good approximation as far as the eigenmodes are concerned since they are separated by large gaps in the spectrum and it is a reasonable assumption for the Fourier modes since the steps of our Fourier series are also large.

Finally, the parameter ν_T is taken equal to

$$u_> l_> = \frac{\displaystyle\int_0^{X_2} \langle u_{i>}\, u_{i>}\rangle \, \mathrm{d}x_2}{\left(X_2 \displaystyle\int_0^{X_2} \langle u_{i>,j}\, u_{i>,j}\rangle \, \mathrm{d}x_2\right)^{\frac{1}{2}}} \tag{22}$$

(where $u_>$ and $l_>$ are characteristic scales of the neglected modes). This can be expressed in terms of the eigenvalues and eigenfunctions of the first neglected modes in the three directions (see Appendix B and figure 5.)

We shall refer to α_1 as a Heisenberg parameter. We shall adjust α_1 upward and downward to simulate greater and smaller energy loss to the unresolved modes, corresponding to the presence of a greater or smaller intensity of smaller-scale turbulence in the neighbourhood of the wall. This might correspond, for example, to the environment just before or just after a bursting event, which produces a large burst of small-scale turbulence, which is then diffused to the outer part of the layer.

A term $-\frac{1}{3}\delta_{ij}(\langle u_{k>}\, u_{k>}\rangle_{>} - \langle\langle u_{k>}\, u_{k>}\rangle_{>}\rangle)$ appears in the equation for the resolved field. This term could be combined with the pressure term and would not have any dynamical effect if the integration domain covered the entire flow volume. In our case, it needs to be computed since, like the pressure term, it leads to a term evaluated at X_2. We assume that the deviation (on the resolved scale) in the kinetic energy of the unresolved scales is proportional to the rate of loss of energy by the resolved scales to the unresolved scales. This pseudopressure term gives some quadratic feedback expressed in Appendix B. The rate of loss of energy from the resolved scales to the unresolved scales is $2\alpha_1 \nu_T S_{ij<} S_{ij<}$, so that a free parameter appears also in this term. Because this approximation involves a further assumption, and to give ourselves greater flexibility, we call this parameter α_2, although in all work presented in this paper, we have set $\alpha_1 = \alpha_2$ (see § 9, below).

Thus the Heisenberg model introduces two parameters in the system of equations, one, α_1, in the linear term, the other one, α_2, in the quadratic term. The equations therefore have the following form:

$$\frac{\mathrm{d}a^{(n)}_{k_1 k_3}}{\mathrm{d}t} = L + (\nu + \alpha_1 \nu_T)\, L' + Q + \alpha_2 Q' + C, \tag{23}$$

where L and L' represent the linear terms, Q the direct quadratic terms, Q' the quadratic pseudopressure term and C the cubic terms arising from the Reynolds stress.

7. Specific truncations

This study has two conflicting requirements. On one hand we wish to keep as few modes as possible in order to obtain a low-dimensional system, permitting us to apply the techniques of dynamical system analysis. On the other hand, we would like to retain at least a qualitatively correct dynamical representation of the turbulence production phenomenon. A necessary condition for the second requirement consists of including as much of the energy and Reynolds stress as possible in our system. This is already satisfied in the inhomogeneous direction by the proper orthogonal decomposition itself, since the first structure is the most energetic. Given the energetic gap between the two first eigenfunctions (figure 2), keeping only one structure seems quite reasonable. The choice of wavenumbers is now of great importance, especially as far as the Reynolds stress is concerned (an important part of the Reynolds stress is contained in the higher modes; see § 13). The best selection is probably the one for which the cutoff modes correspond to the experimental measurement cutoff. Since we retain only a few modes, the steps of our Fourier series are large. However, provided that the periodic length is larger than a few integral scales, the Fourier transform (as defined by (16)) of the autocorrelation tensor is unchanged and the eigenfunctions are still the same. The Heisenberg parameter is computed for a series of shorter steps and extrapolated.

We now seek a minimum truncation. The experimental results show that the ratio between the streamwise and spanwise characteristic lengthscales is of order ten (figure 2). Our first approximation therefore neglects streamwise variations, that is to say we truncate the series to the $k_1 = 0$ mode. We need at least three terms in the spanwise direction for nonlinear interactions. Thus the minimum truncation consists of one eigenmode, one streamwise wavenumber ($k_1 = 0$) and three (i.e. two active) spanwise wavenumbers $(0, k, 2k)$. In this paper, up to six spanwise wavenumbers $(0, \ldots, 5k)$ will be considered. In this case k has the value 3×10^{-3} and the lengths of the periodic box are $L_1 = L_3 = 333$. Even the model having six spanwise Fourier modes is still very crude, although the truncation seems to be the one that contains optimally large amount of the total energy among those of the same dimension. The zero cutoff mode in the streamwise direction in particular is a very rough approximation. Such a truncation causes a drop of the spanwise and normal root-mean-square values of the velocity which is particularly significant in the upper half of the layer. For this reason, we do not expect our velocity field reconstructed without rescaling to have more than qualitative significance.

We began with the smaller truncation, $k_1 = 0$ and $(0, k, 2k)$ in the spanwise direction, and one eigenmode. It must be noted that a certain level of complexity is necessary: such processes as vortex self-induction, vortex stretching and the like are nonlinear processes, and we expect to need three active Fourier modes in order to reproduce even qualitatively these effects. Hence, we were not very surprised when our smaller truncation was somewhat lacking in dynamically interesting behaviour (see below). We then moved to five active cross-stream modes, which produced a rich dynamical behaviour, which we will describe below. We are continuing to add modes, notably in the streamwise direction; to begin with, we removed two modes from the cross-stream direction, to see if the streamwise modes could produce the destabilizing influence on the $(0, 2k, 4k)$ set (equivalent to the $(0, k, 2k)$ set) that the addition of k, $3k$ and $5k$ to the cross-stream modes did (see below). We are proceeding cautiously, examining the symmetries and structure of the equations as we go, seeing what properties remain despite the greatly increased complexity. This extension is non-trivial, and will be described in detail elsewhere. It is mentioned here simply to make the point that we understand the properties (notably the symmetries) of the equations responsible for the behaviour observed; that the equations do not have these properties for lower-order truncations, and that the properties are preserved in higher-order truncations. Thus, we may expect the behaviour observed at the level of truncation studied here to continue to have its counterpart in higher-order truncations.

8. The model differential equations

As a preliminary approach, we study the set of equations given in Appendix B for a truncation limited to the first eigenfunction ($n = p = q = r = 1$), the zero streamwise wavenumber $k_1 = 0$ and up to six spanwise wavenumbers $k_3 = 0, k, \ldots, 5k$, for a suitably chosen k.

When only the zero streamwise wavenumber is considered, the equations become much simpler. Indeed, because of the symmetries of the eigenfunctions (Herzog 1986) in the (k_1, k_3) wavenumber plane, the first and second components are purely real and the third component is imaginary on the k_3-axis (i.e. for $k_1 = 0$). Using these symmetries, the equations for the complex modal coefficients $a^{(1)}_{k_1} = 0, k_3$ can be

readily derived. Letting k_3 take the values $jk, j = 0, 1, \ldots, 5$ and writing $a^{(1)}_{k_1=0,\, k_3=jk} = x_j + y_j$, a typical equation takes the form:

$$\begin{aligned}\frac{\mathrm{d}x_1}{\mathrm{d}t} &= a_1 x_1 + c_{-1,2}(x_1 x_2 + y_1 y_2) + c_{-2,3}(x_2 x_3 + y_2 y_3) + c_{-3,4}(x_3 x_4 + y_3 y_4) \\ &\quad + c_{-4,5}(x_4 x_5 + y_4 y_5) + x_1[d_{11}(x_1^2 + y_1^2) + d_{12}(x_2^2 + y_2^2) + d_{13}(x_3^2 + y_3^2) \\ &\quad + d_{14}(x_4^2 + y_4^2) + d_{15}(x_5^2 + y_5^2)]. \end{aligned} \tag{24}$$

The list of the coefficients $c_{k',\,k-k'}$ and $d_{kk'}$ is given in Appendix C. The values tabulated there are obtained by numerical evaluation of the integrals in the general equations of Appendix A.

In these equations the zero Fourier mode $a^{(1)}_{00} = x_0 + \mathrm{i}y_0$ has been removed since its imaginary part is identically zero and its real part decays to zero under the influence of the viscosity ($\mathrm{d}x_0/\mathrm{d}t = a_0 x_0$; $a_0 < 0$). The coefficients of the quadratic and cubic terms are each the sums of two quantities: $c_{k',\,k-k'}, c_{k-k',\,k}$ and $d_{k,\,k'}, d_{k,\,-k'}$. The influence of the Heisenberg model appears in the linear and quadratic terms as follows:

$$a_k = a^1_k + (1 + \alpha_1/Re_{\mathrm{T}})\, a^2_k, \quad c_{k',\,k-k'} = c^1_{k',\,k-k'} + \alpha_2\, c^2_{k',\,k-k'}$$

where α_1 and α_2 are the proportionality (Heisenberg) coefficients already mentioned in §6. The computation of the non-dimensionalized transport coefficient ν_{T} for this particular truncation gives the value $1/Re_{\mathrm{T}} = 6.28$.

6. Mathematical properties of the model ODEs

In this and the next section we present a preliminary analysis of the ODEs derived above. We concentrate on the case of six spanwise Fourier modes, for which the system has five 'active' modes, since the (linear) dynamics of the zero-wavenumber mode implies that it decouples from the non-zero modes and decays as $t \to +\infty$ (cf. §8). The equations are given in §8, and the numerical values of the coefficients a_j, $c_{i,j}$ and d_{ij} are given in Appendix C. Note that the first two (linear and quadratic) coupling terms depend upon the Heisenberg parameters α_1 and α_2. For simplicity, in this preliminary study we set $\alpha_1 = \alpha_2 = \alpha$ and vary the single parameter. Since α_2 is multiplied by small coefficients ($c_{i,j} = c^1_{i,j} + \alpha_2 c^2_{i,j}$ and typically $c^2_{i,j}/c^1_{i,j} \sim 0.05$), it has little effect on the equations and therefore we feel that little is lost in the simplification. We deal first with general properties of the equations, irrespective of precise values of coefficients.

9.1. *Global stability*

We first observe that the evolution equations are globally stable in the sense that solutions starting with sufficiently large initial conditions in the Euclidean norm $(\Sigma_j x_j^2 + y_j^2)^{\frac{1}{2}}$ decay and enter a compact trapping region. To see this, consider the Liapunov function

$$V(\boldsymbol{x}, \boldsymbol{y}) = \frac{1}{2} \sum_{j=1}^{5} (x_j^2 + y_j^2) \tag{25}$$

and differentiate along solution curves of (24) to obtain

$$\frac{\mathrm{d}V}{\mathrm{d}t} = \sum_{j=1}^{5} (x_j^2 + y_j^2) \left(a_j + \sum_{k=1}^{5} d_{jk}(x_k^2 + y_k^2) \right) + C(\boldsymbol{x}, \boldsymbol{y}), \tag{26}$$

where C is a cubic form in $\boldsymbol{x}$ and $\boldsymbol{y}$. Since all the coefficients d_{jk} are negative, for a sufficiently large value of the Euclidean norm and any Heisenberg parameter $\alpha \geqslant 0$, the quadratic terms dominate and $\mathrm{d}V/\mathrm{d}t < 0$. Thus all level sets $V =$ constant, sufficiently large, are crossed inwards by solutions. This stability result reflects the physical 'feedback' effect of the model in which the growth of the perturbations reduces the slope of the mean velocity profile (cf. §5). The global stability result holds for any number of spanwise modes.

9.2. *Invariant subspaces*

The ODEs have several important invariant subspaces and symmetries, which reflect physical symmetries of the flow and lead to simplifications in analysis. The flow is invariant under infinitesimal streamwise and spanwise translations $x_i \to x_i + \beta_i$, $i = 1, 3$, and spanwise reflections $x_3 \to -x_3$. Since only the zero-wavenumber streamwise mode is retained in our model, the former does not appear, but the latter leads to an $O(2)$-symmetry which is most easily seen by passing to polar coordinates $r_j = (x_j^2 + y_j^2)^{\frac{1}{2}}$, $\theta_j = \tan^{-1}(y_j/x_j)$. The equations then take the form

$$\left.\begin{aligned} \dot{r}_j &= (a_j + \sum_k d_{jk} r_k^2)\, r_j + \sum_k c_{j,k}(\boldsymbol{r}) \cos\phi_k, \\ r_j \dot{\theta}_j &= \sum_k \underline{c}_{j,k}(\boldsymbol{r}) \sin\phi_k, \end{aligned}\right\} \tag{27}$$

where (for six modes) $\phi_j = \theta_1 + \theta_j - \theta_{j+1}$ $(j = 1, 2, 3, 4)$, $\phi_5 = 2\theta_2 - \theta_4 = \phi_2 + \phi_3 - \phi_1$ and $\phi_6 = \theta_2 + \theta_3 - \theta_5 = \phi_3 + \phi_4 - \phi_1$. Here the $\underline{c}_{j,k}$ are the same as the quadratic coefficients $c_{j,k}$ of the original equations, up to some sign changes (cf. (29), below, for an example).

We observe that only certain phase differences appear and that all the ϕ_j are invariant under the symmetry $\theta_j \to \theta_j + j\beta$, corresponding to translation in x_3. For six modes, only four phase differences $\phi_1, \ldots, \phi_4$ appear in the ODEs for the five active modes $r_1, \ldots, r_5$. Thus we find S^1-families of solutions: for example, if the r_j, ϕ_j equations have a fixed point with $r_j > 0$ for some j, and $\phi_j = 0$ or π for all j, the full r_j, θ_j or x_j, y_j equations have a *circle* of fixed points.

A second important invariance is that of the 2–4 subspace. If $x_j = y_j = 0$ for $j = 1, 3, 5$ then the evolution equations show that $\mathrm{d}x_j/\mathrm{d}t = \mathrm{d}y_j/\mathrm{d}t = 0$ for $j = 1, 3, 5$ and the dynamics reduces to

$$\left.\begin{aligned} \dot{x}_2 &= (a_2 + d_{22}(x_2^2 + y_2^2) + d_{24}(x_4^2 + y_4^2))\, x_2 + c_{4,-2}(x_4 x_2 + y_4 y_2), \\ \dot{y}_2 &= (a_2 + d_{22}(x_2^2 + y_2^2) + d_{24}(x_4^2 + y_4^2))\, y_2 + c_{4,-2}(x_2 y_4 - x_4 y_2), \\ \dot{x}_4 &= (a_4 + d_{42}(x_2^2 + y_2^2) + d_{44}(x_4^2 + y_4^2))\, x_4 + c_{2,2}(x_2^2 - y_2^2), \\ \dot{y}_4 &= (a_4 + d_{42}(x_2^2 + y_2^2) + d_{44}(x_4^2 + y_4^2))\, y_4 + 2c_{2,2}(x_2 y_2), \end{aligned}\right\} \tag{28}$$

or, in polar coordinates:

$$\left.\begin{aligned} \dot{r}_2 &= (a_2 + d_{22} r_2^2 + d_{24} r_4^2 + c_{4,-2} r_4 \cos\phi_5)\, r_2, \\ \dot{r}_4 &= (a_4 + d_{42} r_2^2 + d_{44} r_4^2)\, r_4 + c_{2,2} r_2^2 \cos\phi_5, \\ \dot{\phi}_5 &= -(2c_{4,-2} r_4 + c_{2,2} r_2^2 / r_4) \sin\phi_5, \end{aligned}\right\} \tag{29}$$

where $\phi_5 = 2\theta_2 - \theta_4$. This subsystem has a fixed point $r_2, r_4, \phi_5 = \pi$, which for the parameter values of primary interest is the only stable one (when it exists: see §9.3 below). In this range $(1.32 < \alpha < 1.61)$ the origin $(r_2, r_4) = 0$ is completely unstable

and $r_2 = 0$, $r_4 = (-a_4/d_{44})^{\frac{1}{2}}$ is a saddle point. We observe that this subsystem (together with the 'trivial' mode $\dot{r}_0 = a_0 r_0$) is identical in form to the minimal 3-mode truncation mentioned in §7. We will return to this subsystem in 9.4.

The third invariance is that of the purely real system $y_j = 0$, $\forall j$, for which the equations reduce to

$$\left.\begin{aligned}
\dot{x}_1 &= (a_1 + \sum_j d_{1j} x_j^2)\, x_1 + c_{-1,2} x_1 x_2 + c_{-2,3} x_2 x_3 + c_{-3,4} x_3 x_4 + c_{-4,5} x_4 x_5,\\
\dot{x}_2 &= (a_2 + \sum_j d_{2j} x_j^2)\, x_2 + c_{1,1} x_1^2 + c_{3,-1} x_1 x_3 + c_{4,-2} x_2 x_4 + c_{5,-3} x_3 x_5,\\
\dot{x}_3 &= (a_3 + \sum_j d_{3j} x_j^2)\, x_3 + c_{1,2} x_1 x_2 + c_{4,-1} x_1 x_4 + c_{5,-2} x_2 x_5,\\
\dot{x}_4 &= (a_4 + \sum_j d_{4j} x_j^2)\, x_4 + c_{1,3} x_1 x_3 + c_{2,2} x_2^2 + c_{5,-1} x_1 x_5,\\
\dot{x}_5 &= (a_5 + \sum_j d_{5j} x_j^2)\, x_5 + c_{1,4} x_1 x_4 + c_{2,3} x_2 x_3.
\end{aligned}\right\} \tag{30}$$

In view of the first invariance noted above, any rotation $\theta_j \to \theta_j + j\beta$ of this subspace is also invariant; in particular for $\beta = \frac{1}{2}\pi$ one obtains the y_1, x_2, y_3, x_4, y_5 subsystem from (30) by replacing variables according to $x_1 \to y_1$, $x_2 \to -x_2$, $x_3 \to -y_3$, $x_4 \to x_4$, $x_5 \to y_5$. This last symmetry corresponds to the physical situation of structures invariant under reflection about a plane $x_3 = \text{const}$. It will be especially useful in our discussion of homoclinic orbits and 'intermittency' in §10.

9.3. *Behaviour for large* α

Since each linear coefficient has the form $a_j = a_j^1 + (1 + \alpha/Re_\tau)\, a_j^2$ and $a_j^2 < 0$ for all j, there exists a critical value of α above which all coefficients are negative. For the six-mode model this is $\alpha = \alpha_c \sim 2.409$ and the last coefficient to become negative as α increases is a_2. Therefore for $\alpha > \alpha_c$ the trivial solution $x_j = y_j = 0$ is a stable fixed point, since the eigenvalues of the system linearized at this point are $\lambda_j = a_j$, each with multiplicity 2.

The indefiniteness of quadratic terms such as $c_{-j,j+1}(x_j x_{j+1} + y_j y_{j+1})$ makes it difficult to immediately rule out the existence of additional stable or unstable fixed points for $\alpha > \alpha_c$, although, since all cubic coefficients d_{jk} are negative, it is easy to see that no 'pure' modes of the form $r_j \neq 0$, $r_i = 0$, $i \neq j$ exist for $\alpha > \alpha_c$. However, for example, on the 2–4 subspace it is fairly easy to show that no non-trivial steady modes can exist, by a simple *reductio ad absurdum* argument (Aubry *et al.* 1987). Therefore, for $\alpha > \alpha_c \sim 2.409$, the 2–4 system has a unique globally stable fixed point $r_2 = r_4 = 0$. Similar arguments show that for sufficiently large α the trivial solution $\boldsymbol{r} = 0$ is the unique global attractor for the full system. Of course, this merely confirms our physical intuition that increased loss to unresolved modes promotes steady 'stable' behaviour.

9.4. *Bifurcation as* α decreases

The arguments outlined above suggest that, as α decreases and the coefficients a_j in turn become positive, bifurcations may occur in which non-trivial fixed points branch off the trivial solution. To illustrate this, we consider the bifurcations occurring in the 2–4 subspace, bifurcations in which solutions having $r_1 = r_3 = r_5 = 0$ are created. Clearly $r_2 = r_4 = 0$ is a solution of (29) for all α: it is merely the trivial solution of the full problem and is a stable sink (in $r_2 - r_4$ space) for $\alpha > 2.409$

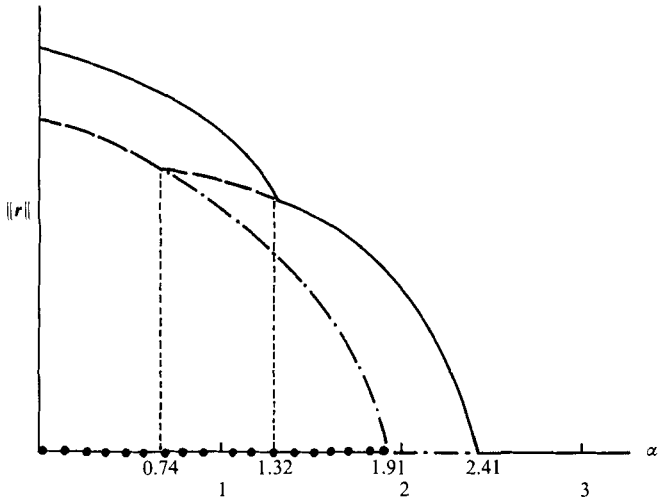

FIGURE 6. Schematic bifurcation diagram for the 2–4 subsystem, equations (28) and (29): ——, sinks; – – –, saddles with one positive eigenvalue; –·–·–, saddles with two positive eigenvalues; · · · ·, sources. Note that non-trivial branches correspond to circles of solutions, and one of their eigenvalues is always 0.

$(a_2, a_4 < 0)$, a saddle for $1.94 < \alpha < 2.409$ $(a_4 < 0 < a_2)$ and a source for $0 < \alpha < 1.94$ $(a_4, a_2 > 0)$. Since $r_2 = r_4 = 0$, the phase aqngles θ_2, θ_4 and hence the phase difference ϕ_5 are irrelevant for this solution. A second family of solutions with $r_4 = (-a_4/d_{44})^{\frac{1}{2}}$, $r_2 = 0$ bifurcates from the trivial solution at $\alpha \sim 1.94$ $(a_4 = 0)$ and exists for all $0 \leqslant \alpha < 1.94$. This solution corresponds to a 'pure' mode of spatial wavenumber 4, and since the polar coordinate representation is singular for $r_2 = 0$, its stability must be investigated by linearizing the Cartesian equation (28). An elementary calculation yields a matrix with eigenvalues $a_2 - a_4 d_{24}/d_{44} \pm c_{4,-2}(-a_4/d_{44})^{\frac{1}{2}}$, $-2a_4 < 0$ and 0, the eigenvector of the latter being tangent to the circle of fixed points $x_4^2 + y_4^2 = -a_4/d_{44}$, $x_2 = y_2 = 0$ (see §9.5 below). These solutions are saddle points with two positive eigenvalues for $0.74 < \alpha < 1.94$ and one positive eigenvalue for $0 \leqslant \alpha < 0.74$. At $\alpha = 1.94$ this branch of solutions coalesces with the trivial branch.

A third branch of equilibrium solutions bifurcates from the origin at $\alpha = 2.409$. Here both amplitude components r_2 and r_4 are non-zero, and so the phase difference equation must be satisfied either by setting $\sin\phi_5 = 0 \Rightarrow \phi_5 = 2\theta_2 - \theta_4 = 0, \pi$ or $2c_{4,-2} r_4^2 + c_{2,2} r_2^2 = 0$. The branch in question has $\phi_5 = \pi$ and is stable for $1.32 < \alpha < 2.409$. At $\alpha \sim 1.32$ it becomes a saddle point with unstable eigenvector in the ϕ_5-direction: thus at this point we expect a bifurcation to a fourth family of solutions having $\phi_5 \neq \pi$ (and $\neq 0$). The third branch continues to exist until α reaches 0.74 when it coalesces with the second branch described above.

At $\alpha = 1.32$ a fourth branch of solutions emerges from the third branch; this branch exists for all $\alpha < 1.32$ and has $r_2, r_4 \neq 0$, but the phase equation is satisfied by $2c_{4,-2} r_4^2 + c_{2,2} r_2^2 = 0$, thus $\phi_5 \neq 0, \pi$, as expected. This branch is stable. No solutions with $\phi_5 = 0$, $r_2, r_4 \neq 0$ exist for $\alpha > 0$. The overall behaviour can be represented by the bifurcation diagram of figure 6. These computations were verified by use of the bifurcation computation package AUTO (Doedel & Kernevez 1985). As we shall see in the next section, more exotic bifurcations involving periodic and homoclinic orbits occur for the full ten-dimensional system as α varies.

9.5. *Linearized stability of the 2–4 fixed point*

Since it will play an important role in interpreting the numerical simulations of the next section, we discuss the stability of the (circle of) fixed points $r_2, r_4 \neq 0$, $\phi_5 = 2\theta_2 - \theta_4 = \pi$, $r_1 = r_3 = r_5 = 0$, found above, in the context of the full 10-dimensional phase space. Without loss of generality we choose the representation on the purely real subspace. Since $r_2 = z_2$, $r_4 = z_4$ and $\phi_5 = \pi$ there are two such: $x_2 = \pm z_2$, $x_4 = -z_4$ and $x_1 = x_3 = x_5 = y_j = 0$, $j = 1, \ldots, 5$. Linearizing the full system in Cartesian coordinates at the first of these 'real' fixed points, we find that the 10×10 matrix block diagonalizes as follows, when the components are written in the sequence $(x_2, x_4; y_2, y_4; x_1, x_3, x_5; y_1, y_3, y_5)$:

$$(x_2, x_4) = \begin{bmatrix} a_2 + 3d_{22} z_2^2 + d_{24} z_4^2 - c_{4,-2} z_4 & c_{4,-2} z_2 - 2d_{24} z_2 z_4 \\ 2c_{2,2} z_2 - 2d_{42} z_2 z_4 & a_4 + d_{42} z_2^2 + 3d_{44} z_4^2 \end{bmatrix}, \tag{31a}$$

$$(y_2, y_4) = \begin{bmatrix} a_2 + d_{22} z_2^2 + d_{24} z_4^2 + c_{4,-2} z_4 & c_{4,-2} z_2 \\ 2c_{2,2} z_2 & a_4 + d_{42} z_2^2 + d_{44} z_4^2 \end{bmatrix}, \tag{31b}$$

$$(x_1, x_3, x_5) = \begin{bmatrix} a_1 + d_{12} z_2^2 + d_{14} z_4^2 + c_{-1,2} z_2 & c_{-2,3} z_2 - c_{-3,4} z_4 & -c_{-4,5} z_4 \\ c_{1,2} z_2 - c_{4,1} z_4 & a_3 + d_{32} z_2^2 + d_{34} z_4^2 & c_{5,-2} z_2 \\ -c_{4,1} z_4 & c_{2,3} z_2 & a_5 + d_{52} z_2^2 + d_{54} z_4^2 \end{bmatrix}, \tag{31c}$$

$$(y_1, y_3, y_5) = \begin{bmatrix} a_1 d_{12} z_2^2 + d_{14} z_4^2 - c_{-1,2} z_2 & c_{-2,3} z_2 + c_{-34} z_4 & -c_{-4,5} z_4 \\ c_{1,2} z_2 - c_{4,1} z_4 & a_2 + d_{32} z_2^2 + d_{34} z_4^2 & -c_{5,-2} z_2 \\ -c_{1,4} z_4 & c_{2,3} z_2 & a_5 + d_{52} z_2^2 + d_{54} z_4^2 \end{bmatrix}, \tag{31d}$$

At the second fixed point the matrix is obtained from (31) by letting $z_2 \to -z_2$. The reader can check that, under this transformation, the eigenvalues of both 2–4 subsystems remain invariant while those of the real and imaginary 1, 3, 5 subsystems are interchanged.

Substituting from the expressions (31) for r_2 and r_4, we find that the determinants and traces of the first two matrices are

$$\left.\begin{aligned} \det(x_2, x_4) &= 4(d_{22} d_{44} - d_{24} d_{42}) z_2^2 z_4^2 + 2z_2^2 (d_{22} c_{2,2} z_2^2 / z_4^2) \\ &\quad + (2d_{24} c_{2,2} + c_{4,-2} d_{42}) z_4 - c_{4,-2} c_{2,2}), \\ \operatorname{trace}(x_2, x_4) &= 2(d_{22} z_2^2 + d_{44} z_4^2) + c_{2,2} z_2^2 / z_4, \\ \det(y_2, y_4) &= 0, \\ \operatorname{trace}(y_2, y_4) &= 2c_{4,-2} z_4 + c_{2,2} z_2^2 / z_4. \end{aligned}\right\} \tag{32}$$

For all $0 \leqslant \alpha \leqslant 2.41$ we find that $\det(x_2, x_4) > 0$ and $\operatorname{trace}(x_2, x_4) < 0$ while $\operatorname{trace}(y_2, y_4)$ *is* < 0 for $\alpha > 1.32$ and > 0 for $\alpha < 1.32$, so that we always have two eigenvalues with negative real part and one with zero real part (recall that $z_4 > 0$, so that $x_4 = -z_4 < 0$). The latter corresponds to variations along the circle of (degenerate) fixed points $x_2^2 + y_2^2 = r_2^2$, $x_4^2 + y_4^2 = r_4^2$, $2\theta_2 - \theta_4 = \pi$; its eigenvector is tangent to this circle. This behaviour agrees, as it must, with the bifurcation study of the 2–4 system in §9.4, above. The remaining eigenvalues vary in the range $1.2 \leqslant \alpha \leqslant 1.65$ as indicated in table 1. Thus, for $\alpha > \alpha_b \sim 1.61$, the fixed points in question are stable,

α	x_2, x_4	y_2, y_4	x_1, x_3, x_5	y_1, y_3, y_5
1.2	−32.88, −2.538	0, +1.618	−7.318, 0.9764 ± 2.036i	−5.294 ± 2.096i, +1.065
1.3	−28.53, −3.108	0, +0.3838	−8.548, 0.7011 ± 1.991i	−6.916, −4.520, −0.0903
1.35	−26.53, −3.398	0, −0.2426	−9.227, 0.5839 ± 1.943i	−8.234, −3.525, −0.7460
1.4	−24.74, −3.737	0, −0.9142	−9.989, 0.4529 ± 1.875i	−9.326, −2.381, −1.867
1.45	−23.00, −4.072	0, −1.530	−10.76, 0.3434 ± 1.780i	−10.31, −2.137 ± 1.118i
1.5	−21.40, −4.425	0, −2.158	−11.57, 0.2375 ± 1.713i	−11.26, −2.168 ± 1.479i
1.55	−19.87, −4.797	0, −2.769	−12.40, 0.1362 ± 1.616i	−12.18, −2.206 ± 1.692i
1.6	−18.43, −5.203	0, −3.382	−13.26, 0.0291 ± 1.506i	−13.11, −2.255 ± 1.826i
1.61	−18.15, −5.284	0, −3.501	−13.44, 0.0093 ± 1.483i	−13.29, −2.263 ± 1.846i
1.63	−17.57, −5.440	0, −3.727	−13.77, −0.0248 ± 1.438i	−13.64, −2.273 ± 1.878i
1.65	−17.04, −5.613	0, −3.972	−14.12, −0.0684 ± 1.386i	−14.01, −2.294 ± 1.904i

TABLE 1. Eigenvalues of the fixed point $x_2 = \imath_2$, $x_4 = -\imath_4$, $x_1 = x_3 = x_5 = y_j = 0$

while for $1.32 < \alpha < \alpha < \alpha_b$ they are saddle points with two-dimensional unstable manifolds. The numerical computations described in the next section suggest that this circle of fixed points is the unique global attractor for $1.61 \leqslant \alpha \leqslant 2$, but for $2.0 \leqslant \alpha \leqslant 2.3$ these fixed points are again unstable, with a single positive eigenvalue. However, slight variation of the coefficients removes this unstable range, while not significantly altering the lower range, and so we do not discuss it further. From $\alpha = 2.3$ to 2.41, where they coalesce with the trivial solution, these points are again globally stable.

The linear analysis above shows that the fixed point $x_2 = +\imath_2$, $x_4 = -\imath_4$(denoted $\boldsymbol{r}^+$) undergoes a Hopf bifurcation (Marsden & McCracken 1976; Guckenheimer & Holmes 1983, §3.4) as α passes through α_b. In doing so, for $\alpha < \alpha_b$ it becomes a saddle point with a two-dimensional unstable manifold $W^u(\boldsymbol{r}^+)$ which, in view of the global invariance noted in §9.2, must lie in the subspace spanned by x_1, x_3 and x_5 (i.e. $x_2 = x_4 = y_j = 0$). We have not computed the Hopf stability coefficient (a_1 of Guckenheimer & Holmes 1983, §3.4): V''' of Marsden & McCracken 1976, §4), and so cannot say whether the limit cycles thus created exist for $\alpha < a_b$ or $\alpha > \alpha_b$, but since no small stable periodic orbits are observed near $\boldsymbol{r}^+$, we conjecture that an unstable (saddle-type) periodic orbit exists for $\alpha > a_b$, and that the bifurcation is therefore subcritical. The S^1 symmetry implies that the Hopf bifurcation occurs for every point on the circle of fixed points $r_2 = \imath_2$, $r_4 = \imath_4$, $r_1 = r_3 = r_5 = 0$ and that we have an S^1 family of limit cycles.

We will return to the behaviour of the eigenvalues for lower α in the next section.

10. Numerical simulations and further analysis of the model ODEs

Numerical integrations of 3-, 4-, 5- and 6-mode models have been carried out, but we shall only report in detail on the 6-mode (5 active mode) simulations here. A fourth-order Runge–Kutta method was used with double precision arithmetic and integrations were carried out on a SUN 150 workstation and a GOULD (for large runs) using 'C' routines under a Berkeley 4.2 UNIX operating system. The algorithms were checked by integrating from initial conditions chosen to select the various invariant subspaces discussed in §9.2. A fixed stepsize of 0.02 was used for the computations reported here: it was found that stepsizes below 0.03–4 gave indistinguishable results.

Heisenberg parameter, α	Behaviour
0.41–0.7	Periodic orbit r_j = constant $\neq 0$, ϕ_j = constant, $\mathrm{d}\theta_j/\mathrm{d}t$ = constant $\neq 0$.
0.7–1.0	Quasi-periodic behaviour, $\mathrm{d}r_j/\mathrm{d}t$ bounded $\neq 0$, ϕ_j = constant, $\mathrm{d}\theta_j/\mathrm{d}t$ = constant $\neq 0$.
1.0–1.3	Complex transition from quasi-periodic to intermittent behaviour. Phases ϕ_j still drift.
1.3–1.61	Intermittency, described below.
1.61–2.41	Unique stable fixed point $r_2, r_4 \neq 0$, $r_1 = r_3 = r_5 = 0$, $r_2, r_4 \to 0$ as α increases with window of instability from 2.0–2.3.
$\alpha > 2.41$	Trivial solution $r_j = 0$, $\forall j$, is the global attractor.

TABLE 2. Qualitative dynamical behaviour of the 6-mode model

10.1. *General behaviour*

We start by outlining the behaviour of typical solutions of the equations as α, the Heisenberg parameter, is reduced. For $1.61 < \alpha < 2.0$ we find an apparently unique circle of globally stable fixed points at which $x_j = y_j = 0$ for $1, 3, 5$ and $r_2 = (x_2^2 + y_2^2)^{\frac{1}{2}}$, $r_4 = (x_4^2 + y_4^2)^{\frac{1}{2}} \neq 0$ with $\phi_5 = 2\theta_2 - \theta_4 = \pi$. For $2.0 < \alpha < 2.3$ the fixed points are unstable and weak intermittency, like that described later for $\alpha < 1.61$, occurs. For $2.3 < \alpha < 2.41$ one again has global stability. In view of the analytical results of §9, this is not surprising. As we shall see in §12, this solution corresponds to a steady structure of streamwise vortex pairs. As α increases, the amplitudes of the components become smaller, and the trivial solution $x_j = y_j = 0$, $\forall j$ is the unique, attracting fixed point for $\alpha \geqslant 2.41$, see figure 8. As α is reduced below 1.61, the fixed points become unstable, as predicted by the linear theory of §9.5, and 'intermittent' behaviour is observed. We discuss this in detail below, since it appears to be most relevant to the dynamics of coherent structures in the boundary layer. The intermittent behaviour persists until $\alpha \sim 1.35$.

For α between ~ 0.7 and ~ 1.0 we observe quasi-periodic and, for $\alpha \sim 1.0$–1.3, more complex and possibly chaotic motions. For $\alpha \sim 0.7$–0.9 there is reasonably clear evidence of an invariant two-dimensional torus in the phase space. As α decreases, one of the radii of this torus shrinks and the behaviour is dominated by a single oscillating mode for $\alpha \sim 0.4$–0.7. Thus, a Hopf bifurcation from a periodic orbit to a two-torus appears to occur at $\alpha \sim 0.7$. An interesting characteristic of the periodic and quasi-periodic and complex motions in the range $\alpha \sim 0.4$–1.0 is that the phase differences ϕ_j remain constant, but at values $\neq 0$ or π so that the components $\sin\phi_j$ of the phase evolution equations (27) are non-zero . Thus the phases θ_j drift, at constant speeds, while the moduli r_j remain constant (for periodic motions) or oscillate periodically (for quasi-periodic motions). This is a natural consequence of the $O(2)$-symmetry, cf. Armbruster, Guckenheimer & Holmes (1988). Such motions correspond to lateral (spanwise) drift of the streamwise vortices: travelling waves in the boundary layer. Note that the fourth branch of solutions in the r_2–r_4 subspace found for $\alpha < 1.32$ in §9.4 has $\phi_5 \neq 0$ and that θ_2 and θ_4 drift constant speed for that mode. Although the eigenvalue computations of §9.5 and the simulations indicate that this 'pure' 2–4 solution is unstable to perturbations in r_1, r_3, r_5, it probably plays an important role in the evolution of these 'travelling wave' solutions.

For $\alpha \sim 0.41$, quasi-periodic motions are observed again, but below $\alpha \sim 0.4$ the behaviour is more complex and we have not carried out enough integrations in this

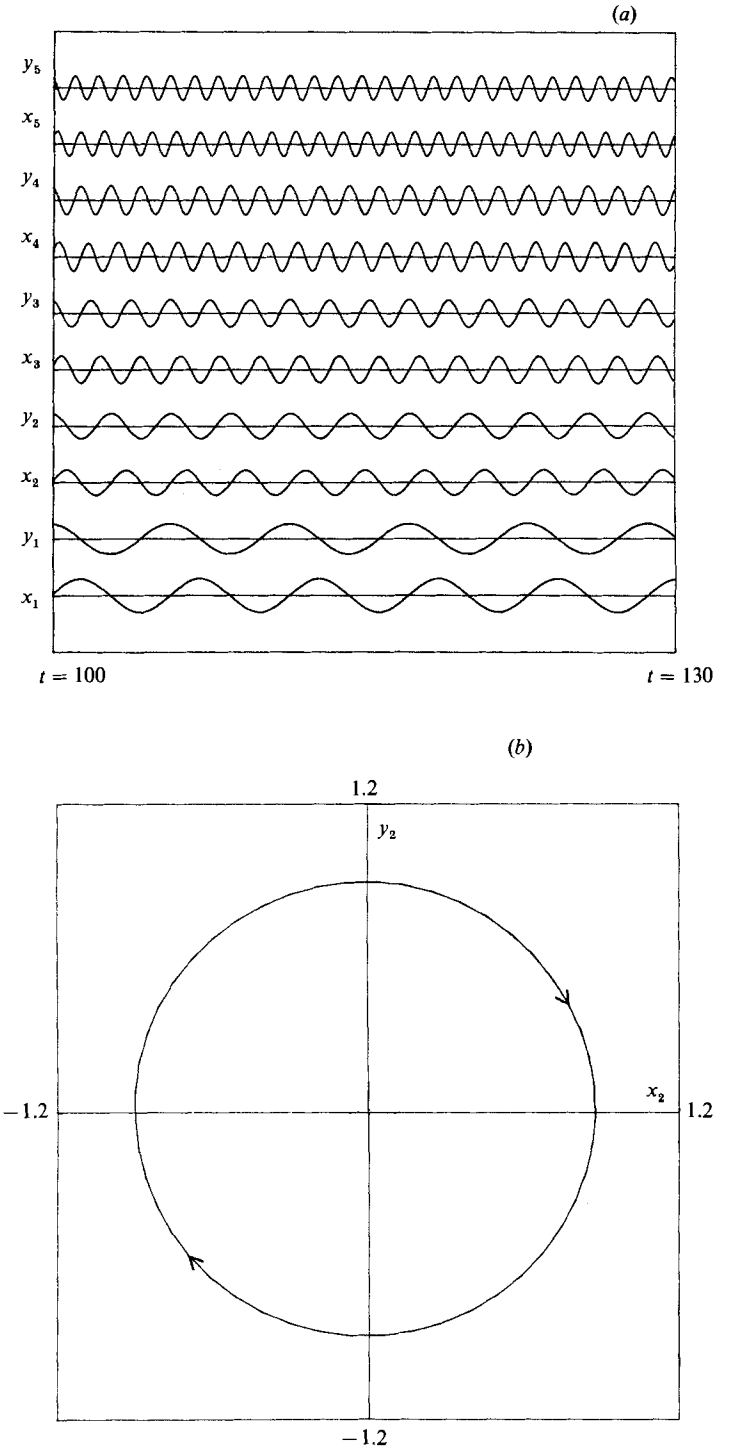

FIGURE 7(a, b). For caption see page 142.

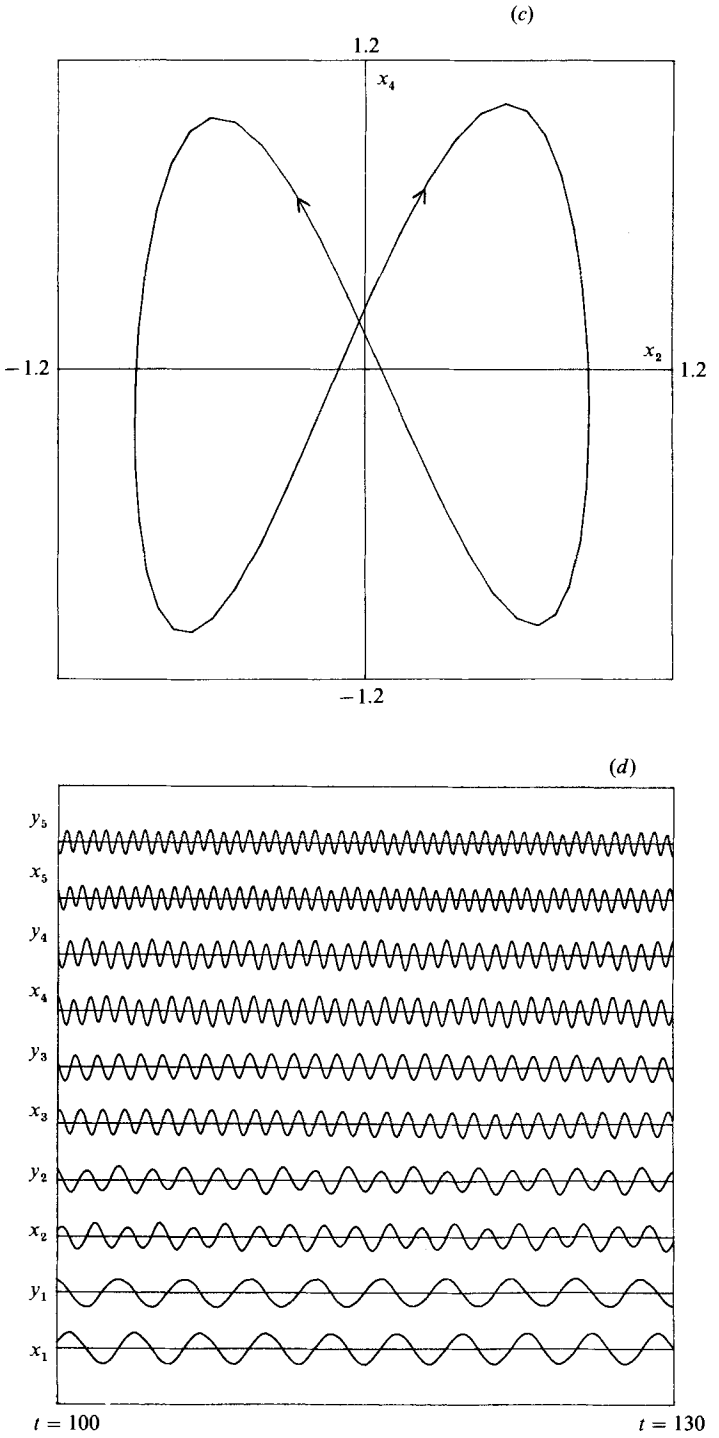

FIGURE 7 (*c*, *d*). For caption see page 142.

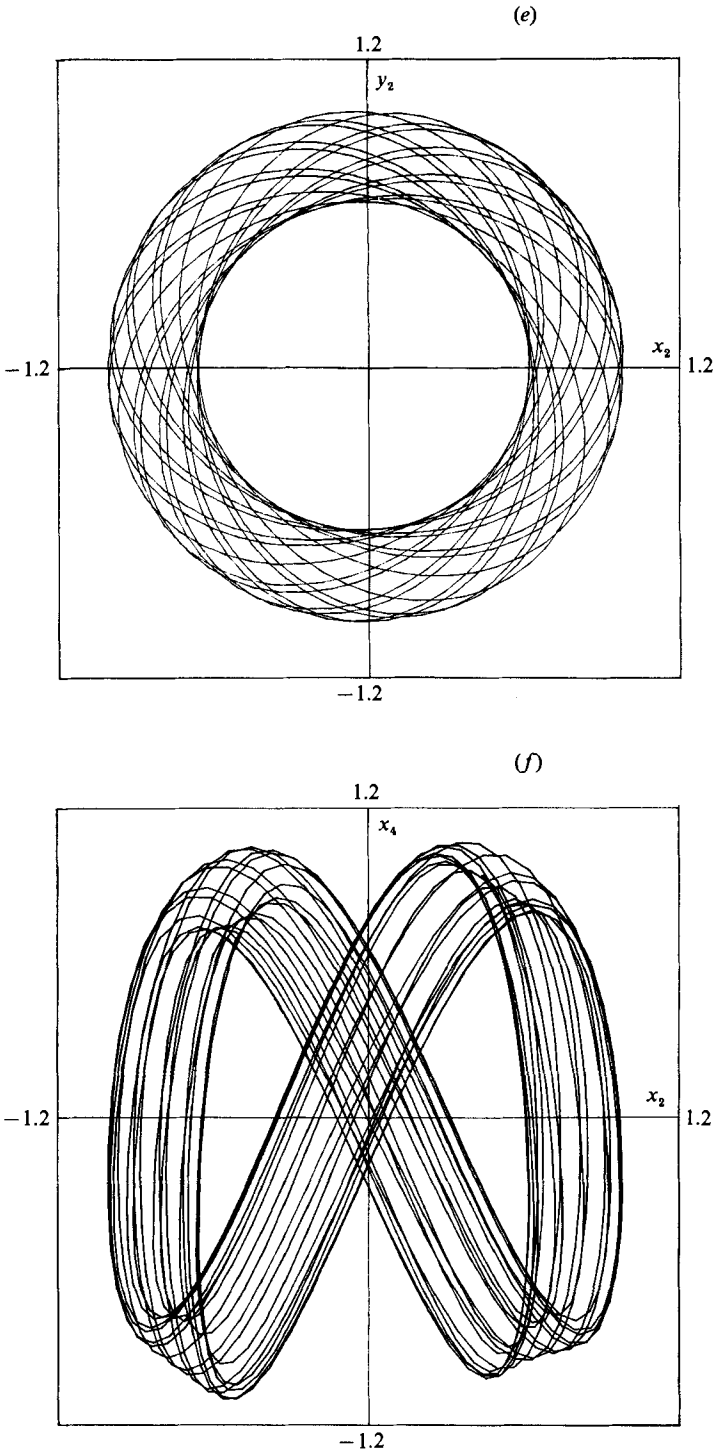

FIGURE 7. Time histories of the modal components $x_1, \ldots, y_5$ and selected projections of phase planes: (a, b, c) Heisenberg parameter $\alpha = 0.7$: note steady periodic motion with uniformly rotating phase: (d, e, f), $\alpha = 0.9$: Note quasi-periodic motion with rotating phase.

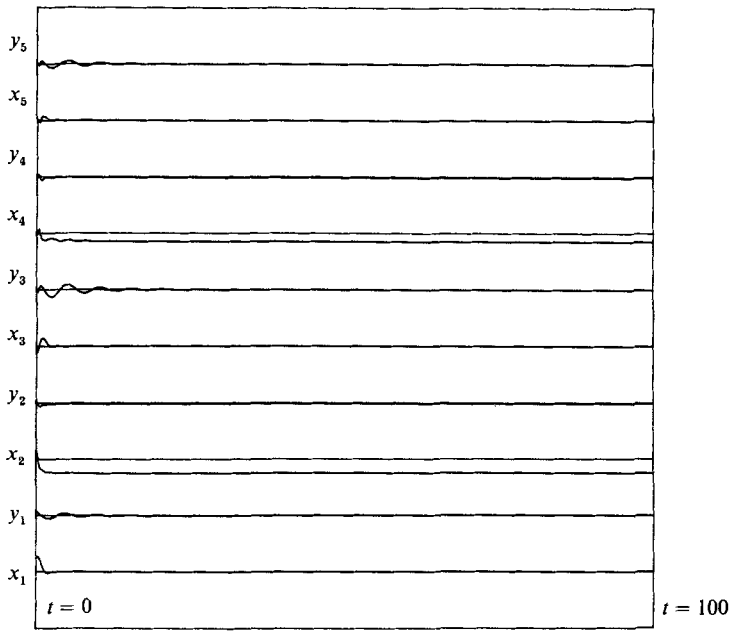

FIGURE 8. Time histories for Heisenberg parameter $\alpha = 1.7$, showing stable fixed point.

region to determine it. We summarize in table 2. The existence of some of these solutions – notably the travelling waves and quasi-periodic motions – follow from rather general group theoretic considerations, cf. papers on $O(2)$-symmetry in Golubitsky & Guckenheimer (1986), and Armbruster *et al.* (1988). Also see §13. We intend to pursue the group theoretic issues in detail in subsequent work.

Figure 7 shows examples of time histories of solutions for $\alpha = 0.7$ and $\alpha = 0.9$; projections of the solutions into the x_1, y_1 and x_2, x_4 'phase-planes' are also shown, to illustrate the phase drift behaviour. Figure 8 shows time histories for $\alpha = 1.7$, illustrating the presence of a stable fixed point.

For the present study, however, the intermittent behaviour exhibited by the six-mode model for α between 1.35 and 1.61 appears to be of greatest interest, since it corresponds in a fairly clear way to the physical instability, sweep and ejection event observed in boundary-layer experiments (cf. §1 and see §12, below). We now describe this intermittent behaviour, starting with some general remarks.

10.2. *Intermittency*

In the theory of dynamical systems three types of intermittency have been distinguished (Pomeau & Manneville 1980). They are associated with solutions repeatedly passing close to a weakly unstable fixed point or periodic orbit. The solution spends a long 'laminar' phase near the point or orbit until it reaches a critical amplitude and a brief turbulent 'burst' ensues, in which it travels far and fast in phase space before returning. (These terms were appropriated by the dynamical-systems community and have been used in a predominantly metaphorical fashion thus far.) The laminar phase is governed by the linearized dynamics near the fixed point or periodic orbit, but the burst and return are associated with a 'global reinjection mechanism', usually a homoclinic orbit or heteroclinic cycle (Tresser,

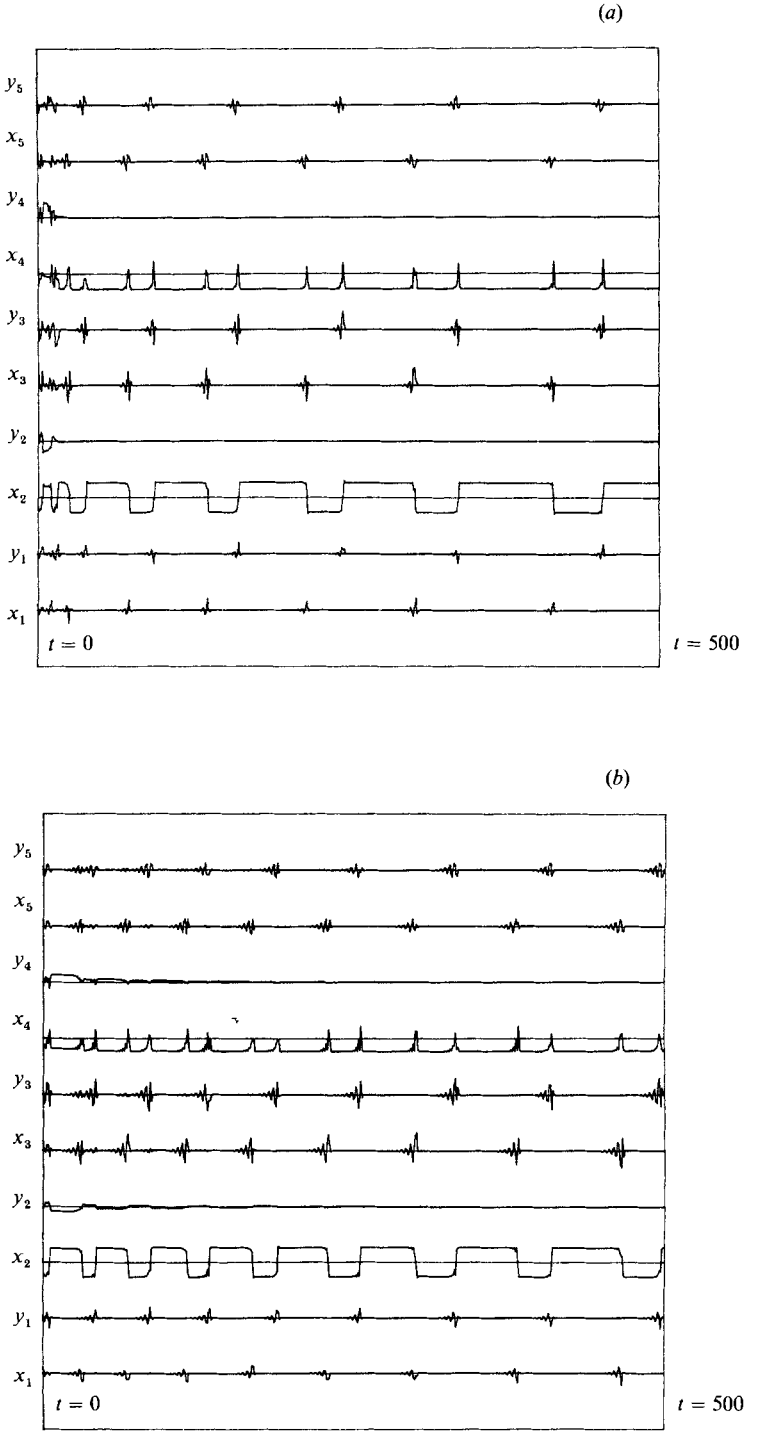

FIGURE 9(*a*, *b*). For caption see page 146.

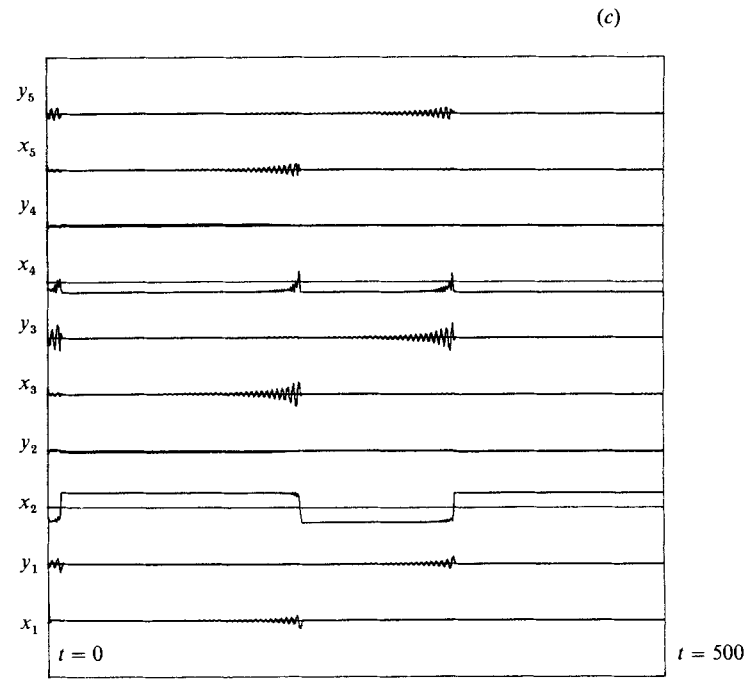

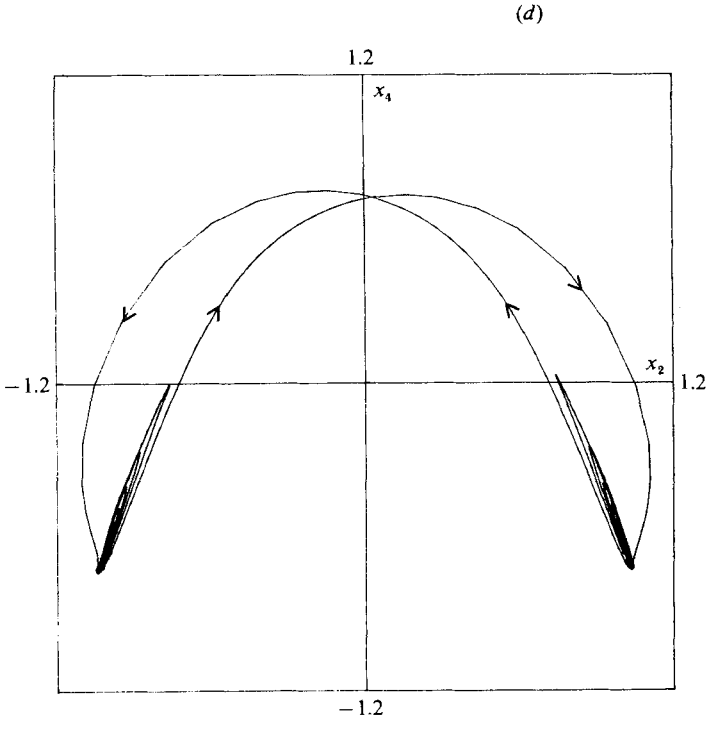

FIGURE 9(*c*, *d*). For caption see page 146.

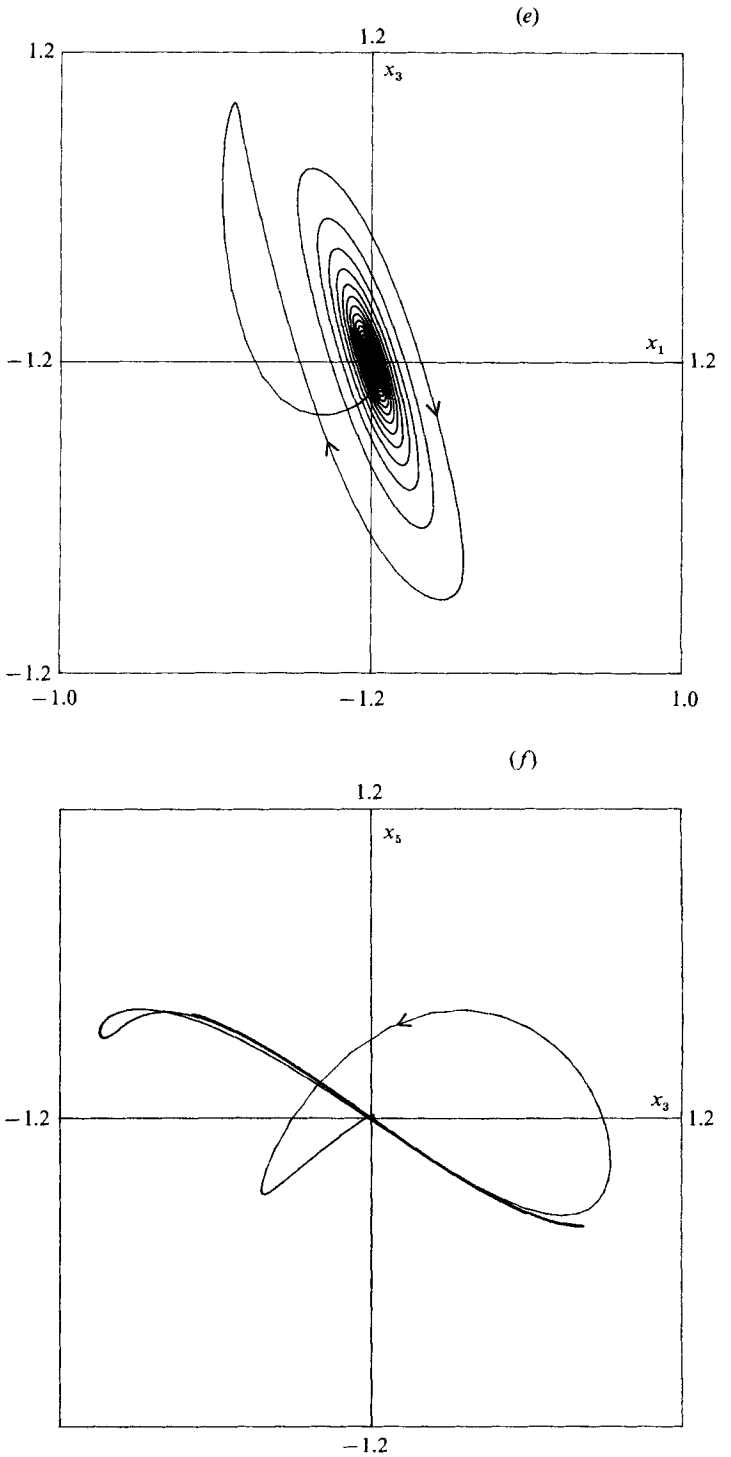

FIGURE 9. Time histories and selected projections of phase planes: (*a*) Heisenberg parameter $\alpha = 1.4$; (*b*) $\alpha = 1.5$; (*c, d, e, f*) $\alpha = 1.6$. Figure (*d*) shows a projection on the (x_2, x_4)-plane of a pair of burst events, showing how the solution passes from the neighbourhood of $\boldsymbol{r}^+$ to $\boldsymbol{r}^-$ and returns to $\boldsymbol{r}^+$ (see text). Figures (*e, f*) show projections onto the (x_1, x_3)- and (x_3, x_5)-planes and illustrate the growing linear instability near $\boldsymbol{r}^+$ in the $\{x_1, x_3, x_5\}$ subspace.

Coullet & Arneodo 1980; Silnikov 1965, 1968, 1970; Tresser 1984; Sparrow 1982; Guckenheimer & Holmes 1983, §6.5).

While evidence of intermittency has been detected before in fluid systems and models (Pomeau & Manneville 1980; Bergé *et al.* 1980; Maurer & Libchaber 1980; Dubois, Rubio & Bergé 1983) there has been little evidence of type II, associated with a subcritical Hopf bifurcation, which is what we observe in the present model at $\alpha = 1.61$. We shall therefore explore the connection between this dynamical phenomenon and its analogue in the turbulent boundary layer in some detail. For reasons we shall describe, our model displays a 'regular' intermittency, in contrast to the chaotic intermittency of Pomeau & Manneville (1980), in which event durations are distributed randomly.

We first describe the characteristic sequence of events observed in numerical simulations, starting immediately after a 'burst'. The solution remains near the fixed point $r_2, r_4 \neq 0$, $r_1 = r_3 = r_5 = 0$ for a relatively long period, during which the r_1, r_3, r_5 components grow exponentially in an oscillatory fashion. They eventually reach a critical amplitude at which r_2 and r_4 begin to oscillate perceptibly about their equilibrium values; these oscillations grow rapidly and then, with the phase difference $\phi_5 = 2\theta_2 - \theta_4$ remaining constant at π, θ_2 changes by π and θ_4 by 2π, r_2 and r_4 return to their equilibrium positions and r_1, r_3, r_5 simultaneously collapse to zero. The process is then repeated. Figure 9 shows typical time histories of the 10 components x_j, y_j for $\alpha = 1.35$, 1.5 and 1.6, as well as some (projected) phase-plane pictures. For these computations, initial conditions were chosen so that the fixed points that are successively visited lie in the purely real subspace, ($\theta_2 = 0, \pi$; $\theta_4 = \pi$), to correspond with our linearization work of §9.5. Hereafter we refer to the points as $\boldsymbol{r}^+(x_2 = +\imath_2, x_4 = -\imath_4, x_1 = x_3 = x_5 = y_j = 0)$ and $\boldsymbol{r}^-(x_2 = -\imath_2, x_4 = -\imath_4, x_1 = x_3 = x_5 = y_j = 0)$.

As α decreases from $\alpha_b \sim 1.61$, the typical duration of the laminar and burst phases is reduced until, at $\alpha \sim 1.3$, the growth is so rapid that no perceptible laminar phase remains. In fact, as we point out below, it is difficult to define 'typical' durations, since, as $t \to \infty$, the durations grow without bound, at least for α near α_b.

In the light of the invariant subspaces and the linear analysis of §9, the laminar growth phase is easy to understand. The fixed point $\boldsymbol{r}^+$ is a saddle point with a two-dimensional unstable manifold $W^u(\boldsymbol{r}^+)$ lying in the three-dimensional subspace spanned by x_1, x_3 and x_5. Thus, almost all solutions starting near $\boldsymbol{r}^+$ will exhibit an oscillation which initially grows exponentially at the rate of the (positive) real part λ^+ of the eigenvalues of $\boldsymbol{r}^+$. Since $\lambda^+ \to 0^+$ as $\alpha \to \alpha_b \sim 1.61$ (and $\lambda < 0$ for $\alpha > \alpha_b$), this rate decreases as α approaches the bifurcation value α_b (cf. table 1). The behaviour near $\boldsymbol{r}^-$ is similar, except that $W^u(\boldsymbol{r}^-)$ lies in the subspace spanned by y_1, y_3 and y_5 and thus exponentially growing oscillations are observed in that subspace. See the phase planes of figure 9 for clear geometrical evidence of the unstable manifolds $W^u(\boldsymbol{r}^\pm)$.

It is more difficult to see why the slow growth should culminate in the relatively sudden burst, in which x_2 changes sign (from $+\imath_2$ to $-\imath_2$), x_4 changes sign and returns to $-\imath_4$, and r_1, r_3 and r_5 collapse. However, if we postulate the existence of a *heteroclinic orbit* $\Gamma_1 = W^u(\boldsymbol{r}^+) \cap W^s(\boldsymbol{r}^-)$ connecting $\boldsymbol{r}^+$ to $\boldsymbol{r}^-$ in x_j space ($y_j = 0$, $\forall j$) and a (symmetric) orbit $\Gamma_2 = W^u(\boldsymbol{r}^-) \cap W^s(\boldsymbol{r}^+)$ connecting $\boldsymbol{r}^-$ to $\boldsymbol{r}^+$ in $(y_1, x_2, y_3, x_4, y_5)$-space ($x_1 = y_2 = x_3 = y_4 = x_5 = 0$), then this behaviour also becomes clear. We are observing orbits that are attracted to and remain in tubular neighbourhood of the (double) homoclinic cycle $\Gamma = \Gamma_1 \cup \Gamma_2$. Moreover, the computations summarized in table 1 shows that, for $\alpha > 1.37$, the smallest magnitude of the negative real parts of the eigenvalues of $\boldsymbol{r}^+$ and $\boldsymbol{r}^-$ is larger than that of the eigenvalues having positive real

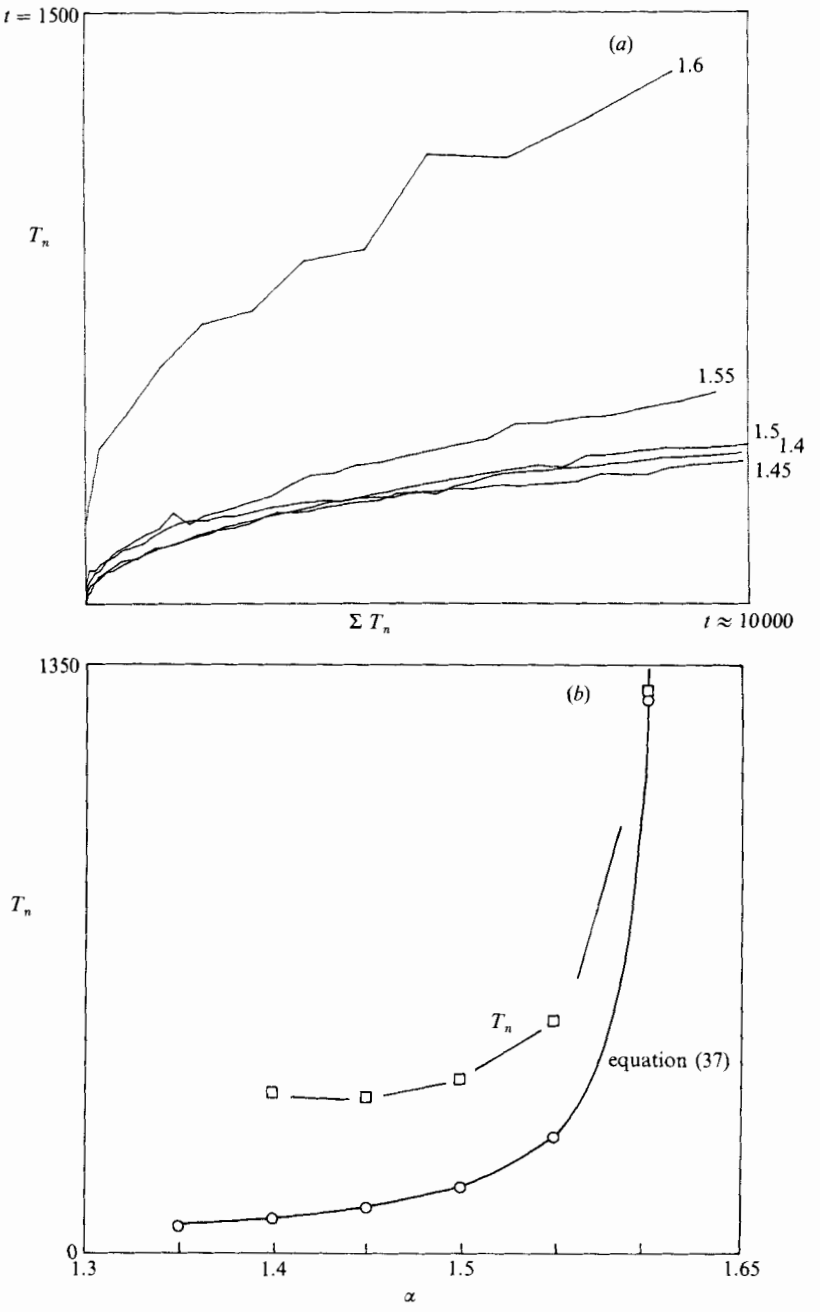

FIGURE 10. Graphs of durations of double burst events. (*a*) T_n *vs.* ΣT_n for $\alpha = 1.30$–1.60. (*b*) T_n at $t = 10^4$ *vs.* α. On (*b*) we also indicate the curve obtained from (37).

parts. Under these conditions, elementary linear analyses (cf. Guckenheimer & Holmes 1983, §§6.1, 6.5, and see below) show that Γ is an *attracting* homoclinic cycle, and thus we expect to see orbits that enter a sufficiently small neighbourhood of Γ approach it as $t \to +\infty$. Indeed, suppose that we have a (single or multiple) homoclinic orbit to a saddle point $\boldsymbol{p}$ having a pair of complex conjugate or a single eigenvalue with negative real part $-\lambda^-$. Suppose that $\lambda^- > \lambda^+ (> 0)$ and all other

eigenvalues have negative real parts greater in magnitude than λ^-. Consider an orbit entering a (fixed) ϵ-neighbourhood U_ϵ of $\boldsymbol{p}$ at distance d_0 from the stable manifold $W^s(\boldsymbol{p})$ and leaving at a distance d_1 from the unstable manifold $W^u(\boldsymbol{p})$. In U_ϵ the linearized flow dominates the behaviour, and thus typical solutions decay in norm at the exponential rate $e^{\lambda^- t}$ in the stable directions and growth at rate $e^{\lambda^+ t}$ in the unstable directions. Ignoring the rapidly decaying eigenvalues, simple integration of the linearized amplitude equations associated with the unstable and weakly stable directions shows that the time of flight of the solution passing through U_ϵ is given, to leading order, by

$$\tau_0 = (1/\lambda^+) \ln (\epsilon/d_0), \tag{33}$$

and that the relationship between d_1 and d_0 is

$$d_1 = \epsilon^{(1-\lambda^-/\lambda^+)} d_0^{\lambda^-/\lambda^+}. \tag{34}$$

Thus, as $d_0 \to 0$, we have

$$\tau_0 \sim (1/\lambda^+) \ln (1/d_0), \quad \ln (1/d_1) \sim (\lambda^-/\lambda^+) \ln (1/d_0). \tag{35}$$

These asymptotic results can be made rigorous regardless of the number of additional, strongly stable modes. Moreover, since the time taken by solutions to return to $\boldsymbol{p}$ (or to pass to the next saddle on the homoclinic cycle) is uniformly bounded *independent* of the distances d_0, d_1, we can estimate the global asymptotic behaviour of orbits in the tubular neighbourhood of Γ; in particular, this uniform bound implies that, if d_1 is the distance from the unstable manifold $W^u(\boldsymbol{p})$ on leaving $U_\epsilon(\boldsymbol{p})$ then the distance from the stable manifold $W^s(\boldsymbol{p})$ on next arrival at $U_\epsilon(\boldsymbol{p})$ is Kd_1, where K is a constant. Thus, for d_0, d_1 sufficiently small, the linear estimates (35) hold for the *global* behaviour at each passage around the cycle Γ. We conclude that, for $\lambda^-/\lambda^+ > 1$, we have an attracting homoclinic cycle, as claimed. (In our case Γ contains two identical saddles, and the compounded contraction factor is thus $(\lambda^-/\lambda^+)^2$ at each passage.)

This type of analysis permits one to predict the asymptotic rate at which event durations should grow for specific parameter values, once λ^- and λ^+ are known. Unfortunately the computations involved in numerical simulations are very delicate and even in double precision arithmetic, rounding error effectively prevents orbits from approaching the homoclinic cycle closer than some fixed distance ($\sim 10^{-16}$ for the double precision arithmetic used in this case). Thus, while the expressions (35), compounded for the double cycle, predict that the duration of laminar growth phases increases according to $T_{n+1} = (\lambda^-/\lambda^+)^2 T_n$, only modest increases of the form $T_{n+1} = T_n + \text{const}$ are observed. In figure 10 we plot event duration T_n versus time elapsed ΣT_n for various α-values. We also show the durations at elapsed time $t \sim 10^4$ as a function of α, compared with the time taken for a disturbance of $O(10^{-16})$ to grow to $O(1)$ (at which an event occurs) at the exponentially rate $e^{\lambda t}$:

$$\tau_0 \sim (1/\lambda^+) \ln (1/10^{-16}) \sim 38.84/\lambda^+. \tag{36}$$

Note that the order of magnitude appears to be correct. Note also that at $\alpha = 1.35$, for which the homoclinic cycle is no longer an attractor, the duration equilibrates at the (relatively) low value of 147.

Although our analysis does not adequately describe the rate at which event durations increase in the numerical simulation, the existence of an attracting homoclinic cycle does explain why the intermittent behaviour of the problem

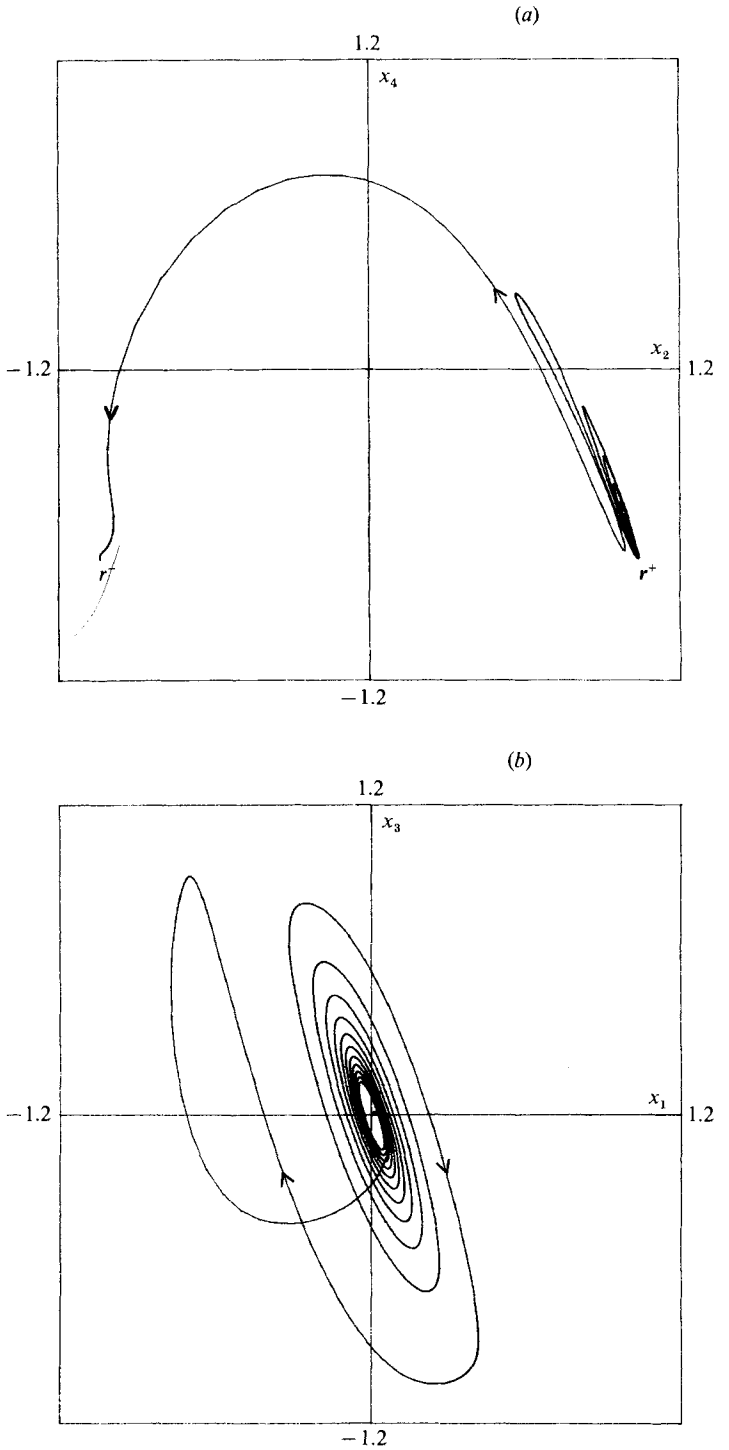

FIGURE 11. Projections on to the (x_2, x_4)- and (x_1, x_3)-plane of solution in the real subspace $\{y_j = 0\}$ illustrating heteroclinic orbit $\Gamma_+ = W^u(\boldsymbol{r}^+) \cap W^s(\boldsymbol{r}^-)$ which lies in $\{y_j = 0\}$. Heisenberg parameter $\alpha = 1.6$. Compare with figure 9 (d, e).

exhibits a steady increase in duration, rather than the randomly distributed behaviour of chaotic systems. For $1.37 < \alpha < 1.61$, Γ is a simple attracting set: *our system does not possess a strange attractor*. Nonetheless, the intermittent behaviour does capture the major features of the lift, sweep and ejection events observed in the boundary layer, as we shall see in the next sections. The addition of very small-amplitude random perturbations (due to the pressure terms which we ignored in §§7 and 8, cf. §5) would cause fluctuations in event durations which might be more appropriate to the true dynamical behaviour, Busse & Heikes (1980); Busse (1981). We return to this point in §11.

It remains, of course, to demonstrate the existence of the homoclinic cycle. Without loss of generality consider the component $\Gamma_1 = W^u(\boldsymbol{r}^+) \cap W^s(\boldsymbol{r}^-)$ which lies in the 'real' subspace $y_j = 0$. Restricting the flow to this subspace, Γ_1 connects the saddle $\boldsymbol{r}^+$, with three-dimensional stable manifold and two-dimensional unstable manifold $W^u(\boldsymbol{r}^+)$, to the *sink* $\boldsymbol{r}^-$, with its five-dimensional invariant stable manifold $W^s(\boldsymbol{r}^-) \cap \{y_j = 0\}$. (Recall that, for $\alpha > 1.45$ the unstable and zero eigenvectors of $\boldsymbol{r}^-$ lie in the imaginary ($x_j = 0$) subspace, §9.5.) Especially since $W^u(\boldsymbol{r}^+)$ is confined to a compact subset, in view of the global stability result of §9.1, it is not surprising that this two-dimensional manifold should intersect the five-dimensional manifold $W^s(\boldsymbol{r}^-) \cap \{y_j = 0\}$. Estimates of the 'real' vector field of (30) suggest that such a connection does exist (certainly, for $x_4 > 0$ sufficiently large and $x_1 x_3 < 0$, $x_3 x_5 < 0$, solutions pass from $x_2 > 0$ to $x_2 < 0$), but we have not yet proved the existence of the connection. Specifically, we must rule out the existence of any invariant set 'between' $\boldsymbol{r}^+$ and $\boldsymbol{r}^-$ to which $W^u(\boldsymbol{r}^+)$ might be asymptotic. This has been done in lower dimensions (Armbruster *et al.* 1988), but the details remain to be worked out in the present case. However, the numerical evidence is unequivocal. Solutions started in the real subspace with $(x_1^2 + x_3^2 + x_5^2)^{\frac{1}{2}}$ very small and $(x_2, x_4) = (+\epsilon_2, -\epsilon_4)$ leave the neighbourhood of $\boldsymbol{r}^+$ and, after a period of slow oscillatory growth, cross $x_2 = 0$ and rapidly approach $\boldsymbol{r}^-$: $(x_2, x_4) = (-\epsilon_2, -\epsilon_4)$. See figure 11, and compare with figure 9(*d*, *e*), above.

The behaviour of the eigenvalues of the (circle of) fixed points $\boldsymbol{r}^+$ also helps us see why 'clean' intermittent behaviour is not observed for $\alpha < 1.35$. At $\alpha \sim 1.37$ the weakest stable eigenvalue and the pair of unstable eigenvalues have real parts that are equal in magnitude, and for $1.32 < \alpha < 1.37$ the expanding real parts λ^+ are greater in magnitude than the smallest decaying real part λ^-. Under the latter conditions almost all orbits starting near the homoclinic cycle Γ are repelled from it: equations (35)–(36) show that $d_1 > d_0$ for d_0 sufficiently small and $\lambda^-/\lambda^+ < 1$. Thus almost all orbits must approach some other attracting set. Moreover, the analysis of Silnikov (1965, 1968, 1970) (cf. Guckenheimer & Holmes 1983, §6.5) shows that horseshoes (Smale 1967) and chaotic motions exist in the neighbourhood of Γ in this situation. While we cannot prove the existence of a strange attractor, in this light the numerical observation of complex, apparently chaotic motion in the Heisenberg parameter range $\alpha < 1.35$ is not surprising. However, at $\alpha \sim 1.32$ the non-zero (real) eigenvalue of $\boldsymbol{r}^+$ whose eigenvector lies in (y_2, y_4)-space becomes positive and so there is a further qualitative change in the phase space: $W^u(\boldsymbol{r}^\pm)$ becomes three-dimensional. Shortly afterwards, at $\alpha \sim 1.29$, a fourth eigenvalue, whose eigenvector lies in (y_1, y_3, y_5)-space for $\boldsymbol{r}^+$ and (x_1, x_3, x_5)-space for $\boldsymbol{r}^-$ becomes positive and $W^u(\boldsymbol{r}^\pm)$ becomes four-dimensional. Figure 12 shows time histories for $\alpha \sim 1.3$ which indicate these (strong) linear instabilities but also suggest that the fixed points $\boldsymbol{r}^\pm$ and the (r_2, r_4)-subspace play an important role even in this regime. One can even see

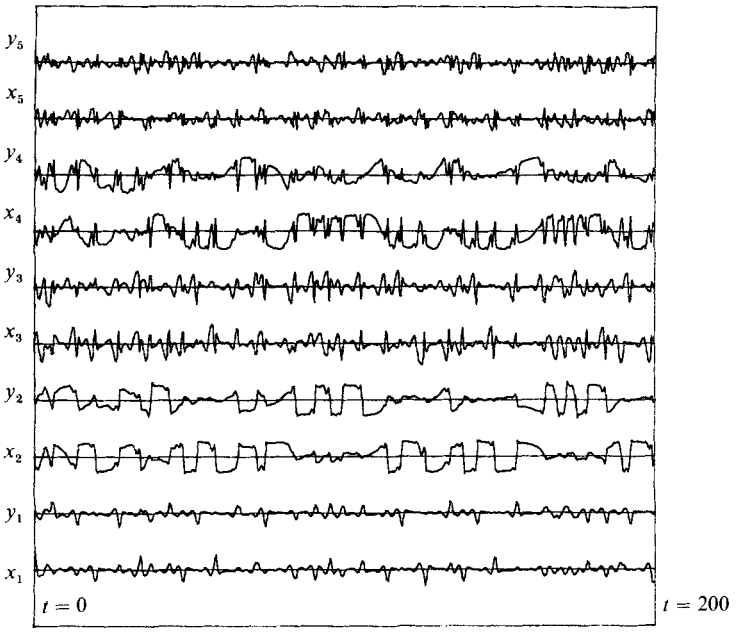

FIGURE 12. Time histories for Heisenberg parameter $\alpha = 1.3$, showing apparently chaotic motions.

instances of phase drift and travelling waves associated with the 2–4 fixed points with $\phi_5 \neq 0, \pi$ which bifurcate from $\boldsymbol{r}^{\pm}$ at $\alpha \sim 1.32$ (§9.4).

Throughout this discussion we have not explicitly mentioned the S^1 symmetry which implies that the fixed points $\boldsymbol{r}^+, \boldsymbol{r}^-$ are antipodal points on a *circle* of fixed points lying in the four-dimensional 2–4 subspace. Each such pair of antipodal fixed points are connected by a homoclinic cycle which is an image of Γ under an appropriate phase rotation. We anticipate that the use of group-theoretic methods will yield a much more complete picture of the model's behaviour.

10.3. *Summary*

After this lengthy discussion, a summary may be useful. For $\alpha > 1.61$ a unique circle of globally attracting stable fixed points exists in the 2–4 subspace (with a window of instability between 2.0 and 2.3): the r_1, r_3, r_5 components, along with the trivial r_0 component, are zero. As α increases, the magnitude of the r_2 and r_4 components decreases until, at $\alpha \sim 2.409$, this non-trivial circle of fixed points coalesces with the origin, which for $\alpha > 2.409$ is the unique and globally attracting fixed point for the problem. For $1.37 < \alpha < 1.61$, an S^1-symmetric family of globally attracting double homoclinic cycles Γ exists, connecting pairs of saddle points which are π out of phase with respect to their second (x_2, y_2)-components. The points $\boldsymbol{r}^+, \boldsymbol{r}^-$ discussed above are typical members of this family. The existence of the cycles Γ implies that, after a relatively brief and possibly chaotic transient, almost all solutions enter a tubular neighbourhood of Γ and thereafter follow it more and more closely. As they approach Γ, the duration of the 'laminar' phase of behaviour (in which r_2 and r_4 remain non-zero and almost constant and r_1, r_3, r_5 grow exponentially in an oscillatory fashion) increases while the bursts (in which r_1, r_3 and r_5 collapse) remain short. In an ideal, unperturbed system, the laminar duration would grow without bound, but small numerical perturbations, such as truncation errors, presumably prevent this

occurring in our numerical simulations. More significantly, the pressure perturbation, considered in §11, will limit the growth of the laminar periods. Thus there is an effective maximum duration of events, which is reduced as α is decreased from the critical value $\alpha_b \sim 1.61$.

As this paper was being completed we learned of work in progress on the 'Kolmogorov–Sivashinsky' equation: a scalar field model for two-dimensional turbulence (Nicolaenko 1986). Remarkably similar bifurcation sequences are observed and symmetries and homoclinic cycles play roles in that problem very like their roles in the present model. Related observations of solutions of the Kuromoto–Sivashinsky equation have been published (Hyman & Nicolaenko 1985; Hyman, Nicolaenko & Zaleski 1986).

In the next section we discuss the physical implications of this intermittent behaviour.

11. The pressure term: interaction with the outer layer

Thus far our model has been essentially insulated from the flow in the outer part of the boundary layer ($y^+ > 40$). We have assumed a fixed (time-independent) boundary at $y^+ = 40$, albeit with unusual boundary conditions, since the eigenfunctions Φ^n do not vanish there. We now attempt to introduce a more realistic boundary by including a term representative of the pressure field in the boundary layer at $y^+ = 40$.

Since spatially distributed experimental pressure measurements away from the wall itself are effectively impossible, we shall use data obtained numerically, specifically from the large-eddy simulations of Moin (1984). Moin's data is for a channel flow at $Re = 13800$ based on the centreline velocity and the channel half-width and yields a pressure spectrum $S(k_1, k_3, t)$ in terms of spanwise and streamwise Fourier wavenumbers and time at $y^+ = 38$. By projecting onto the appropriate Fourier modes ($k_1 = 0$, $k_3 = jk$, $j = 0, \ldots, 5$), we calculated the real and imaginary parts of the pressure excitation term which act as an external forcing function for the model equations of §8. Figure 13(*a*) shows the resulting functions over a time interval of 768 units (the extent of Moin's calculation). We note that the maximum amplitude of these functions is two orders of magnitude smaller than the maximum amplitudes of the variables x_i, y_i in solutions of the unperturbed equations. They can thus be expected to have little effect on the dynamical behaviour during a heteroclinic event, or burst, since the dynamical vector field is $O(1)$ in that regime. However, the noise has an important effect on the behaviour near the saddle points, where small perturbations typically cause solutions to leave the saddle region quickly, since they prevent close approaches to the stable manifold.

As we pointed out in §10, when an attracting heteroclinic cycle exists ($\lambda^- > \lambda^+$), the time duration between bursts, T_n, grows without bound according to the equation $T_{n+1} = (\lambda^-/\lambda^+)^2 T_n$, although in numerical simulations the durations are limited by finite precision arithmetic (cf. (37), figure 10). Addition of the relatively weak pressure signal limits these durations in a much more dramatic manner, as figures 13(*b–e*) shows. Here we compare solutions of the model equations (24) with and without the pressure term for two values of the parameter α. The results indicate that, as expected, the solution during the burst phase is little affected by the presence of the small pressure term, but that this term causes the interburst duration to equilibrate rapidly.

A simple theory for local behaviour near the saddle, in which the pressure term is

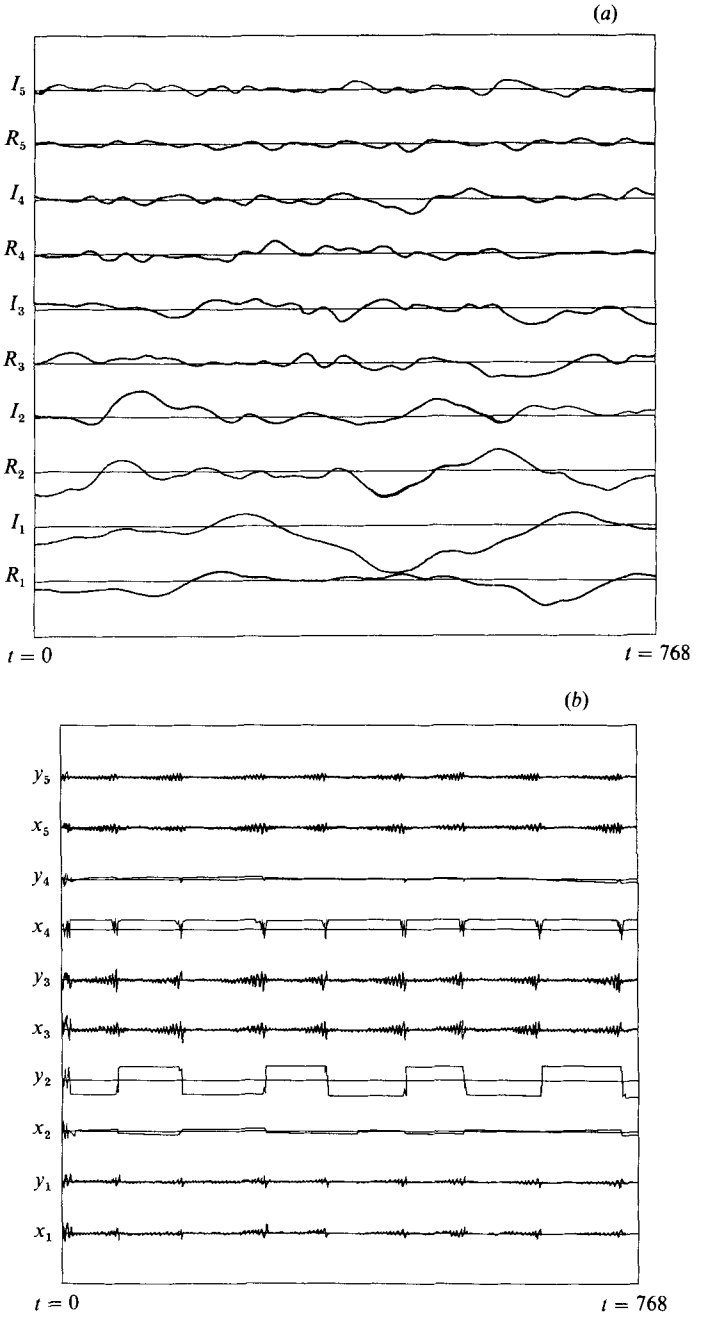

FIGURE 13(*a*, *b*). For caption see page 156.

modelled as an impulsive random perturbation at each approach to the saddle, permits one to predict a distribution of 'residence times' for solutions near the saddle points; in particular, the mean interburst period is found to scale with noise amplitude ϵ and unstable eigenvalue λ^+ as

$$T \sim K_1 + \frac{1}{\lambda^+}\left[K_2 + \ln\left(\frac{1}{\epsilon}\right)\right]. \tag{37}$$

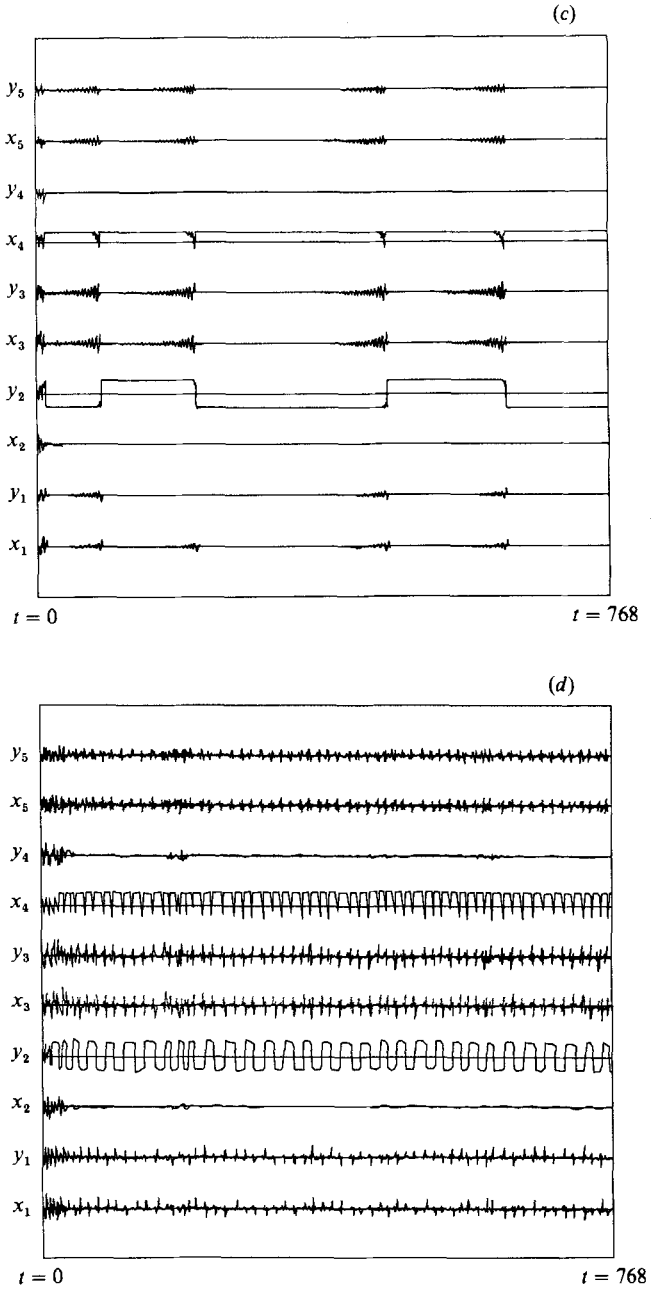

FIGURE 13(*c*, *d*). For caption see page 156.

Details of this and more sophisticated analyses will be published later (P. Holmes & E. Stone paper in preparation). The limited durations of pressure signals available to us preclude the reliable computation of mean and variance of interburst durations, but the results summarized on figure 14 indicate that (38) is a reasonable predictor of mean interburst durations. The constants K_i were determined from a least squares fit of the data (T *vs.* $1/\lambda^+$) for a single value of ϵ.

The main point of interest for the present study is that the pressure term provides

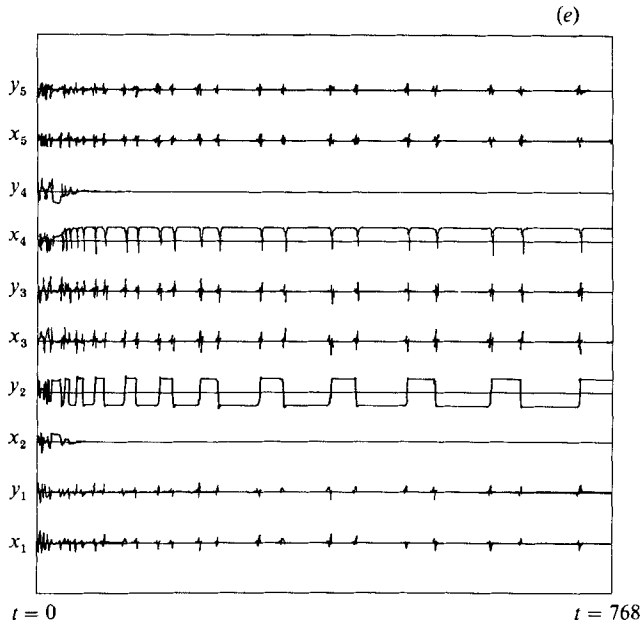

FIGURE 13. Pressure perturbations: (*a*) pressure excitations for the ten model equations (scale, 100 × figures 7–9); (*b*, *c*) solutions for $\alpha = 1.6$ (*b*) with and (*c*) without pressure term; (*d*, *e*) solutions for $\alpha = 1.4$, (*d*) with and (*e*) without pressure term.

a means of coupling the inherent wall-layer dynamics (heteroclinic bursts) with the behaviour of the outer layer, which, via the weak quasi-random pressure excitation, acts as a trigger, promoting bursting behaviour at a steady rate. Thus, while the source and gross characteristics of individual bursts are a feature of the deterministic model equations (and thus of the inner 'insulated' wall region), their quasi-regular repetition is due to the influence of pressure fluctuations arising in the outer layer.

This resolves in a satisfactory way the controversy that has long existed relative to normal and drag reducing boundary layers: whether the events related to bursting scale with outer variables or wall variables. We feel it is now clear that the bursts themselves should scale with wall variables, while the interburst period should scale with both outer and inner variables. In this connection note that, in (37), the unstable eigenvalue λ^+ is a property of the wall layer (inner) model, while the pressure amplitude ϵ is a property of the outer layer.

12. Implications for the flow in the wall region

Equipped with the information about fixed point, intermittent and chaotic solutions of the model ODEs discussed above, we can now reconstruct the steady and time varying three-dimensional perturbation velocity fields in the wall region. We start with a geometrical description of the resulting fluid flow, and follow this with discussions of the Reynolds stress change exhibited during the quasi-steady and bursting phases of the flow corresponding to the intermittent dynamical behaviour.

FIGURE 15(*a*).

FIGURE 15. Coloured pathlines for initial conditions $x_2 = 13$ and various x_3 (simulation of a spanwise marker). x_2-axis is stretched, x_1-axis is shrunk.

FIGURE 15(*c*).

FIGURE 16. Coloured pathlines with same initial conditions as in figure 15 obtained with the perturbation velocity field $\boldsymbol{u}$ only.

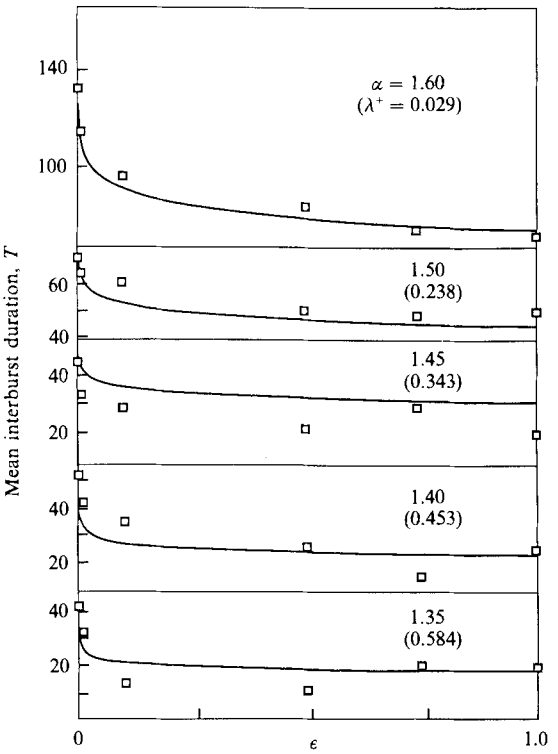

FIGURE 14. Mean interburst duration T as a function of eigenvalue λ^+ and pressure signal amplitude ϵ. Solid curves indicate prediction of (38), open squares indicate results of numerical simulations.

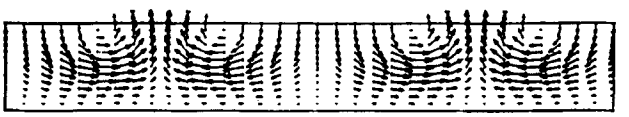

FIGURE 17. Vector representation of the (x_2, x_3)-components of the velocity field in a cross-section (x_2, x_3-plane) of the periodic cell: $L_3 = 333$, $x_2^+ = 40$ (in inner variables) reconstructed from the stable point obtained for Heisenberg parameter $\alpha = 2.0$.

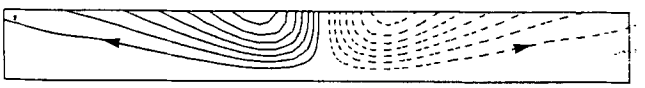

FIGURE 18. Streamlines in the (x_2, x_3)-plane of the first eigenfunction. $x_2^+ = 65$ corresponds to the top of the figure (from Moin 1984).

12.1. *Flow geometry, velocity fields and streaklines*

Reconstruction of flow corresponding to fixed points is relatively simple, since in this situation the (complex) modal coefficients

$$a^{(n)}_{k_1=0,\, k_3=jk} = x_j + \mathrm{i}y_j$$

remain constant and one simply forms the constant velocity field with components

$$u_i(\boldsymbol{x}, t) = \sum_{j=1}^{3} a^{(n)}_{0,jk}\, \mathrm{e}^{2\pi \mathrm{i} jk x_3}\, \phi^{(1)}_{i\,0,jk}(x_2) \tag{38}$$

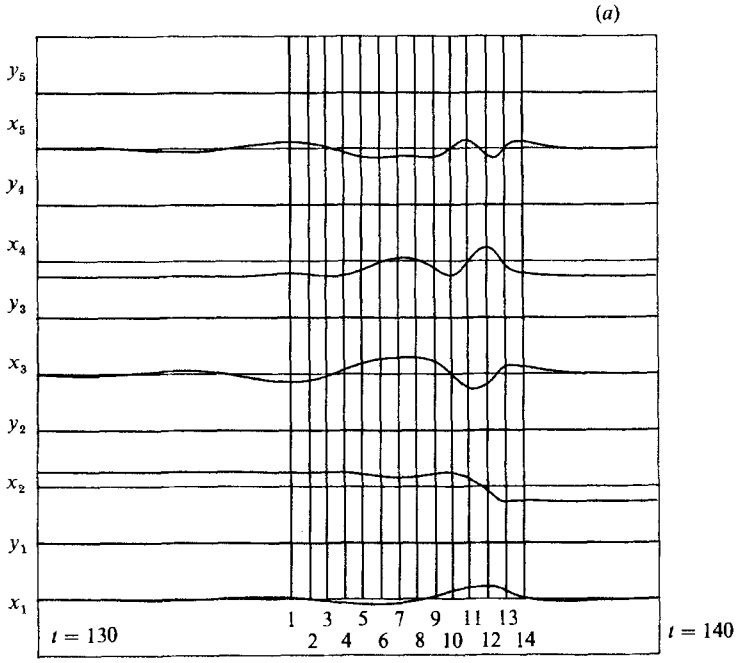

FIGURE 19. Intermittent solution corresponding to an Heisenberg parameter $\alpha = 1.4$. (*a*) Time history of the real and imaginary parts of the model coefficients x_i, y_i $(i = 1, 2, \ldots, 5)$ (*b*) Vector representation of u_2, u_3 in a (x_2, x_3)-plane at times indicated on (*a*).

(cf. the general form of (8)). Addition of the x_2-dependent mean velocity $(U(x_2), 0, 0)^{\mathrm{T}}$ yields the full velocity field $\boldsymbol{v}(\boldsymbol{x}, t)$. Note that $\boldsymbol{u}$ depends only on x_2 and x_3, since we have only included the zero Fourier mode in the streamwise (x_1) direction. Thus the velocity field is constant in time and identical at each streamwise station $x_1 = \text{const}$. Nonetheless, the interaction of the spanwise and wall-normal (perturbation) velocity components with the streamwise, predominantly mean, component $U(x_2) + u_1(\boldsymbol{x}, t)$ leads to non-trivial behaviour, even in the time-independent case.

To illustrate this, we have integrated the Lagrangian problem

$$\frac{\mathrm{d}x_i}{\mathrm{d}t} = v_i(\boldsymbol{x}, t) \tag{39}$$

to investigate the motion of fluid particles in the flow. This permits us to compare the behaviour of our model with the flow visualization experiment in which passive markers, such as bubbles or dye streaks, are released near the wall. In particular, we have integrated sets of initial conditions at $x_2^+ = 13$ for various x_3 to represent the transport of a 'pulse' of hydrogen bubbles released from a wire stretched horizontally in the spanwise direction above the boundary layer at constant x_2^+ (cf. Kline *et al.* 1967; figure 1). The evolution in time of the marker is thus followed and a three-dimensional picture of the pathlines is obtained at each timestep. Pictures of the last frames rotated at different angles are then taken: figures 15 and 16 (Plate 1). In order to visualize all directions adequately, we stretch the x_2-axis and shrink the x_1-axis. We also display the spanwise and wall-normal components of the velocity field in the (x_2, x_3)-plane in figure 17. Here, the magnitude and direction of the arrow indicates the velocity at its base point.

Figures 15, 16 and 17 show our results for the instantaneous velocity field

(*b*)

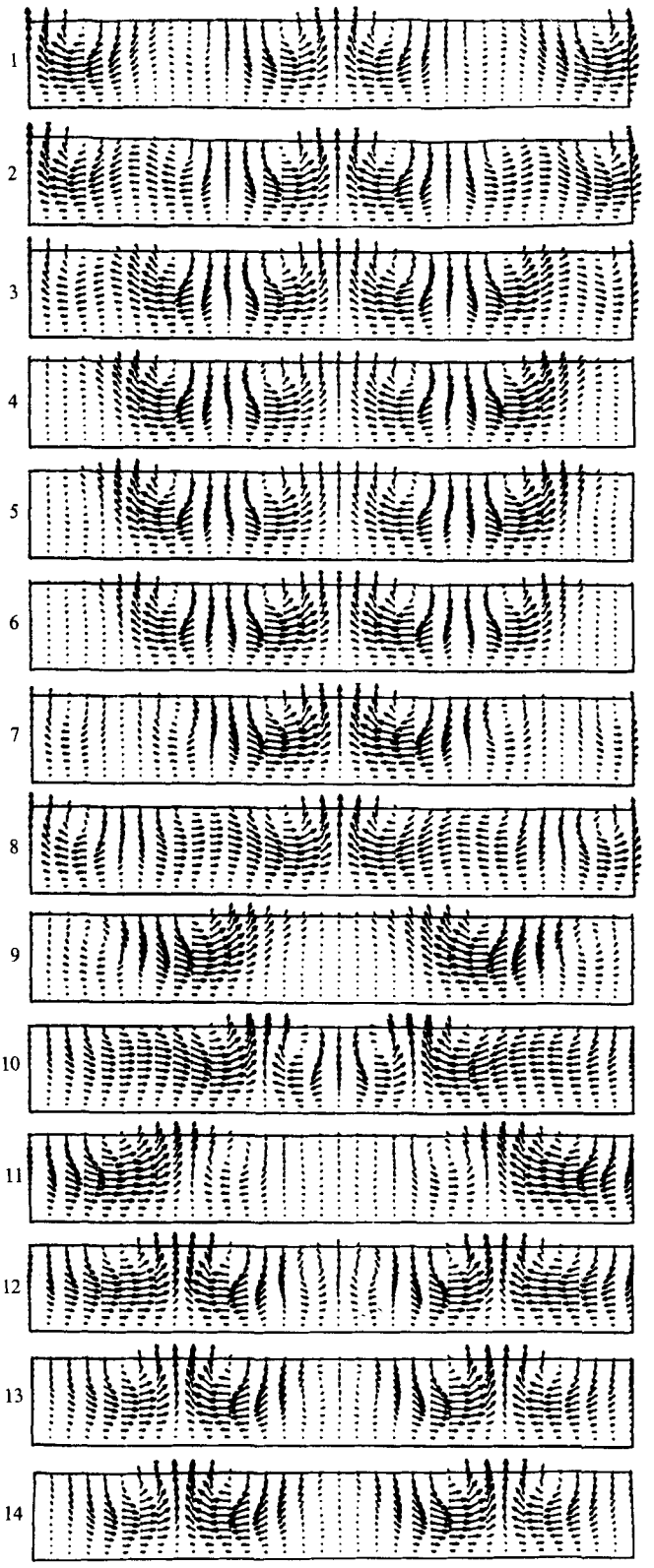

FIGURE 19(*b*). For caption see facing page.

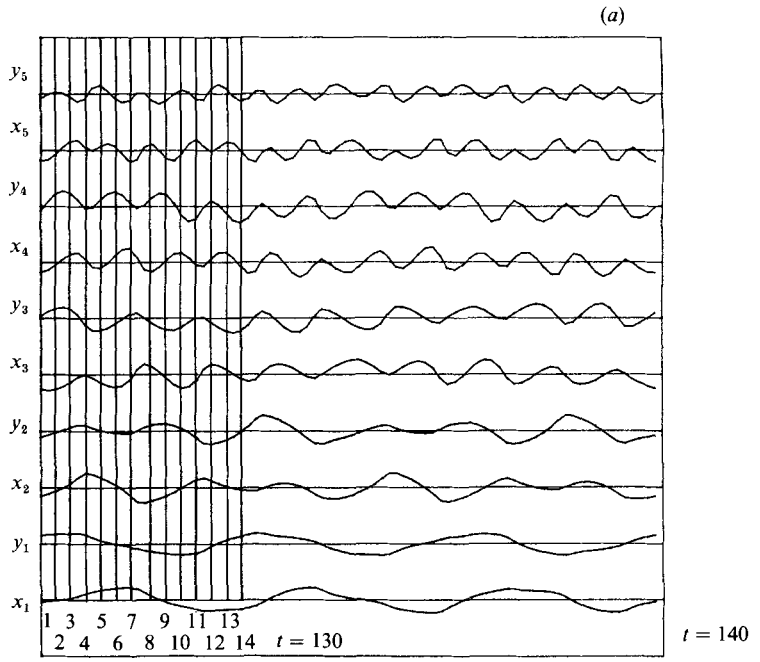

FIGURE 20. Chaotic solution for Heisenberg parameter $\alpha = 1, 2$. (*a*) Time history of the real and imaginary parts of the modal coefficients x_i, y_i $(i = 1, 2, \ldots, 5)$ (*b*) Vector representation of u_2, u_3 in a (x_2, x_3)-plane at times indicated on (*a*).

reconstructed from the stable fixed point $r_2 = -0.800$, $r_4 = -0.273$, $r_1 = r_3 = r_5 = 0$, $\phi_5 = 2\theta_2 - \theta_4 = \pi$ which exists for Heisenberg parameter $\alpha = 2.0$ (for other values $1.61 \leqslant \alpha \leqslant 2.41$ for which the system of equations also evolves to a fixed point, the resulting steady velocity field is similar). As predicted in §7, because a part of the energy contained in our truncated system is lacking, our reconstructed velocity components are too small in the spanwise and normal directions. Nevertheless we can clearly see two pairs of counter-rotating streamwise vortices in each periodic cell of length $L_3 = 333$ wall units. The rolls are symmetric with respect to an (x_1, x_2)-plane, which is a consequence of the act that the stable point lies in the real subspace. The rolls generate a strong updraught between them and a weak downdraught on their 'outsides'. This can be observed from the display of the (x_2, x_3)- velocity components in the cross-section of figure 17 and becomes even clearer by observation of the fluid which is violently ejected upward once it reaches the appropriate zone (between the two vortices) (figure 15*a*). The rolls of figure 17 can be compared to those obtained by Moin (1984) from large-eddy-simulation data, figure 18. Figures 15(*b*) and 15(*c*) can be compared to those obtained by Kline *et al.* (1967) by visualization with the hydrogen bubble technique (here, since the velocity field is time independent, pathlines and streaklines are identical). After a sufficiently long time, the particles are collected between the rolls into streamwise streaks which become thinner downstream. This is due to concentration of fluid in the (x_1, x_2) vertical 'ejection' plane in which the spanwise velocity is very small. All the particles are thus convected away from the wall as they go downstream. The streak spacing is approximately 150 wall units which is in reasonable agreement with the experimental result $\lambda^+ = 100 \pm 40\%$ given by Kline *et al.* (1967). Figure 16 shows the integration of (39) where the instantaneous velocity field $\boldsymbol{v}$ is replaced by the perturbation $\boldsymbol{u}$. It

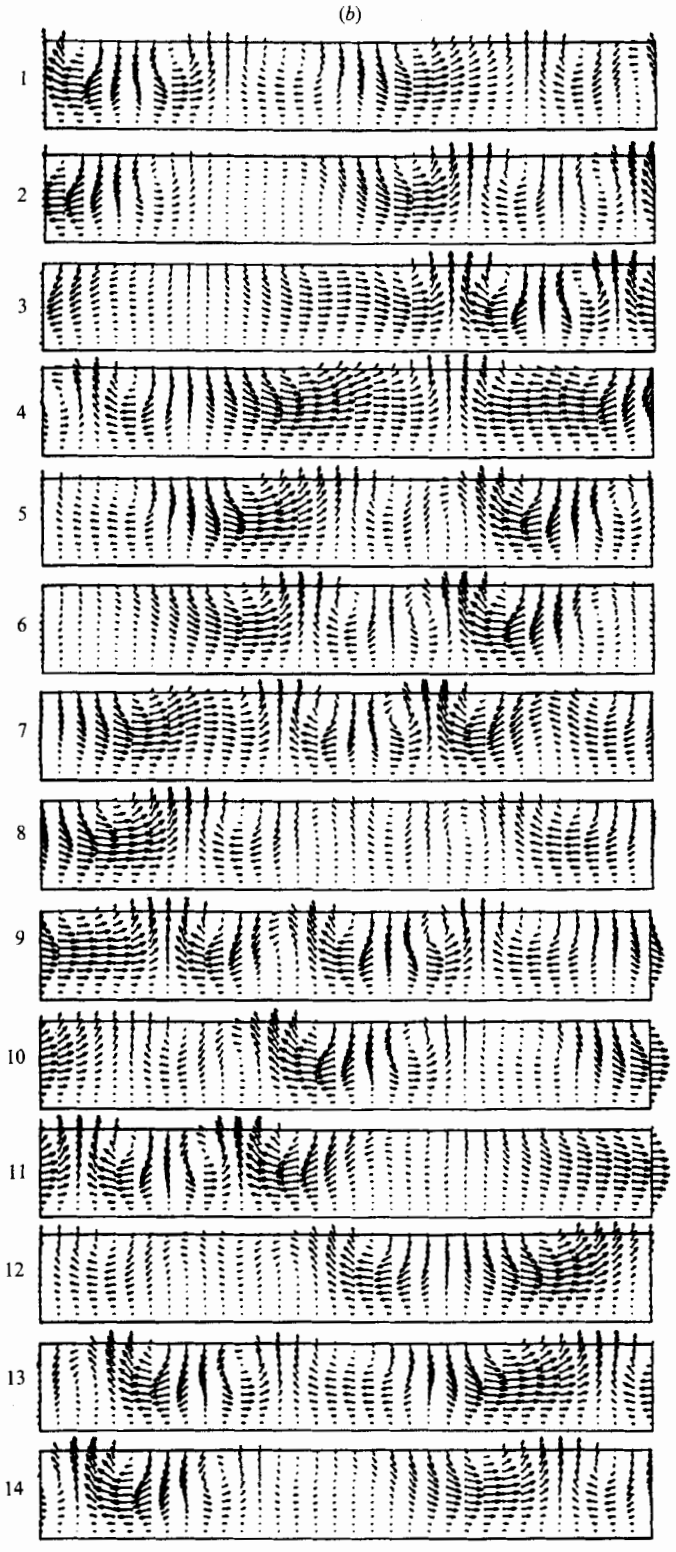

FIGURE 20(*b*). For caption see facing page.

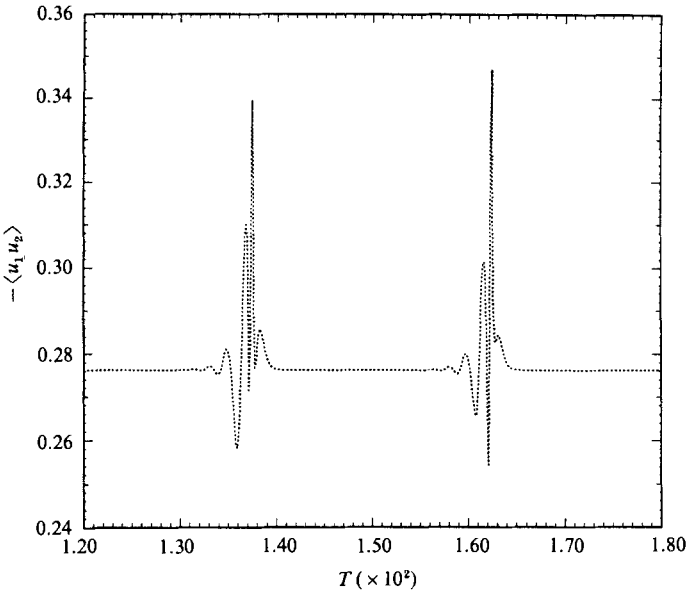

FIGURE 21. The Reynolds stress $\langle u_1, u_2 \rangle$ at $y^+ = 35$ *vs.* time for Heisenberg parameter $\alpha = 1.4$, showing two bursts.

reveals the presence of negative streamwise perturbation patterns which drift away to the top of the layer.

After this static geometrical description of the velocity field, we now interpret its dynamical behaviour for lower values of the Heisenberg parameter α. Time-dependent flows are reconstructed in precisely the same way, except that now the velocity $\boldsymbol{v}(\boldsymbol{x}, t)$ is time-dependent. The numerical values of x_j, y_j obtained by integration of the ODEs (24) are used in (38) to yield tables of time-dependent components u_i. Like the steady rolls, our time-dependent solution suffers the same deficiency in the velocity field, due to the truncation.

Probably the most interesting sets of solutions are those exhibiting intermittency, obtained for $1.3 \leqslant \alpha \leqslant 1.61$. The phenomenon has already been described in §10.2 from a dynamical-systems point of view. In the flow field, the rapid event which follows the slowly growing oscillation and the repetition of the process reminds one of the bursting events experimentally observed (Kline *et al.* 1967; Corino & Brodkey 1969, etc.). For that reason we call it a 'burst'. We shall analyse its effect on the streamwise vortices.

In figure 19(*a*) we show an enlargement of the time histories of the modal coefficients during a burst for $\alpha = 1.4$ (cf. figure 9*a*). A description of the motion of the eddies during the burst is given in figure 19(*b*) for $\alpha = 1.4$ by plotting u_2 and u_3 at the different times indicated on figure 19(*a*). Before and after the event, two pairs of streamwise vortices are present in the periodic box, a structure very similar to that previously obtained for $1.61 \leqslant \alpha \leqslant 2.41$. Nonetheless pictures 1 and 14 are shifted in the spanwise direction by $333_+/4$, corresponding to the phase shift $\Delta\theta_2 = \pi$, $\Delta\theta_4 = 2\pi$ (see §10.2). The bursting event leads to variations of positions and amplitudes of the basic streamwise rolls and formation of other vortices. The oscillation, death and rebirth of vortices make the streak spacing vary. This recalls the experimental results: 'considerable variation in the spacing between individual streaks' (Kline *et al.* 1967). However, since the intermittent solution is always very close to the real

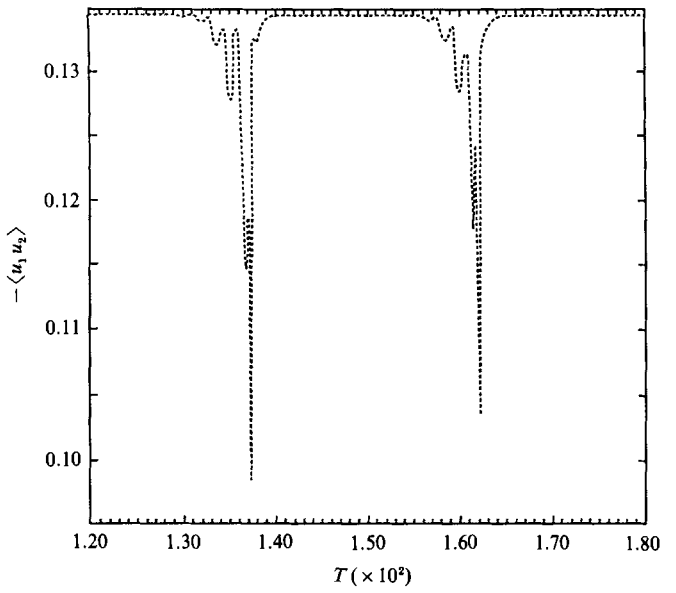

FIGURE 22. The Reynolds stress $\langle u_1 u_2 \rangle$ at $y^+ = 10$ *vs.* time for Heisenberg parameter $\alpha = 1.4$, showing two bursts.

subspace or a rotation of it, the vortices remain symmetric and paired. Moreover it is possible to adjust the value of the viscosity parameter ($\alpha \sim 1.5$) so that the bursting period is 100 wall units as experimentally observed. It is found that, in this case, the 'burst' lasts 10 wall units which is also the right order of magnitude.

The behaviour of the eddies corresponding to a chaotic solution ($1.0 \leqslant \alpha \leqslant 1.3$) is shown in figure 20(*b*), as before, by plotting the u_2, u_3 velocity components at specific times. The behaviour is less regular and isolated vortices sometimes emerge. This is consistent with the flow visualization experiments of Smith & Schwarz 1983 who observed a significant number of solitary vortices among the predominant vortex pairs. These patterns are also very rich in dynamics. We intend to study the regime further in future work.

12.2. *Reynolds stress behaviour during the 'burst'*

Plots of the evolution of the Reynolds stress $\langle u_1 u_2 \rangle$ in time, at different values of x_2 show a strong change during the burst. Nevertheless this change is negative in absolute value near the wall and only changes its sign at about $x_2^+ = 25$ for $\alpha = 1.4$. At this level and higher there is significant increase of the Reynolds stress but it is not as large as that observed in experiments, see figures 21 and 22. We discuss the reasons for the discrepancy in the final section.

13. Physical interpretation

Owing to the truncation of our model to a single eigenmode and one streamwise Fourier component, the absolute and relative energy of the various velocity components is affected. First, the choice of streamwise lengthscale affects absolute values of all the component energies, but not their relative values. We chose a streamwise lengthscale of 333. Keeping only the Fourier mode at zero streamwise wavenumber, this is equivalent to supposing that the distribution of the first

eigenvalue with wavenumber is flat to 333, and drops to zero. Comparison with the true distribution of the first eigenvalue with streamwise wavenumber indicates that this should overestimate the energy in this eigenvalue. A more reasonable lengthscale would be between 400 and 500, a value determined by the requirement that the area between it and the origin is the same as the true area under the distribution of the first eigenvalue with streamwise wavenumber. However, examination of the equations indicates that changing the value of L_1 leaves the equations invariant. Hence all phenomena reported here would be unchanged, with simply a decrease in energy level of all the velocity components. This would decrease the overestimated streamwise energy contained in our system but would not necessarily improve our model since it would also decrease the energy, already deficient, in the normal and cross-stream components.

The truncation also affects the relative energy in the various velocity components. We have examined the distribution with x_2^+ of the energy in the three velocity components for truncations of 3, 6 and 17 cross-stream wavenumbers, 1, 2 and 7 streamwise wavenumbers, and 1 and 3 eigenmodes. It is clear that the energy in the u_2 and u_3 components is relatively low (compared with the u_1 component) when only one streamwise wavenumber is included. This is particularly true in the upper part of the layer. While inclusion of more than 6 cross-stream wavenumbers has no effect, addition of streamwise wavenumbers does make a difference. In particular addition of another streamwise wavenumber helps considerably. We must conclude that there is energy in cross-stream and normal motions of higher streamwise wavenumbers that makes little relative contribution to the streamwise velocity component. As a consequence, our predicted rolls are somewhat weak compared with reality, and we rescaled them in figure 13 to give three-dimensional trajectory images more comparable with experiment. This rescaling will not be necessary in future work, when we shall add streamwise wavenumbers.

One naturally asks if the addition of streamwise modes will drastically change the behaviour of our model. In this respect, we observe that the same symmetries, inherited from invariance of the Navier–Stokes equations to spanwise translation and reflection, and streamwise translation, operate at any order of truncation. In particular, this implies that the subspace spanned by basis functions with zero streamwise wavenumber is invariant and that the coefficients of the equations restricted to this subspace remain unchanged as streamwise components are added. Thus, the model studied in this paper, together with its dynamics, exists *unchanged*, as a *subsystem* in the larger set of differential equations, much as the 2–4 subsystem exists in the present model. This raises the interesting possibility that the 2–4 branch may be destabilized by streamwise modes as well as by the 1, 3, 5 'interstitial' spanwise Fourier modes as described in §9.5. In such a case one might expect even more exotic bursting behaviour, while stability of the 2–4 spanwise, zero streamwise wavenumber subspace would imply that the present behaviour would be little changed beyond excitation of streamwise components during a burst. In an attempt to address this, we integrated a model with three streamwise and three spanwise components, of total dimension 24 (after removal of the (0, 0) mode). This model exhibited steady rolls down to $\alpha \approx 0.5$, indicating stability of the 2–4 subspace to non-zero streamwise perturbation. We have not yet tackled the 54-dimensional model with 3 streamwise and 6 spanwise modes, for the following reasons.

In the preliminary studies of models with two and three streamwise wavenumbers referred to above, it became clear that the way in which the eigenfunctions are fitted to the experimental data can affect the magnitude of the coefficients a, c and d of the

model equations by up to 20%. The dependence of the linear term on the second derivative is especially sensitive, and the sensitivity is apt to increase as streamwise wavenumbers are included. Before embarking on a detailed study of models with additional Fourier components and eigenfunctions, we therefore decided to investigate the effect of eigenfunction variations on the six-mode model studied in this paper. We obtained a set of eigenfunctions computed from direct numerical simulations of a channel flow at $Re = 6600$ through the courtesy of Parviz Moin and Robert Moser at the Stanford–Ames Center for Turbulence Research. While the flow conditions are somewhat different from those of Herzog's (1986) pipe flow, the eigenfunctions are generally similar in form, and they are defined more precisely, since the discretization is considerably finer. The resulting coefficients in the model equations have the same signs and general relative magnitudes as those of the present model, the largest differences being of the order of 20%. While this affects the detailed structure of the bifurcation diagram, the model still exhibits bursting behaviour, albeit now for a lower value of α (≈ 0.74) and involving heteroclinic cycles connecting small periodic orbits (limit cycles) which contain all Fourier components, not merely 2 and 4. Thus, in this model, the quasi-steady state is of weakly oscillating rolls which have a somewhat richer spanwise structure. The general features of the burst are very similar to the present model. For higher α one again observes steady rolls containing only Fourier components 2 and 4. We feel that these findings, which we shall report in detail later, give much credibility to our present simple model.

The model we have presented here is rudimentary in more ways than the simple sparsity of modes retained. Many non-essential mechanisms have been suppressed in the interests of simplicity. For example, the structure of the eigenmodes normal to the wall is held fixed as the modes evolve. In nature, the eddies in the wall layer are observed to be approximately round in cross-section. To mimic this behaviour we could allow the scale of the modes normal to the wall to grow and shrink; this could be done either by tying the scales to the slope of the mean velocity profile at the wall (so that the eddies always fill approximately the same fraction of the mean profile as the shape of that profile changes), or the scales could be made to change proportional to the centroid of the energy in the cross-stream modes. That is, if the energy were concentrated in $2k$ rather than k, the scale normal to the wall would be reduced. Either of these would produce a more realistic behaviour.

We do not have present in our modal population a mechanism to represent the production of higher-wavenumber energy when an intense updraught is formed, presumably as a result of a secondary instability. We quote, for example, the description of the measurements of Kim *et al.* (1968) from Willmarth & Lu (1972): 'When the rising filament of low-speed fluid reached a height in the range $8 < y^+ < 12$, an oscillatory motion of marked fluid lines (time lines) within the parcel was observed. The oscillatory motions, which were of various types, appeared to be associated with a swirling motion of the fluid. As the amplitude of the swirling motion of the rising fluid became larger, the pattern "broke up" at a distance from the wall in the range $10 < y^+ < 40$. During the breakup process, a significantly more random chaotic motion occurred in which marked lines of fluid were obliterated owing to the sudden increase in turbulent mixing'. Willmarth & Lu (1972) also quote Corino & Brodkey (1969): 'When the ejected low-speed fluid encountered the interface between high-and low-speed fluid, at the high shear layer, a violent interaction occurred with intense, abrupt and chaotic movements. The intense interaction continued as more fluid was ejected. The end result was the creation of a relatively large-scale region of turbulent motion reaching into the sublayer as the

violent interaction region spread out in all directions'. It is clear that the higher-wavenumber turbulence produced in this 'violent interaction region' has strong transport properties, since it transports both the marked lines, obliterating them, and itself, spreading the region of higher-wavenumber turbulence. To the extent that there are inequalities of momentum of larger scale in this region (and there are) it will transport them also. Thus, the higher-wavenumber component will make a substantial contribution to the Reynolds stress. Unfortunately, the various measurements (see particularly Lu & Willmarth 1973) do not appear to have discriminated between the high-wavenumber and low-wavenumber contributions to the Reynolds stress; they are not separated by conditioning (or, at least, not by the conditioning of Lu & Willmarth 1973) since they occur at more-or-less the same time. The only indication is given by the calculations of Corino & Brodkey (1969), who have calculated by hand the contributions to the Reynolds stress of the large-scale motions in the ejection phase, finding a value between 50% and 70% of the long-time average value, the percentage falling with Reynolds number. Since Lu & Willmarth (1973) and Willmarth & Lu (1972) measure values of the Reynolds stress during a burst several times the long-term average, a considerable fraction of the Reynolds stress must be produced by the higher-wavenumber component. The higher-wavenumber component will also be expected to make a contribution to the streamwise and cross-stream energy.

Thus, although our eddies are capable of exhibiting the basic bursting and ejection process, the labour is in vain – there is no sequel, no production of intense higher-wavenumber turbulence. A contribution is made only to the low-wavenumber part of the streamwise fluctuating velocity and the Reynolds stress. We could easily simulate the production of this high-wavenumber turbulence, although we do not expect its inclusion to change the dynamics of our system qualitatively. However, we have held the value of our Heisenberg parameter constant, whereas its value should rise and fall with the level of this intense higher-wavenumber turbulence in the vicinity of the wall. The transport effectiveness of intense higher-wavenumber turbulence would be expected to damp the system, suppressing the interesting dynamics until the higher levels are either blown downstream or lifted and diffused to the outer edge of the boundary layer. The production of higher values of the Heisenberg parameter could easily be parameterized by a single time-constant first-order equation tied to a measure of the amplitude of the coefficients. The major effect would simply be to cut off each burst more rapidly than at present. We plan to study the behaviour of a such a model in the future.

The absence of this component of the Reynolds stress has other effects. At present each bursting event produces a considerable change in the Reynolds stress, but the magnitude is too small and the direction is positive over too much of the layer, although it has the right sign in the outer part of the layer. The contribution of the higher-wavenumber Reynolds stress would change this situation, since the latter Reynolds stress would be negative and large, and would occur in the outer part of the wall region, near the tops of the large eddies.

In this connection we may mention the convergence of our representation of the velocity field. The set of eigenfunctions is complete, which means essentially that any physically possible velocity field can be represented. The eigenfunctions are computed from second-order statistics. It is, of course, quite possible (even likely) that there are dynamically significant events the contribution of which to the second-order statistics is lost in the experimental noise, but which would contribute

importantly to the fourth-order statistics, say. These events are thus not represented among the eigenfunctions we are able to compute from the experimental information at hand. However, the completeness of the set of eigenfunctions (including those undeterminable from the experiment) assures us that these events would be represented by the inclusion of the higher-order eigenfunctions, if we knew them. Put simply, although we may be neglecting something by our truncation, inclusion of higher wavenumbers in the streamwise and cross-stream directions, and of higher eigenmodes (we may, in fact, already have high enough wavenumbers in the cross-stream direction) would recapture this effect. There is nothing fundamentally limiting about the nature of our model that makes it incapable of capturing reality.

The occurrence of the bursts of values of the Heisenberg parameter between 1.4 and 1.6 appears to be pseudorandom. This is essentially due to round-off error in the calculations. The transitions from one solution to the other and back are extremely sensitive to the precise solution trajectory, and a minute change can make a considerable change in the time at which the next transition occurs. Initially we did not exercise the pressure term. Recall that the pressure term appeared owing to the finite domain of integration. It represents the interaction of the part of the eddy that we have resolved with the part above the domain of integration, which is unresolved. The order of magnitude that we estimated for this term was small, and for that reason we at first neglected it. It has, however, an important effect, while not changing the qualitative nature of the solution. The term has the form of a random function of time, with a small amplitude. This slightly perturbs the solution trajectory constantly; away from the points $\boldsymbol{r}^+$ and $\boldsymbol{r}^-$ this has little effect, but when the solution trajectory is very close to these points, the perturbation has the effect of throwing the solution away from the fixed point, so that it need not wait long to spiral outward. This results in a thorough randomization of the transition time from one solution to the other, while having little effect on the structure of the solution during a burst, as described in §11.

Probably the most significant finding of this work is the identification of the etiology of the bursting phenomenon. That is, the bursts appear to be produced autonomously by the wall region, but to be triggered by pressure signals from the outer layer. Whether the bursting period scales with inner or outer variables has been a controversy in the turbulence literature for a number of years. The matter has been obscured by the fact that the experimental evidence has been measured in boundary layers with fairly low Reynolds numbers lying in a narrow range, so that it is not really possible to distinguish between the two types of scaling. The literature on turbulent polymer drag reduction is particularly instructive, however, since the sizes of the large eddies, and the bursting period, all change scale with the introduction of the polymer (see, for example, Kubo & Lumley 1980; Lumley & Kubo 1984). The present work indicates clearly that the wall region is capable of producing bursts autonomously, but the timing is determined by trigger signals from the outer layer. This suggests that events during a burst should scale unambiguously with wall variables. Time between bursts will have a more complex scaling, since it is dependent on the first occurrence of a *large* enough pressure signal *long* enough after a previous burst; 'long enough' is determined by wall variables, but the pressure signal should scale with outer variables, as described in §11.

Finally, we can mention some of the possible applications of this approach. Many drag reduction schemes appear to depend on a change of boundary conditions or of

distribution of effective viscosity in the wall region. For example, it has been suggested that polymer drag reduction is due to an increase in the effective viscosity in the turbulent part of the flow (effectively, a suppression of the intense higher-wavenumber turbulence), while it remains the same in the viscous sublayer. Microbubbles have been said to have their effect owing to reduction of the mean density, with an increase in effective viscosity, in the turbulent part of the wall layer, with essentially no change in the viscous sublayer. It has been suggested that riblets have their effect owing to an increase in the viscous losses at the boundary for the transverse velocities in the large eddies. It would be relatively simple to introduce changes in the distribution of the effective viscosity with distance from the wall, or in the boundary conditions, and see the effect of this on the dynamics of the wall region. One could imagine introduction of a compliant boundary. One could consider the pressure footprint of the eddy system on the wall (although much of the pressure signal sensed at the wall is transmitted from the outer part of the boundary layer; Farabee, 1986). Distributed parameter active control of turbulence requires a computable model to provide feedback, and our model might be adequate, and simple enough (S. B. Pope, private communication). It seems that our approach to the wall region has many interesting possibilities that could be explored.

While this paper was being prepared, Jang, Benney & Gran (1986) appeared. This paper describes an entirely different approach to the same region, intended to answer different questions. Jang *et al.* (1986) investigate the etiology of the rolls: what physical phenomenon causes them, concluding that they arise from a non-linear instability mechanism. On the other hand, we adopt the position of supposing that the rolls exist, and ask about their dynamical behaviour. (Recall that our decomposition, using empirical eigenfunctions, puts in the form of the rolls, leaving only the most energetic cross-stream wavenumber in question. However, since the vertical scale of the rolls is fixed, even this is fairly well predetermined.) Jang *et al.* (1986) and our papers thus complement each other.

Supported primarily by the U.S. Office of Naval Research under the program Select Research Opportunity IV, grant no N00014-85-K-0172. The experimental work leading to the empirical eigenfunctions was supported in part by the following organizations: The Naval Sea Systems Command (through the Garfield Thomas Water Tunnel and the Fluids Engineering Unit, Applied Research Laboratory, the Pennsylvania State University); The Office of Naval Research (through the General Hydrodynamics Program of the David W. Taylor Naval Ship Research and Development Center): The NASA–Ames Research Center, Aerodynamics Division (Gary T. Chapman, monitor); the NASA–Langley Research Center; the U.S. Air Force Office of Scientific Research (Aerospace Science Directorate (Michael Francis, Manager)).

Appendix A. General dynamical equations

$$\frac{\mathrm{d}a_k^{(n)}}{\mathrm{d}t} = (L_1 L_3)^{\frac{1}{2}} \sum_m a_k^{(m)} \Bigg[\underbrace{-(k_1^2+k_3^2)\,\delta_{mn}}_{\text{viscous term (linear)}}$$

$$+ \int_0^{X_2} \Bigg(\underbrace{D^2\phi_{i_k}^{(m)}\,\phi_{i_k}^{(n)*}}_{\text{viscous term (linear)}} - \underbrace{\left(1-\frac{x_2}{H}\right)\phi_{2_k}^{(m)}\,\phi_{1_k}^{(n)*} - \mathrm{i}k_1 x_2 \left(1-\frac{x_2}{2H}\right)\phi_{i_k}^{(m)}\,\phi_{i_k}^{(n)*}}_{\text{part of interaction with mean velocity (linear)}} \Bigg) \mathrm{d}x_2 \Bigg]$$

$$- \sum_{pq} \sum_{k'} a_{k'}^{(p)}\, a_{k-k'}^{(q)} (1-\delta_{k0}) \int_0^{X_2} \underbrace{\phi_{j_{k'}}^{(p)}\, \Omega_{k_j-k_j'}\, \phi_{i_{k-k'}}^{(q)}\, \phi_{i_k}^{(n)*}\, \mathrm{d}x_2}_{\text{inertia term (quadratic)}}$$

$$- \sum_{pqr} \sum_{k'} a_k^{(r)}\, a_{k'}^{(p)}\, a_{k'}^{(q)*} \Bigg(\underbrace{\int_0^{X_2} \phi_{1_{k'}}^{(p)}\, \phi_{2_{k'}}^{(q)*}\, \phi_{1_k}^{(n)*}\, \phi_{2_k}^{(r)} + \mathrm{i}k_1 \int_0^{X_2} \phi_{i_k}^{(n)*}\, \phi_{i_k}^{(r)} \int_0^{x_2} \phi_{1_{k'}}^{(p)}\, \phi_{2_{k'}}^{(q)*}\, \mathrm{d}x_2'\, \mathrm{d}x_2}_{\text{part of interaction with mean velocity coming from the Reynolds stress (cubic)}} \Bigg) \Bigg/$$

$$(L_1 L_3)^{\frac{1}{2}} - \underbrace{\hat{p}_k(X_2, t)\, \phi_{2_k}^{(n)*}(X_2)}_{\text{pressure term}}.$$

Here, i is the complex number $\mathrm{i}^2 = -1$, D denotes the derivative operator with respect to x_2: $\mathrm{D} = \mathrm{d}/\mathrm{d}x_2$, and

$$\Omega_{k_j} = \mathrm{i}k_j \quad \text{if } j = 1, 3$$
$$= \mathrm{D}\phi_k \quad \text{if } j = 2.$$

Appendix B. Energy transfer model

B.1. *Eddy viscosity*

The eddy viscosity is computed from the expression

$$\nu_{\mathrm{T}} = \frac{\alpha_1 \sum_{kn} \lambda_k^{(n)}}{\left(X_2 L_1 L_3 \sum_{kn} \lambda_k^{(n)} \left(\int_0^{X_2} \mathrm{D}\phi_{i_k}^{(n)}\, \mathrm{D}\phi_{i_k}^{(n)*}\, \mathrm{d}x_2 - k_1^2 - k_3^2 \right) \right)^{\frac{1}{2}}},$$

where the triplets $(\boldsymbol{k}, n)$ are the first neglected modes.

B.2. *The pseudopressures term*

As a rough approximation, the kinetic energy content of the small scales is proportional to the rate of loss of energy by the large scales to the small scales:

$$\langle u_{i>}\, u_{i>} \rangle_> - \langle\langle u_{i>}\, u_{i>} \rangle_> \rangle_> = -\alpha_2 \tau_> [(\langle u_{i>}\, u_{j>} \rangle_> - \langle\langle u_{i>}\, u_{j>} \rangle_> \rangle_>)\,(u_{i<,j} + u_{j<,i})$$
$$- \langle (\langle u_{i>}\, u_{j>} \rangle_> - \langle\langle u_{i>}\, u_{j>} \rangle_> \rangle_>)\,(u_{i<,j} + u_{j<,i}) \rangle],$$

where τ is a characteristic timescale of the first neglected modes: $\tau_> = l_>/u_>$,

$$\langle u_{i>}\, u_{i>} \rangle_> - \langle\langle u_{i>}\, u_{i>} \rangle_> \rangle_> = \alpha_2 l_>^2 [(u_{i<,j} + u_{j<,i})\,(u_{i<,j} + u_{j<,i})$$
$$- \langle (u_{i<,j} + u_{j<,i})\,(u_{i<,j} + u_{j<,i}) \rangle].$$

This term gives an extra quadratic term:

$$-\tfrac{2}{3} l_>^2 \sum_{pq} \Big(\sum_{k'} a_{k'}^{(p)}\, a_{k-k'}^{(q)} (\Omega_j \phi_{i_{k'}}^{(p)}(X_2)\, \Omega_j \phi_{i_{k-k'}}^{(q)}(X_2) + \Omega_j \phi_{i_{k'}}^{(p)}(X_2)\, \Omega_i \phi_{j_{k-k'}}^{(q)}(X_2)) \Big)\, \phi_{2_k}^{(n)*}(X_2).$$

Appendix C. List of coefficients of the set of 10 equations (24)

(i) Coefficients of the linear terms, a_k^1 and a_k^2 presented in the form of a two-column vector:

$$a^1 = [16.66,\ 28.27,\ 39.83,\ 52.08\ 60.98]^{\mathrm{T}}$$
$$a^2 = [-1.07,\ -1.75,\ -2.69,\ -3.95,\ -5.46]^{\mathrm{T}}.$$

(ii) Coefficients of the quadratic terms per complex equation, $c^1_{k',k-k'}$ and $c^2_{k',k-k'}$

Equation (1)		$c_{-1,2}$	$c_{-2,3}$	$c_{-3,4}$	$c_{-4,5}$
	c^1	2.09	1.13	0.46	0.21
	c^2	0.017	0.020	0.015	0.078
Equation (2)		$c_{1,1}$	$c_{3,-1}$	$c_{4,-2}$	$c_{5,-3}$
	c^1	−1.30	2.41	1.26	0.56
	c^2	−0.024	0.018	0.012	0.023
Equation (3)		$c_{1,2}$	$c_{4,-1}$	$c_{5,-2}$	
	c^1	−4.49	3.13	1.77	
	c^2	−0.04	0.009	0.014	
Equation (4)		$c_{1,3}$	$c_{2,2}$	$c_{5,-1}$	
	c^1	−5.81	−3.39	4.40	
	c^2	−0.061	−0.11	0.010	
Equation (5)		$c_{1,4}$	$c_{2,3}$		
	c^1	−6.44	−8.15		
	c^2	−0.16	−0.18		

(iii) Coefficients of the cubic terms presented in the form of a (5, 5) matrix, $d_{kk'}$:

$$d = \begin{bmatrix} -3.08 & -3.76 & -2.46 & -1.30 & -0.68 \\ -4.80 & -6.20 & -4.23 & -2.34 & -1.27 \\ -6.26 & -8.44 & -5.97 & -3.43 & -1.91 \\ -7.37 & -10.36 & -7.62 & -4.60 & -2.67 \\ -7.86 & -11.39 & -8.62 & -5.43 & -3.26 \end{bmatrix}$$

REFERENCES

Armbruster, D., Guckenheimer, J. & Holmes, P. 1988 Heteroclinic cycles and modulated traveling wave systems with $O(2)$ symmetry. *Physica D* **29**, 257–282.

Aubry, N. 1987 A dynamical system coherent structure approach to the fully developed turbulent wall layer. Ph.D. thesis, Cornell University.

Aubry, N., Holmes, P., Lumley, J. L. & Stone, E. 1987 The dynamics of coherent structures in the wall region of a turbulent boundary layer. *Sibley School of Mechanical and Aerospace Engineering Rep.* FDA-86-15. Cornell University.

Bakewell, P. & Lumley, J. L. 1967 Viscous sublayer and adjacent wall region in turbulent pipe flow. *Phys. Fluids* **10**, 1880–1889.

Bergé, P., Dubois, M., Manneville, P. & Pomeau, Y. 1980 Intermittency in Rayleigh–Bénard convection. *J. Phys. Lett.* **41**, L341.

Blackwelder, R. F. & Eckelmann, H. 1979 Streamwise vortices associated with the bursting phenomenon. *J. Fluid Mech.* **94**, 577–594.

Blackwelder, R. F. & Kaplan, R. E. 1976 On the wall structure of the turbulent boundary layer. *J. Fluid Mech.* **76**, 89–112.

Busse, F. H. 1981 Transition to turbulence in Rayleigh–Bénard convection. In *Hydrodynamic instabilities and the transition to turbulence* (ed. H. L. Swinney & J. P. Gollub), pp. 97–137. Springer.

BUSSE, F. M. & HEIKES, K. E. 1980 Convection in a rotating layer: a simple case of turbulence. *Science* **208**, 173–175.

CAMPBELL, D. & ROSE, H. 1983 *Order in Chaos*. North-Holland.

CANTWELL, B. J. 1981 Organized motion in turbulent flow. *Ann. Rev. Fluid Mech.* **13**, 457–515.

CHAPMAN, D. R. & KUHN, G. D. 1986 The limiting behaviour of turbulence near a wall. *J. Fluid Mech.* **170**, 265–292.

CORINO, E. R. & BRODKEY, R. S. 1969 A visual investigation of the wall region in turbulent flow. *J. Fluid Mech.* **37**, 1–30.

CORRSIN, S. 1957 Some current problems in turbulent shear flows. In *Proc. Naval Hydr. Symp. 24–28 Sept. 1956*. (ed. F. S. Shemen): 373. US Office of Naval Research 1956.

DEVANEY, R. L. 1985 *An Introduction to Chaotic Dynamical Systems*. Benjamin–Cummings.

DOEDEL, E. J. & KERNEVEZ, J. P. 1985 Software for continuation problems in ordinary differential equations with applications. *Applied Mathematics Rep.* California Institute of Technology.

DRAZIN, P. G. & REID, W. H. 1981 *Hydrodynamic Stability*. Cambridge University Press.

DUBOIS, M., RUBIO, M. A. & BERGÉ, P. 1983 Experimental evidence of intermittencies associated with a subharmonic bifurcation. *Phys. Rev. Lett.* **51**, 1446–1449.

ERSOY, S. & WALKER, J. D. A. 1985 Viscous flow induced by counter-rotating vortices. *Phys. Fluids* **28**, 2687–2698.

FARABEE, T. M. 1986 An experimental investigation of wall pressure fluctuations beneath non-equilibrium turbulent flows. *David W. Taylor Naval Ship Research and Development Center* DTNSRDC-86-047.

GLAUSER, M. N., GEORGE, W. K. & TAULBEE, D. B. 1985*b* Evaluation of an alternative orthogonal decomposition. *38th Annual American Physical Society. Division of Fluid Dynamics. Tucson, Arizona. Nov. 24–25.*

GLAUSER, M. N., LEIB, S. J. & GEORGE, W. K. 1985*a* Coherent structure in the axisymmetric jet mixing layer. *Proc. 5th Symp. of the Turbulent Shear Flow Conf. Cornell University.* Springer.

GOLUBITSKY, M. & GUCKENHEIMER, J. (eds) 1986 *Multiparameter Bifurcation Theory*. A.M.S. Contemporary Mathematics Series, No. 56. American Mathematical Society, Providence, R.I.

GUCKENHEIMER, J. 1986 Strange attractors in fluids: another view. *Ann. Rev. Fluid Mech.* **18**, 15–31.

GUCKENHEIMER, J. & HOLMES, P. J. 1983 *Nonlinear Oscillations, Dynamical Systems and Bifurcations of Vector Fields*. Springer. (Corrected second printing, 1986).

HATZIAVRAMIDIS, D. T. & HANRATTY, T. J. 1979 The representation of the viscous wall region by a regular eddy pattern. *J. Fluid Mech.* **95**, 655–679.

HEAD, M. R. & BANDYOPADHYAY, P. 1981 New aspects of turbulent boundary layer structure. *J. Fluid Mech.* **107**, 297–338.

HERZOG, S. 1986 The large scale structure in the near-wall region of turbulent pipe flow. Ph.D. thesis, Cornell University.

HOGENES, J. H. A. & HANRATTY, T. J. 1982 The use of multiple wall probes to identify coherent flow patterns in the viscous wall region. *J. Fluid Mech.* **124**, 363–390.

HYMAN, J. M. & NICOLAENKO, B. 1985 The Kuromoto–Sivashinsky equation: a bridge between PDEs and dynamical systems. *Los Alamos Rep.* UR-85-1556.

HYMAN, J. M., NICOLAENKO, B. & ZALESKI, S. 1986 Order and complexity in the Kuromoto–Sivashinsky model of weakly turbulent interfaces. *Physica D* **23**, 265–292.

JANG, P. S., BENNEY, D. J. & GRAN, R. L. 1986 On the origin of streamwise vortices in a turbulent boundary layer. *J. Fluid ,mech.* **169**, 109–123.

KEEFE, L., MOIN, P. & KIM, J. 1987 The dimension of an attraction in turbulent Poiseuille flow. *Bull. Am. Phys. Soc.* **32**, 2026.

KIM, J. 1983 On the structure of wall-bounded turbulent flows. *Phys. Fluids* **26**, 2088–2097.

KIM, J. 1985 Turbulence structures associated with the bursting event. *Phys. Fluids* **28**, 52–58.

KIM, H. T., KLINE, S. J. & REYNOLDS, W. C. 1971 The production of turbulence near a smooth wall in a turbulent boundary layer. *J. Fluid Mech.* **50**, 133–160.

KIM, J. & MOIN, P. 1986 The structure of the vorticity field in turbulent channel flow. Part 2. Study of ensemble-averaged fields. *J. Fluid Mech.* **162**, 339–363.

KLINE, S. J., REYNOLDS, W. C., SCHRAUB, F. A. & RUNDSTADLER, P. W. 1967 The structure of turbulent boundary layers. *J. Fluid Mech.* **30**, 741–773.

KUBO, I. & LUMLEY, J. L. 1980 A study to assess the potential for using long chain polymers dissolved in water to study turbulence. *Ann. Rep. NASA-Ames Grant No. NSG*-2382. Cornell University.

LOÈVE, M. 1955 *Probability Theory.* Van Nostrand.

LORENZ, E. N. 1963 Deterministic non-periodic flow. *J. Atmos. Sci.* **20**, 130–141.

LU, S. S. & WILLMARTH, W. W. 1973 Measurements of the structure of the Reynolds stress in a turbulent boundary layer. *J. Fluid Mech.* **60**, 481–511.

LUMLEY, J. L. 1967 The structure of inhomogeneous turbulent flows. In *Atmospheric Turbulence and Radio Wave Propagation* (ed. A. M. Yaglom & V. I. Tatarski), pp. 166–178. Moscow: Nauka.

LUMLEY, J. L. 1970 *Stochastic Tools in Turbulence.* Academic.

LUMLEY, J. L. 1981 Coherent structures in turbulence. In *Transition and Turbulence* (ed. R. E. Meyer), pp. 215–242. Academic.

LUMLEY, J. L. & KUBO, I. 1984 Turbulent drag reduction by polymer additives: a survey. In *The Influence of Polymer Additives on Velocity and Temperature Fields. IUTAM Symposium Essen 1984.* (ed. B. Gampert), pp. 3–21. Springer.

MARSDEN, J. E. & MCCRACKEN, M. 1976 *The Hopf Bifurcation and its Applications.* Springer.

MAURER, J. & LIBCHABER, A. 1980 Effects of the Prandtl number on the onset of turbulence in liquid helium. *J. Phys. Paris Lett.* **41**, L-515–518.

MOIN, P. 1984 Probing turbulence via large eddy simulation. *AIAA 22nd Aerospace Sciences Meeting.*

MONIN, A. S. 1978 On the nature of turbulence. *Sov. Phys. Usp.* **21** 429–442.

NICOLAENKO, B. 1986 Lecture delivered at workshop on *Computational Aspects of Dynamical Systems, Mathematical Sciences Institute, Cornell University, September 8–10, 1986.*

NIKOLAIDES, C. 1984 A study of the coherent structures in the viscous wall region. Ph.D. thesis, University of Illinois, Urbana.

POMEAU, Y. & MANNEVILLE, P. 1980 Intermittent transition to turbulence. *Communs Math. Phys.* **74**, 189–197.

RAND, D. A. & YOUNG, L. S. (eds) 1981 *Dynamical Systems and Turbulence.* Lecture Notes in Mathematics, vol. 898. Springer.

RICHETTI, P., ARGONE, F. & ARNEODO, A. 1985 Type-II intermittency in a periodically driven non-linear oscillator. Preprint, Université de Nice.

RUELLE, D. & TAKENS, F. 1971 On the nature of turbulence. *Communs Math. Phys.* **82**, 137–151.

SILNIKOV, L. P. 1965 A case of the existence of a denumerable set of periodic motions. *Sov. Math. Dokl* **6**, 163–166.

SILNIKOV, L. P. 1968 On the generation of a periodic motion from trajectories doubly asymptotic to an equilibrium state of saddle type. *Math. USSR Sbornik* **6**, 427–438.

SILNIKOV, L. P. 1970 A contribution to the problem of the structure of an extended neighbourhood of a rough equilibrium state of saddle-focus type. *Math USSR Sbornik* **10**, 91–102.

SIROVICH, L. 1987*a* Turbulence and the dynamics of coherent structures: I. *Q. Appl. Maths* **45**, 561–571.

SIROVICH, L. 1987*b* Turbulence and the dynamics of coherent structures: II. *Q. Appl. Maths* **45**, 573–582.

SIROVICH, L. 1987*c* Turbulence and the dynamics of coherent structures: III. *Q. Appl. Maths* **45**, 583–590.

SIROVICH, L., MAXEY, M. & TARMAN, H. 1987 Analysis of turbulent thermal convection. In *Turbulent Shear Flows 6* (ed F. Durst *et al.*). Springer (in press).

SIROVICH, L. & RODRIGUEZ, J. D. 1987 Coherent structures and chaos: a model problem. *Phys. Lett.* **A 120**, 211–214.

SMALE, S. 1967 Differentiable dynamical systems. *Bull. Am. Math. Soc.* **73**, 747–817.

SMITH, C. R. 1984 A synthesized model of the near wall behavior in turbulent boundary layers. In *Proc. Eighth Symp. on Turbulence* (ed. G. K. Patterson & J. L. Zakin), Dept. of Chem. Eng., University of Missouri-Rolla.

SMITH, C. R. & SCHWARZ, S. P. 1983 Observation of streamwise rotation in the near-wall region of a turbulent boundary layer. *Phys. Fluids* **26**, 641–652.

SPARROW, C. T. 1982 *The Lorenz Equations: Bifurcations, Chaos and Strange Attractors.* Springer.

SWINNEY, H. L. 1983 Observations of order and chaos in physical systems. *Physica* **7D**, 3–15. Also in Campbell and Rose 1983.

SWINNEY, H. L. & GOLLUB, J. P. (eds) 1981 *Hydrodynamic Instabilities and the Transition to Turbulence.* Springer.

TENNEKES, H. & LUMLEY, J. L. 1972 *A First Course in Turbulence.* M.I.T. Press.

THEODORSEN, T. 1952 Mechanism of turbulence. In *Proc. 2nd Midwestern Conf. on Fluid Mech. Ohio State U., Columbus, Ohio.*

TRESSER, C. 1984 About some theorems by L. P. Silnikov. *Ann de L'Inst. H. Poincané* **40**, 441–461.

TRESSER, C., COULLET, P. & ARNEODO, A. 1980 On the existence of hysteresis in a transition to chaos after a single bifurcation. *J. Phys. Paris Lett.* **41**, L243–246.

WILLMARTH, W. W. 1975 Structure of turbulence in boundary layers. *Adv. Appl. Mech.* **15**, 159–254.

WILLMARTH, W. W. & BOGAR, T. J. 1977 Survey and new measurements of turbulent structure near the wall. *Phys. Fluids Suppl.* **20**, S9–S21.

WILLMARTH, W. W. & LU, S. S. 1972 Structure of the Reynolds stress near the wall. *J. Fluid Mech.* **55**, 65–92.

WILLMARTH, W. W. & TU, B. J. 1967 Structure of turbulence in the boundary layer near the wall. *Phys. Fluids Suppl.* **10**, S134–S137.

ZILBERMAN, M., WYGNANSKI, I. & KAPLAN, R. E. 1977 Transitional boundary layer spot in a fully turbulent environment. *Phys. Fluids Suppl.* **20**, S258–S271.